vgi 2+3/2015

103. Jahrgang Heft 2+3/2015

Österreichische Zeitschrift für

vgi Vermessung & Geoinformation

Austrian Contributions to the XXVI General Assembly of the IUGG

Austrian Contributions to the XXVI General Assembly of the International Union of Geodesy and Geophysics (IUGG)

June 22– July 2, 2015, Prague, Czech Republic

Österreichische Zeitschrift für
Vermessung & Geoinformation

Organ der Österreichischen Gesellschaft für Vermessung und Geoinformation und der Österreichischen Geodätischen Kommission

103. Jahrgang 2015
Heft: 2+3/2015
ISSN: 1605-1653

Schriftleiter: Dipl.-Ing. Andreas Pammer
Stellvertreter: Dipl.-Ing. Ernst Zahn
Dipl.-Ing. (FH) Georg Topf

A-1020 Wien, Schiffamtsgasse 1-3
Internet: http://www.ovg.at

Special Issue
XXVI General Assembly of the International Union of Geodesy and Geophysics (IUGG), Prague, Czech Republic

ed. by Hana Krásná, Franz Rottensteiner, Werner Lienhart und Manfred Wieser
(All Papers of this issue were peer-reviewed.)

Impressum

Österreichische Zeitschrift für Vermessung & Geoinformation

Organ der Österreichischen Gesellschaft für Vermessung und Geoinformation und der Österreichischen Geodätischen Kommission

103. Jahrgang 2015 / ISSN: 1605-1653

Herausgeber und Medieninhaber: Österreichische Gesellschaft für Vermessung und Geoinformation (OVG), Austrian Society for Surveying and Geoinformation, Schiffamtsgasse 1-3, A-1020 Wien zur Gänze. Bankverbindung: BAWAG P.S.K., IBAN: AT21 60000 00001190933, BIC: OPSKATWW. ZVR-Zahl 403011926.

Präsident der Gesellschaft: Dipl.-Ing. Julius Ernst, Tel. + 43 1 21110-3703, Schiffamtsgasse 1-3, A-1020 Wien.

Sekretariat der Gesellschaft: Dipl.-Ing. Franz Blauensteiner, Tel. +43 1 21110-2216, Schiffamtsgasse 1-3, A-1020 Wien. E-Mail: office@ovg.at.

Schriftleitung: Dipl.-Ing. Andreas Pammer, Tel. +43 1 21110-5262, Dipl.-Ing. Ernst Zahn, Tel. +43 1 21110-3209, Dipl.-Ing. (FH) Georg Topf, Tel. +43 1 21110-3620, Schiffamtsgasse 1-3, A-1020 Wien. E-Mail: vgi@ovg.at.

Manuskripte: Bitte direkt an die Schriftleitung senden. Es wird dringend ersucht, alle Beiträge in digitaler Form zu übersenden. Genaue Angaben über die Form der Abfassung des Textteiles sowie der Abbildungen (Autoren-Richtlinien) können bei der Schriftleitung angefordert werden bzw. sind auf http://www.ovg.at unter „VGI Richtlinien“ zu ersehen. Beiträge können in Deutsch oder Englisch abgefasst sein; Hauptartikel bitte mit einer deutschsprachigen Kurzfassung und einem englischen Abstract sowie Schlüsselwörter bzw. Keywords einsenden. Auf Wunsch können Hauptartikel einem „Blind-Review“ unterzogen werden. Nach einer formalen Überprüfung durch die Schriftleitung wird der Artikel an ein Mitglied des Redaktionsbeirates weitergeleitet und von diesem an den/die Reviewer verteilt. Artikel, die einen Review-Prozess erfolgreich durchlaufen haben, werden als solche gesondert gekennzeichnet. Namentlich gezeichnete Beiträge geben die Meinung des Autors wieder, die sich nicht mit der des Herausgebers decken muss. Die Verantwortung für den Inhalt des einzelnen Artikels liegt daher beim Autor. Mit der Annahme des Manuskriptes sowie der Veröffentlichung geht das alleinige Recht der Vervielfältigung und Wiedergabe auf den Herausgeber über.

Redaktionsbeirat für Review: Univ.-Prof. Dr. Johannes Böhm, Univ.-Prof. Dr. Werner Lienhart, Univ.-Prof. Dr. Norbert Pfeifer, Dipl.-Ing. Gert Steinkellner, Prof. Dr. Josef Strobl, O.Univ.-Prof. Dipl.-Ing. Dr. Hans Sünkel und Univ.-Doz. Dipl.-Ing. Dr.iur. Christoph Twaroch

Anzeigenbearbeitung und -beratung: Dipl.-Ing. Andreas Pammer, Tel. +43 1 21110-5336, Schiffamtsgasse 1-3, A-1020 Wien. Unterlagen über Preise und technische Details werden auf Anfrage gerne zugesendet.

Erscheinungsweise: Vierteljährlich in zwangloser Reihenfolge (1 Jahrgang = 4 Hefte). Auflage: 1200 Stück.

Abonnement: Nur jahrgangsweise möglich. Ein Abonnement gilt automatisch um ein Jahr verlängert, sofern nicht bis zum 1.12. des laufenden Jahres eine Kündigung erfolgt. Die Bearbeitung von Abonnementangelegenheiten erfolgt durch das Sekretariat. Adressänderungen sind an das Sekretariat zu richten.

Verkaufspreise: Einzelheft: Inland 15 €, Ausland 18 €; Abonnement: Inland 50 €, Ausland 60 €; alle Preise exklusive Mehrwertsteuer. OVG-Mitglieder erhalten die Zeitschrift kostenlos.

Satz und Druck: Buchdruckerei Ernst Becvar Ges.m.b.H., A-1150 Wien, Lichtgasse 10.

Offenlegung gem. § 25 Mediengesetz

Medieninhaber: Österreichische Gesellschaft für Vermessung und Geoinformation (OVG), Austrian Society for Surveying and Geoinformation, Schiffamtsgasse 1-3, A-1020 Wien zur Gänze.

Aufgabe der Gesellschaft: gem. § 1 Abs. 1 der Statuten (gen. mit Bescheid der Bundespolizeidirektion Wien vom 26.11.2009): a) die Vertretung der fachlichen Belange der Vermessung und Geoinformation auf allen Gebieten der wissenschaftlichen Forschung und der praktischen Anwendung, b) die Vertretung aller Angehörigen des Berufsstandes, c) die Förderung der Zusammenarbeit zwischen den Kollegen der Wissenschaft, des öffentlichen Dienstes, der freien Berufe und der Wirtschaft, d) die Förderung des wissenschaftlichen Nachwuchses, e) die Herausgabe einer Zeitschrift mit dem Namen „Österreichische Zeitschrift für Vermessung und Geoinformation“ (VGI).

Erklärung über die grundlegende Richtung der Zeitschrift: Wahrnehmung und Vertretung der fachlichen Belange aller Bereiche der Vermessung und Geoinformation, der Photogrammetrie und Fernerkundung, sowie Information und Weiterbildung der Mitglieder der Gesellschaft hinsichtlich dieser Fachgebiete.

http://www.ovg.at

http://www.oegk-geodesy.at

Preface to the VGI Special Issue

The Austrian Geodetic Commission (ÖGK) is the national organisation in Austria adhering to the International Association of Geodesy (IAG), one of the eight associations of the International Union of Geodesy and Geophysics (IUGG).

The 26th General Assembly of IUGG will take place in Prague, Czech Republic, June 22nd to July 2nd, 2015. Every four years IAG and the other associations within IUGG present the work performed during this General Assembly. It is also used to review and adapt the structure where necessary and appoint officers for the coming period.

ÖGK has decided to contribute to this General Assembly with a collection of research papers of Austrian institutions related to geodesy.

The main task of this special issue of the *Österreichische Zeitschrift für Vermessung & Geoinformation (VGI)* is to give the international geodetic research community an idea about the various topics Austrian geodesists are working on. Additionally, this scientific work should be cumulatively shown to those Austrian colleagues who are mainly involved in practical and administrative work. The variety of research topics indicates how closely geodesy is related to its neighbouring disciplines within IUGG such as, e.g., geophysics, but also to other fields like geoinformation science and computer science. Joint efforts in different fields are required to achieve the goals serving our society, such as precise navigation on Earth, a thorough understanding of 'System Earth', or the sustainable use of natural resources.

With 12 papers this special issue of VGI is more than only snapshot of the geodetic research work carried out in Austria, but also gives insight into research programs and trends. The authors come from the Technische Universität Wien and Graz University of Technology, both offering the full educational programme in geodesy and geoinformation, as well as the Federal Office of Metrology and Surveying (BEV), the Space Research Institute (IWF) of the Austrian Academy of Sciences, and their research partners.

I am particularly grateful to the four guest-editors of this issue, Hana Krásná, Franz Rottensteiner, Werner Lienhart and Manfred Wieser. All papers of this issue were peer-reviewed by experts in the respective field. This ensures the quality of the published articles. Thus, I also want to thank all reviewers for their useful comments and constructive remarks.

On behalf of all authors and the four guest-editors I would like to acknowledge the Austrian Society of Geodesy and Geoinformation (OVG) for providing this platform for the publications. In particular we are grateful to the editor-in-chief of the VGI, Andreas Pammer, and his two deputy editors, Ernst Zahn and Georg Topf, for taking care of the layout of the papers and solving all technical problems. Finally, I want to extend my sincere gratitude to Norbert Höggerl, Secretary of the Austrian Geodetic Commission. His support was essential for the entire process of publishing this special issue for the IUGG General Assembly.

Norbert Pfeifer

President of the Austrian Geodetic Commission
Technische Universität Wien,
Department of Geodesy and Geoinformation


Continuous modelling of point clouds by means of freeform surfaces

Corinna Harmening and Hans Neuner, Wien

Abstract

Deformation analysis is one of the classical tasks in engineering geodesy. The development of the laser scanner has changed the respective data acquisition as well as the data analysis: Instead of point based approaches, areal ones move into focus. In this paper a project is presented which aims to develop a spatiotemporal continuous collocation. In order to model the deterministic trend, B-spline surfaces are used. The parameterization required for the estimation of such freeform surfaces is realized by projecting the acquired point cloud onto a based surface called Coons patch. In order to handle irregular point densities, boundary constraints are introduced.

Keywords: Laser scanning, modelling, freeform surfaces, boundary constraints, datum definition

Kurzfassung

Die Deformationsanalyse ist eines der klassischen Aufgabenfelder der Ingenieurgeodäsie. Mit der Entwicklung des Laserscanners haben sich neben der Datenerfassung auch die entsprechenden Auswertestrategien verändert: Anstelle von punktbasierten Ansätzen rücken flächenhafte Methoden immer mehr in den Fokus. Das Ziel des in diesem Paper vorgestellten Projektes ist die Entwicklung einer raumzeitlichen Kollokation, deren deterministischer Trend mit Hilfe von B-Spline-Flächen modelliert wird. Die Schätzung solcher Freiformflächen erfordert eine Parametrisierung der Beobachtungen. Aus diesem Grund wird mit dem sogenannten Coons Patch eine Basisfläche definiert, auf die die erfasste Punktwolke projiziert wird. Für Punktwolken mit unregelmäßigen Punktdichten wird das Ausgleichungsergebnis durch das Einführen von Randbedingungen stabilisiert.

Schlüsselwörter: Laserscanning, Modellierung, B-Splines, Randbedingungen, Datumsdefinition

1. Introduction

The development of terrestrial laser scanners has substantially increased the importance of areal measurements in engineering geodesy [1]. In order to preserve the added value yielded by these techniques in comparison to the conventional point based ones, an areal data analysis is unavoidable. This is in general achieved by extending existing point based approaches.

Least-squares collocation is a well-established method in geodesy. It distinguishes itself from other methods by modelling the observed phenomena not only by means of a deterministic trend, but also by means of a statistical signal.

The aim of the present project is the extension of the classical least-squares collocation to an approach which is continuous in space and time, so that a description of deformations to arbitrary times and in arbitrary places of the object is possible.

The spatiotemporal collocation starts with the modelling of the geometric part of the areal deformation process by means of freeform surfaces such as B-splines. The estimation of this type of surfaces requires the allocation of appropriate surface parameters to the observations. Setting up the surface's parameter form, is in the focus of this contribution.

B-spline curves and surfaces have been investigated for various geodetic applications: In [2] B-spline surfaces are used as an alternative for spherical harmonics in order to describe the vertical total electron content of the Earth's atmosphere. The observations' parameterization is realised by means of their two-dimensional Cartesian coordinates scaled to the unit square.

In engineering geodesy freeform curves and surfaces are used to model point clouds acquired by laser scanners: The authors of [3] use terrestrial laser scanning in order to determine a bridge's deflection under traffic load. The resulting nonlinear point profiles are parameterized by means of the points' Euclidean distances and afterwards approximated by B-spline curves. The freeform surface's potential to describe deformations is demonstrated in [4]: A plastic sheet is being deformed under pressure while a laser scanner is measuring points on the deforming surface. Three-dimensional B-spline surfaces are used to describe the resulting point clouds analytically. The author assumes a grid-like ar-

rangement of the measured points which allows a parameterization using the Euclidian distances between the observations.

The present paper is structured as follows: Section 2 provides the mathematical basis concerning the estimation of B-spline curves and surfaces. In section 3 a parameterization approach is introduced, which is based on an object, instead of a superior coordinate system. This guarantees that the parameterization reflects the object's actual form. Furthermore, the presented approach is able to handle unordered point clouds, which generally are a laser scanner's output. As a consequence, no simplifying assumptions about the observations' arrangement have to be made. The achieved parameterization is improved iteratively, whereby irregular point densities are managed by introducing boundary constraints. In the last subsection of section 3 it is discussed whether the parameterization can serve as a basis for the datum definition. The overall results are summarized in section 4.

2. Estimation of freeform curves and surfaces

2.1 Estimation of B-spline curves

A B-spline curve of degree p is defined by its $n+1$ control points P_i [5]:

$$C(u) = \sum_{i=0}^{n} N_{i,p}(u) P_i,\ u = [0,\dots,1]. \quad (1)$$

A curve point $C(u)$ therefore results as the weighted average of the control points P_i. The corresponding weights are defined by the B-spline basis functions $N_{i,p}$, which can be computed recursively by means of the Cox-de Boor-algorithm (see [6]; [7]). In addition to the control points, the degree p as well as a knot vector $U = [u_0,\dots,u_m]$ are required to define a B-spline curve uniquely.

When estimating a B-spline curve, the number of control points as well as the curve's degree p can be specified a priori. This results in a linear relationship between the $N+1$ observations $C(u_k)$ and the unknown parameters P_i. Before estimating the curve, convenient parameters u_k have to be allocated to the observations. In case of curve estimation, where the observations are arranged chain-like, either the uniform, the cumulative chord length or the centripetal parameterization is commonly used [8]. In the following the cumulative chord length parameterization is used, whereby the required parameters u_k are determined by means of the Euclidean distance between neighbouring observations:

$$u_k = \begin{cases} 0, & k = 0 \\ u_{k-1} + \dfrac{\left|C(u_k) - C(u_{k-1})\right|}{\sum_{k=1}^{N} C(u_k) - C(u_{k-1})}, & k > 0 \\ 1, & k = N. \end{cases} \quad (2)$$

Thus, the observation's parameterization is independent of the curve's spatial orientation.

In order to avoid singularities in the normal equation system, each knot span of the knot vector U has to contain at least one parameter u_k. In [5] an algorithm is proposed which guarantees that this requirement is fulfilled. The knot vector U and its further influence on the curve and surface estimation are not considered here; for further details related to this topic please refer to [5].

2.2 Estimation of B-spline surfaces

In order to describe a B-spline surface, the so called tensor product representation is used, which represents a surface as an infinite number of parametric curves running into two different directions. In order to construct such a surface, two one-dimensional basis functions are multiplied [5]:

$$S(u,v) = \sum_{i=0}^{m}\sum_{j=0}^{n} N_{i,p}(u) N_{j,q}(v) P_{ij} \quad (3)$$
$$u,\ v = [0,\dots,1].$$

A surface point $S(u_k, v_k)$ is thus given by a grid of $(m+1)\times(n+1)$ control points P_{ij}, the degree p and the knot vector U in the direction of the parameter u as well as the degree q and the knot vector V in v-direction.

Similar to the curve estimation, the number of control points ($m+1$ and $n+1$), the knot vectors U and V as well as the surface's degrees p and q can be specified a priori. If the measured points were ordered grid-like, the observations could be parameterized by means of the above mentioned methods [8]. In engineering geodesy the grid-like arrangement cannot be presumed; rather, the usually unordered point clouds require an alternative method, which is presented in the following.

3. Surface parameterization

A common approach to parameterize unordered point clouds is the definition of a base surface with known parametric form and a subsequent projection of the observed points onto this surface. Via this projection it is possible to allocate

parameters belonging to the base surface's parameter space to the observations. The difficulty of this procedure lies in defining an appropriate base surface, which has to fulfil certain criteria according to [8]: On the one hand the base surface has to be as smooth as possible while being a good approximation of the point cloud. On the other hand an unambiguous projection of the observed points onto the surface has to be possible. As the base surface's parameterization influences the parameterization of the surface to be estimated, the former should furthermore reflect the point cloud's form. Regarding an automated analysis, the base surface's formulation should additionally be generally valid and consequently independent from the acquired data set.

Because of the complexity of the relevant surfaces in engineering geodesy, a completely general valid approach is not possible. For this reason, those surfaces will be classified according to the number of delimiting curves in the following section. The resulting classes form the basis for the parameterization.

3.1 Characterization of surfaces

Typically, either simple geometric primitives are used as base surfaces or the base surface is constructed from the point cloud's boundary curves [8]. As the strategy depends on the number of curves delimiting the point cloud, it is obvious to use this number as a classification criterion to categorize surfaces, which are relevant in engineering geodesy, into three classes:

- Closed surfaces are delimited by no boundary curve [9]. In engineering geodesy those surfaces occur rather seldom. In these rare cases – for example in case of reference spheres for the terrestrial laser scanning – the surfaces take on simple geometric shapes, so that an unambiguous projection on a sphere is possible. The projection on this base surface is realised by computing spherical coordinates. The final parameterization results from the latitude φ und the longitude θ scaled to a range of [0, 1].
- Tubes of industrial plants or cooling towers represent surfaces which are delimited by two boundary curves. In engineering geodesy this type of surface also appears in general as a simple geometric shape like a cylinder or a hyperboloid of one sheet. Consequently, these surfaces are parameterized by computing the cylindrical coordinates radius r, azimuth φ as wells as the height h and scaling φ and h to the range of [0, 1].
- All other surfaces being relevant in engineering geodesy are delimited either by one or by four boundary curves. As a single curve can be subdivided into four segments and a surface delimited by one curve therefore can be transformed into a surface with four boundary curves, these two cases can be handled consistently. These cases are the main focus of this contribution and will be addressed in detail as well as demonstrated on two example data sets, which are presented in the following.

The first data set is a part of a church vault delimited by four boundary curves (see Figure 1). Like most anthropogenic objects, the vault has simple geometric structures and therefore can also be approximated by means of regular geometric shapes.

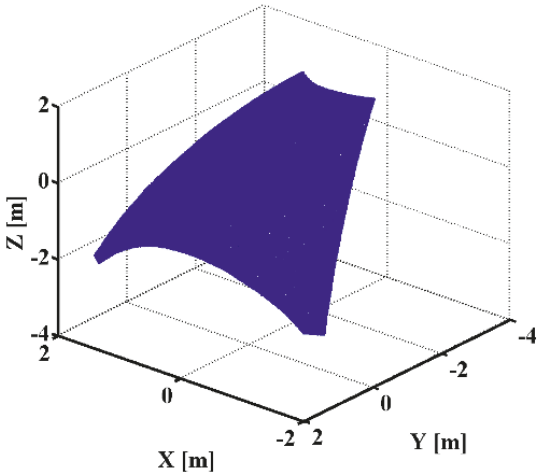

Fig. 1: Point cloud of a church's vault

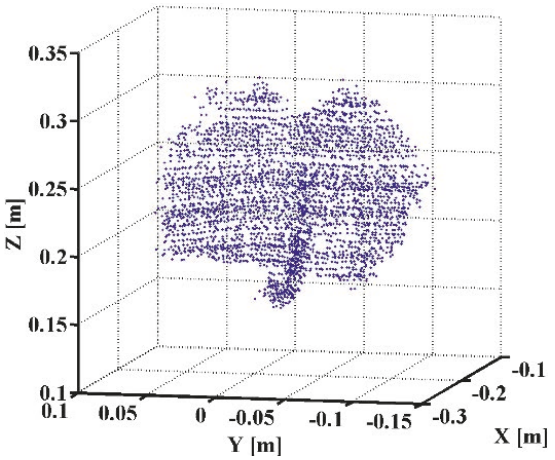

Fig. 2: Point cloud of a leaf

An example for an object delimited by one boundary curve is the leaf of a cucumber plant, which can be seen in Figure 2. Natural objects like this leaf cannot be approximated sufficiently well by means of simple geometric shapes. Furthermore, the point density varies because of the leaf's complex structure, so that the point cloud's approximation by means of freeform surfaces is impeded.

3.2 Parameterization of surfaces with four boundary curves

In order to parameterize surfaces which are delimited by four boundary curves, Coons patch (see [8]) is used as a base surface. The first step for the construction of this patch is the determination of four boundary curves in B-spline form. Regardless of whether the surface is delimited by one or by four curves, boundary points have to be detected automatically at first (see [10]). These boundary points form the basis for the estimation of one and four B-spline curves respectively (cf. section 2), which delimit the patch (see Figure 3 and 4). In case only one boundary curve has been estimated, this curve is subdivided into four segments with the same number of control points by means of the Cox-de Boor algorithm afterwards (see [6]; [7]). The results of the curve estimation are four B-spline curves delimiting the point cloud:

$$C_k(u_C) = \sum_{i_C=0}^{n_C} N_{i_C,p_C}(u_C) P_{i_C}^k, \qquad k = 0,1 \qquad (4)$$

$$C_l(v_C) = \sum_{j_C=0}^{m_C} N_{j_C,q_C}(v_C) P_{j_C}^l, \qquad l = 0,1. \qquad (5)$$

Facing curves are denoted by the letters k and l in superscript and have the same degree as well as the same number of control points. Furthermore, it should be noted that these curves have to be defined on the same knot vector [5]. These conditions have to be fulfilled, as these four curves define the degrees, the number of control points as well as the parameterization of the base surface to be constructed.

In order to distinguish the parameters determining the boundary curves from the parameters of the estimated surface, the former are denoted by the index C.

Coons patch is constructed by two types of surfaces: On the one hand the two pairs of facing curves are used to construct two ruled surfaces $R_u(u_C, v_C)$ and $R_v(u_C, v_C)$ by interpolating linearly between points having the same parameter value [11]:

$$R_u(u_C, v_C) = \left(1 - \frac{i_C}{n_C}\right) P_{0,j_C} + \frac{i_C}{n_C} P_{n_C,j_C}, \; u_C = \frac{i_C}{n_C} \qquad (6)$$

$$R_v(u_C, v_C) = \left(1 - \frac{j_C}{m_C}\right) P_{i_C,0} + \frac{j_C}{m_C} P_{i_C,m_C}, \; v_C = \frac{j_C}{m_C}. \qquad (7)$$

On the other hand the bilinear interpolant of the four corner points is computed:

$$B(u_C, v_C) = \begin{bmatrix} 1 - \frac{j_C}{m_C} & \frac{j_C}{m_C} \end{bmatrix} \begin{bmatrix} P_{0,0} & P_{0,n_C} \\ P_{m_C,0} & P_{m_C,n_C} \end{bmatrix} \begin{bmatrix} 1 - \frac{i_C}{n_C} \\ \frac{i_C}{n_C} \end{bmatrix}. \qquad (8)$$

The vault's ruled surface in u-direction as well as its bilinear interpolant are exemplarily shown in the Figures 5 and 6.

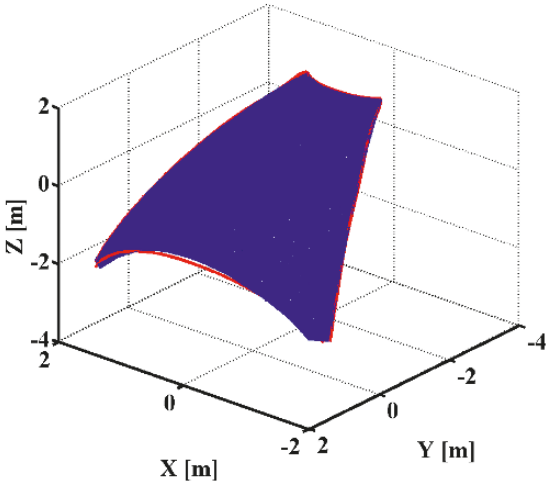

Fig. 3: The vault's four boundary curves

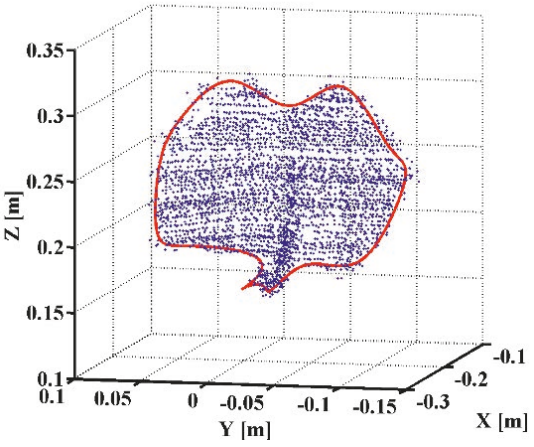

Fig. 4: The leaf's boundary curve

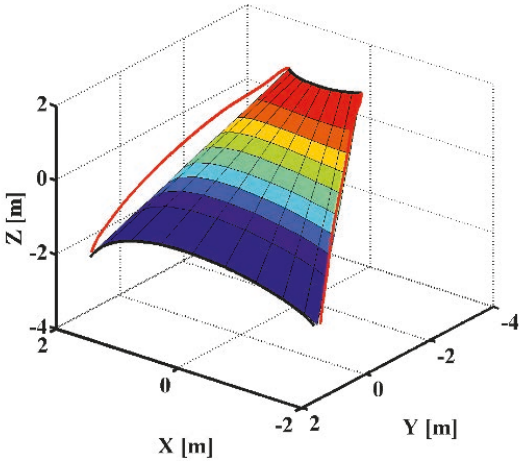

Fig. 5: The vault's ruled surface in u-direction

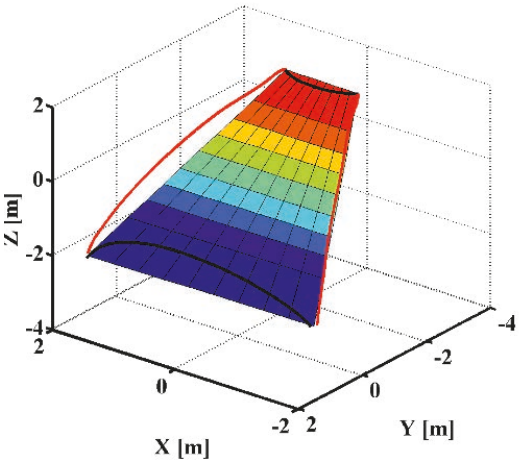

Fig. 6: The bilinear interpolant of the vault's four corner points

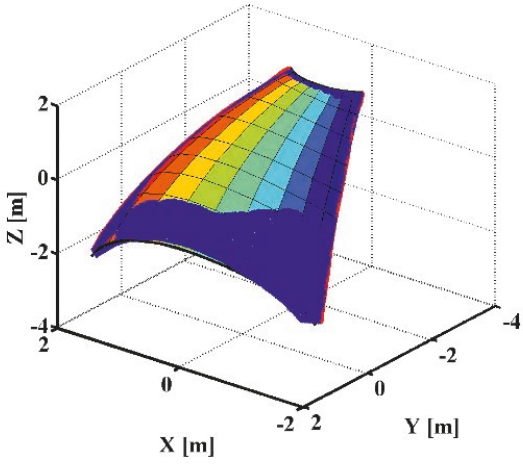

Fig. 7: The vault's Coons patch

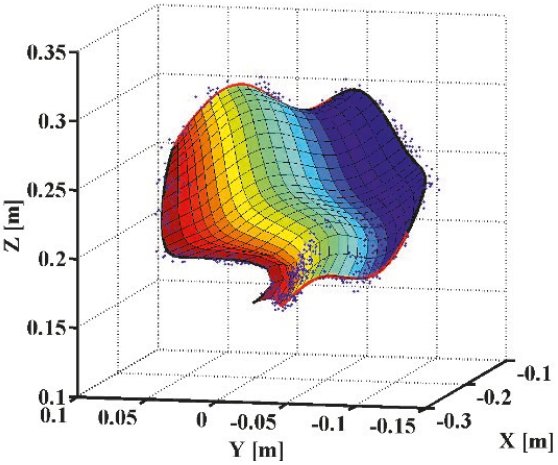

Fig. 8: The leaf's Coons patch

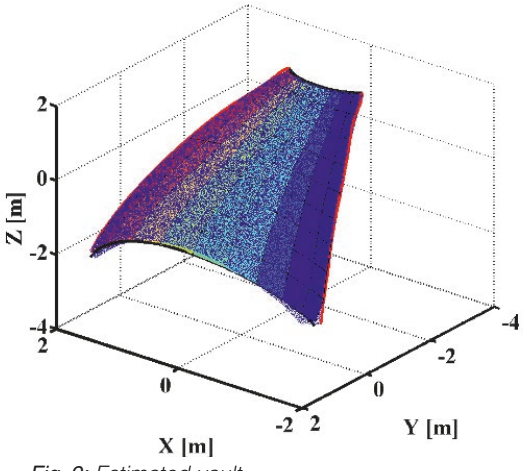

Fig. 9: Estimated vault

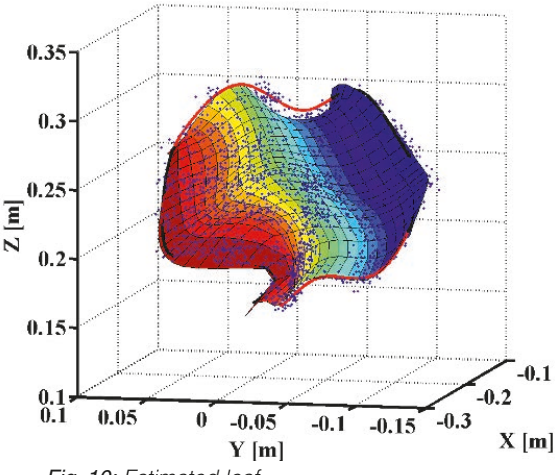

Fig. 10: Estimated leaf

The requested patch $P(u_C,v_C)$ results as the combination of these three surfaces [12]:

$$P(u_C,v_C) = R_u(u_C,v_C) + R_v(u_C,v_C) - B(u_C,v_C). \quad (9)$$

The vault's and the leaf's patch can be seen in the Figures 7 and 8. Both Figures show that a Coons patch meets the base surface's requirements mentioned above, so that now a base surface exists onto which the observations can be projected to perform the parameterization.

In order to project the points onto the Coons patch, the base surface is subdivided into quadrilaterals which are supposed to be approximately planar (cf. [12]). By means of a principal axis transformation the measured points are transformed into the coordinate system of the nearest quadrilateral, denoted by x^q, y^q, z^q in the following. The respective z^q-axis is parallel to the patch's normal vector. As a consequence, the points can be projected to the quadrilateral by discarding that coordinate which contains least information (z^q-coordinate), leaving the coordinates x^q and y^q to each observation. These coordinates form the basis for the determination of the related surface parameters u and v. As for each of the quadrilateral's four corner points the respective Cartesian coordinates x_j^q and y_j^q ($j = 0,\ldots,3$) as well as associated the parameters u_j and v_j are known, the observation's requested parameters u and v can be computed by the inverse bilinear interpolation of the quadrilateral's corner points.

3.3 Iterative improvement of the parameterization

The parameters determined in this way can now be used to estimate a best-fitting B-spline surface $S(u,v)$ (cf. section 2). For the setup of the stochastic model the observations are assumed to be equally accurate and uncorrelated. The Figures 9 and 10 show the results of the surface estimation for the vault as well as for the leaf.

The estimated surfaces approximate the point clouds in a better way than the initial base surfaces do. This statement is supported by the numerical values of the point clouds' mean deviations from Coons patch $\bar{d}_C$ as well as from the estimated surface $\bar{d}_S$: The vault's mean deviation reduces from $\bar{d}_C^V = 0{,}05\,\text{m}$ to $\bar{d}_S^V = 7{,}5 * 10^{-4}\,\text{m}$. Similarly, the leaf's mean deviation decreases from $\bar{d}_C^L = 0{,}004\,\text{m}$ to $\bar{d}_S^L = -2{,}4 * 10^{-16}\,\text{m}$. The smaller the values, the better the respective surface approximates the point cloud. As a consequence, the estimated surfaces fulfil the base surfaces' requirements in a better way than the Coons patch does. Thus, a reparameterization based on the estimated surface gives reasons to expect a better result of the adjustment.

3.3.1 Reparameterization

Taking the requirement into account that the base surface's parameterization should reflect the shape of the surface to be estimated as well as possible, at first a new parameter space is defined. The basis of this new parameter space is formed by isolines on the estimated surface each one being reparameterized by means of the cumulative chord length method (cf. equation (2)). Based on this new parameter space, it is possible to allocate improved parameters to the observations. In this way the parameterization is improved iteratively until the process converges. The whole parameterization procedure is summarized in Figure 11 schematically.

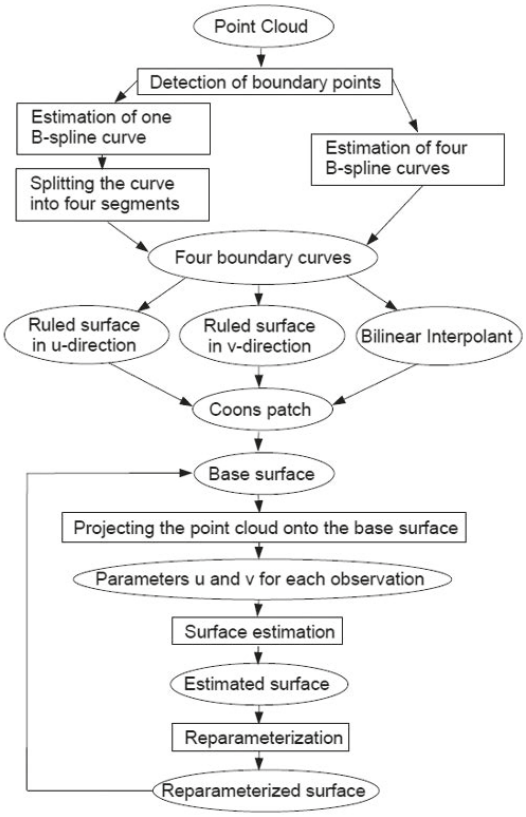

Fig. 11: Parameterization procedure

3.3.2 Introduction of constraints

The iterative adaption of the parameter values leads to artefacts in edge regions with low point densities after just a few iterations (see Figure

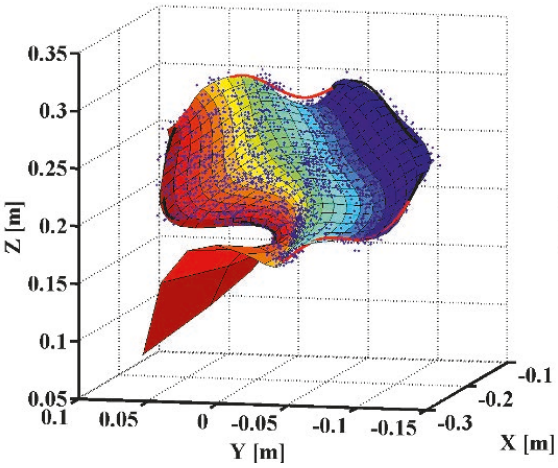

Fig. 12: Artefact in the leaf's edge area (please note the changed range of the z-axis)

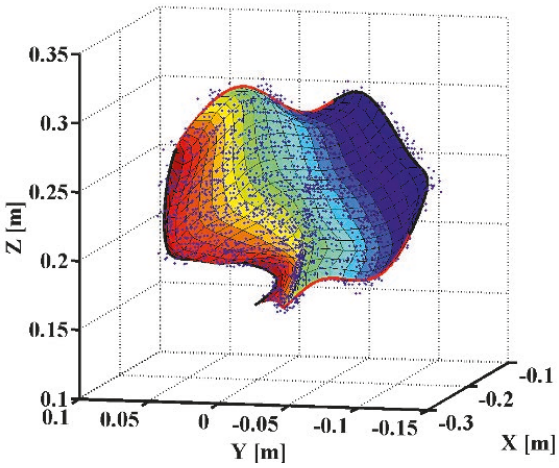

Fig. 13: Constrained estimation of the leaf

12). Consequently, the parameterization does not converge. In order to counteract the surface's degeneration, the knowledge about the surface's limitation is introduced into the adjustment by forcing the surface's edges onto the point cloud's known boundary curves:

$$S(0,v) = C_0(v) \tag{10}$$

$$S(1,v) = C_1(v) \tag{11}$$

$$S(u,0) = C_0(u) \tag{12}$$

$$S(u,1) = C_1(u). \tag{13}$$

As the curve's characteristics are determined by the control polygons and as these polygons can be handled much easier than the continuous curves, the constraints are based on the control polygons: The estimated curve control polygons $\hat{P}^k_{i_C}$ and $\hat{P}^l_{j_C}$ with $k,\ l = 0,\ 1$ are treated as known values in the surface estimation. The aim of the adjustment is the determination of the surface control points P_{ij}. Regarding the constraints, only the outermost control points P_{i0}, $P_{\mathfrak{J}}$, P_{0j} and P_{mj} are of interest.

To provide a better overview, only the case is considered, where the curves' degrees as well as the number of control points are identical with those of the surface to be estimated ($n_C = n,\ m_C = m,\ p_C = p,$ and $q_C = q$). In this case the outermost surface control polygons can be aligned with the curve control polygons by means of the following constraints:

$$\hat{P}^0_{i_C} = P_{i0} \tag{14}$$

$$\hat{P}^0_{j_C} = P_{0j} \tag{15}$$

$$\hat{P}^1_{i_C} = P_{\mathfrak{J}} \tag{16}$$

$$\hat{P}^1_{j_C} = P_{nj}. \tag{17}$$

These constraints are introduced in terms of pseudo observations (see [13]), so that the constraints' influence on the adjustment's result can be controlled by the corresponding weights. The constraints' introduction provides the desired result (see Figure 13): The edge areas are stabilised and the adjustment converges already after few iterations.

Comparing the isolines in the Figures 13 and 10, the reparameterization's influence on the estimated surface becomes visible: While in the first iteration step especially the inner isolines are clinched, the isolines' distances are quite uniform after the reparameterization.

3.4 Parameterization as a basis for datum definition

The classical deformation analysis relies on geodetic networks, whose points are linked by geodetic measurements [14]. The network's seven datum parameters (translations, orientations and scale factor) are introduced by means of datum points [15].

The areal deformation analysis also requires a common reference framework in order to reveal deformations between several measurement epochs. Therefore, the datum definition is also essential when realising areal approaches.

As the base surface's parameter lines define a coordinate system, it seems natural to build up the datum definition from the parameterization. In this case the coordinate system's origin is specified by the base surface's point $S(u = 0,\ v = 0)$. Two of the required coordinate axis are

defined by the isolines $u = 0$ and $v = 0$, so that a curvilinear coordinate system results. The remaining third axis is specified by the surface normal in the system's origin. A significant difference to classical coordinate systems is the definition of the scale factor: Usually a constant scale factor is defined for each coordinate direction, whereas, as the parameter-lines do not run equidistantly, the scale factor varies all over the surface when the datum definition is based on the parameterization. The scale factor along the third coordinate axis, however, can be chosen equidistant.

Naturally, as the parameterization changes during the iterative reparameterization process, the datum definition changes too. However, as the intermediate results are only used to achieve a final parameterization and consequently have no influence on further computations, the associated datum definitions are irrelevant; only that datum definition which belongs to the final parameterization is of importance.

Regarding deformation analysis, not only the datum definition matters, but also the datum's consistency during several measurement epochs [14]. In order to guarantee this consistency, the final base surface of the first measurement epoch has to act as a base surface for the subsequent measurement epochs. When strong deformations occur, this base surface is no longer a good approximation of the point cloud, so that a deterioration of the parameterization has to be expected. For this reason, the following considerations are made under the justified assumption that in engineering geodesy the deformation is small compared to the object size.

Further problems occur, when the object edges change compared to those of the first measurement epoch during the investigation period. If this change is caused by a mere rigid body motion, a new temporary base surface can be defined for the subsequent measurement epoch. Regarding the control points of the two surfaces as homologue, the rigid body motions' translational and rotational parameters can be determined by a similarity transformation and the point cloud of the subsequent epoch can be transformed. Afterwards, a parameterization on the basis of the base surface defining the datum is possible.

If, however, the object deforms, a datum definition based on the parameterization will not be possible: If the point cloud expands beyond the base surface's boundaries, parameters > 1 and/or < 0 will occur. If the point cloud contracts, the edge regions will be poorly or even not at all filled, so that a singular normal equation system results.

A datum definition based on the parameterization is thus suitable only for special cases (small deformations compared to the object size and unchanged object boundaries as long as no mere rigid body motion occurs). For the general case, however, the datum definition has to be based on a superior and object-independent coordinate system.

4. Summary

The presented method allows a parameterization of unordered point clouds, which serves as a basis for estimating freeform surfaces. The parameterization's fundamental principle is the definition of an appropriate base surface, onto which the point cloud is projected. Depending on the number of boundary curves, either a sphere, a cylinder or Coons patch is used as a base surface. The parameterization obtained by the projection is improved iteratively, while constraints are used to stabilise the edge regions and to counteract the surface's degeneration.

Acknowledgement

The presented paper shows results developed during the research project „Integrierte raum-zeitliche Modellierung unter Nutzung korrelierter Messgrößen zur Ableitung von Aufnahmekonfiguationen und Beschreibung von Deformationsvorgängen (IMKAD)“ (1706-N29), which is funded by the Austrian Science Fund (FWF).

References

[1] DGK Sektion Ingenieurgeodäsie, Workshop „Flächenrepräsentation“, Rhön-Park. 2013.

[2] M. Schmidt, D. Dettmering, and F. Seitz, „Using B-Spline Expansions for Ionosphere Modeling“, in Handbook of Geomathematics, W. Freeden, M. Z. Nashed, and T. Sonar, Ed. Berlin, Heidelberg: Springer Berlin Heidelberg, 2013, p. 1–40.

[3] C. Schmitt, H. Neuner, and I. Neumann, „Strain detection on bridge constructions with kinematic laser scanning“, Proceedings of the 2nd Joint International Symposium on Deformation Monitoring, 2013.

[4] K.-R. Koch, „NURBS surface with changing shape“, Allgemeine Vermessungsnachrichten, no. 117, p. 83–89, 2010.

[5] L. A. Piegl and W. Tiller, The NURBS book. Berlin; New York: Springer, 1997.

[6] M. G. Cox, „The Numerical Evaluation of B-Splines“, IMA J. Appl. Math., vol. 10, no. 2, p. 134–149, 1972.

[7] C. de Boor, „On calculating with B-splines“, J. Approx. Theory, vol. 6, no. 1, p. 50–62, 1972.

[8] W. Ma and J. Kruth, „Parameterization of randomly measured points for least squares fitting of B-spline curves and surfaces“, Comput.-Aided Des., vol. 27, no. 9, p. 663–675, 1995.

[9] K. Meyberg und P. Vachenauer, Differential- und Integralrechnung, Vektor- und Matrizenrechnung. Berlin: Springer, 2003.

[10] C. Harmening, „Raum-zeitliche Segmentierung von natürlichen Objekten in stark verdeckten Szenen“, Master thesis (unpublished), Leibniz Universität Hannover, 2013.

[11] G. E. Farin, Curves and surfaces for CAGD a practical guide. San Francisco, CA; London: Morgan Kaufmann ; Academic Press, 2002.

[12] L. A. Piegl and W. Tiller, „Parametrization for surface fitting in reverse engineering“, Comput.-Aided Des., vol. 33, no. 8, p. 593–603, 2001.

[13] W. Niemeier, Ausgleichungsrechnung: Statistische Auswertemethoden. Berlin: De Gruyter, 2008.

[14] H. Pelzer, Ingenieurvermessung: Deformationsmessungen, Massenberechnung : Ergebnisse des Arbeitskreises 6 des Deutschen Vereins für Vermessungswesen (DVW) e. V. Stuttgart: Wittwer, 1987.

[15] O. Heunecke, H. Kuhlmann, W. Welsch, A. Eichhorn, und H. Neuner, Handbuch Ingenieurgeodäsie: Auswertung geodätischer Überwachungsmessungen. Heidelberg, Neckar: Wichmann, H, 2013.

Contacts

Dipl.-Ing. Corinna Harmening, Department für Geodäsie und Geoinformation, Forschungsgruppe Ingenieurgeodäsie, Technische Universität Wien, Gußhausstraße 25-29, 1040 Wien, Austria.
E-Mail: corinna.harmening@geo.tuwien.ac.at

Prof. Dr.-Ing. Hans Neuner, Department für Geodäsie und Geoinformation, Forschungsgruppe Ingenieurgeodäsie, Technische Universität Wien,Gußhausstraße 25-29, 1040 Wien, Austria.
E-Mail: hans.neuner@geo.tuwien.ac.at

Ambiguity fixing in real-time PPP – Determination of uncalibrated phase delays using a regional network




Fabian Hinterberger, Robert Weber, Wien; Katrin Huber, Roman Lesjak, Graz

Abstract

In the last years real-time Precise Point Positioning (PPP) became a well-known GNSS positioning technique which is nowadays already used for various applications. Combining precise satellite positions and clock corrections with zero-difference observations from a dual-frequency GNSS receiver PPP is able to provide position solutions at decimeter to centimeter level. However, these corrections are insufficient to fix the ambiguities, which is why PPP still suffers from long initialization periods until the solution converges to the desired accuracy. This long convergence time is one of the most limiting factors of real-time PPP with regard to numerous applications. This contribution shall give an overview on the work performed in the research project PPPServe (funded by the Austrian Research Promotion Agency – FFG), which aimed at the development of appropriate algorithms for real-time PPP with special emphasis on the ambiguity resolution of zero-difference observations. It shall especially deal with the process and obstacles of calculating the so-called wide-lane and narrow-lane phase-delays which allow PPP-base ambiguity fixing in real-time. Furthermore, the achieved quality and the temporal stability of the estimated phase delays as well as the coordinate convergence period and coordinate quality achieved at the rover site will be discussed on basis of the most recent results.

Keywords: GNSS, Precise Point Positioning, ambiguity fixing, convergence time

Kurzfassung

In den letzten Jahren hat sich die präzise Einzelpunktbestimmung (PPP) in Echtzeit zu einer namhaften Technologie für die Positionsbestimmung mit Hilfe von Globalen Navigationssatellitensystemen (GNSS) entwickelt, die heutzutage schon für diverse Anwendungen zum Einsatz kommt. Durch die Kombination undifferenzierter Beobachtungen eines Zweifrequenz GNSS Empfängers mit präziser Satellitenbahn- und Uhrinformationen ermöglicht PPP eine Positionsbestimmung im Zentimeter- bis Dezimeterbereich. Allerdings reichen diese Korrekturen nicht aus um die Mehrdeutigkeiten zu fixieren, weshalb PPP sehr lange Initialisierungszeiten benötigt, um die gewünschte Positionsgenauigkeit zu erreichen. Diese langen Konvergenzzeiten sind in Hinblick auf zahlreiche Anwendungen der größte limitierende Faktor von PPP. Dieser Beitrag soll einen Überblick über das Projekt PPPServe (gefördert durch die österreichische Forschungsförderungsgesellschaft – FFG) geben. Ziel dieses Projektes war die Entwicklung geeigneter Algorithmen für Echtzeit PPP mit dem Schwerpunkt der Mehrdeutigkeitslösung von undifferenzierten Beobachtungen. Dieser Beitrag beschäftigt sich im speziellen mit dem Prozess und den Problemen bei der Berechnung der sogenannten wide-lane und narrow-lane Phasenverzögerungen, welche eine Fixierung der Mehrdeutigkeiten in Echtzeit PPP erlauben. Des Weiteren werden die erreichte Genauigkeit und die temporale Stabilität der berechneten Phasenverzögerungen, sowie die Güte der am Rover ermittelten Position an Hand der aktuellsten Resultate diskutiert.

Schlüsselwörter: GNSS, Precise Point Positioning, Mehrdeutigkeitsfixierung, Konvergenzzeit

1. Introduction

1.1 Principles of PPP

Precise Point Positioning is a GNSS based positioning technique that utilizes undifferenced single- or dual-frequency code and phase observations from a single GNSS receiver. A precise position can be determined due to the compensation for orbit and clock inaccuracies by using precise orbit and clock corrections. The concept of PPP was first introduced in the 1970s by R. R. Anderle, and was characterized as a single station positioning with fixed precise orbit solutions and Doppler satellite observations [1]. Nevertheless, GPS positioning was dominated by relative techniques until the late 1990's. First investigations using dual frequency data from a single GPS receiver for a few cm-positioning in post-processing mode have been published by [2].

Combining the precise satellite positions and clocks with observations from a dual-frequency GNSS receiver (to remove the first order effect of the ionosphere), PPP is able to provide position solutions at decimeter to centimeter level. The beauty of this zero-difference technique is that it does not require access to observations from one or more close reference stations accurately-surveyed. Furthermore it provides an absolute position instead of a relative location as RTK does. The only products required for PPP are precise orbit and clock data, based on measurements from reference stations from a relatively sparse station network (thousands of km apart would suffice). Nevertheless the PPP technique is still less popular than RTK, since it requires a longer convergence time to achieve maximum performances (in the order of tens of minutes). While in the last years a lot of post-processing services offering PPP arose, real-time PPP is still in an incipient development phase due to a lack of precise real-time products. Only a handful of organizations, e.g. the IGS real-time service, started offering real-time products.

One of the main challenges with PPP is the integer ambiguity resolution. Simple integer ambiguity fixing is prevented by the presence of uncalibrated phase delays (UPDs) originating from oscillator-induced time delays of the satellite and the receiver. Therefore in PPP usually a real-valued bias is estimated in place of the integer ambiguity. However the estimation of real-valued ambiguities requires a large convergence period which is the most significant factor limiting wider adoption of PPP. Accordingly, integer ambiguity resolution of undifferenced carrier phase observations is considered as one of the innovative issues for current GNSS research and applications [3].

1.2 Problems preventing PPP integer ambiguity resolution

In PPP the usual practice when processing dual frequency data is to build the ionosphere-free (IF) linear combination of the pseudo-range $P^i_{k,1}$ and $P^i_{k,2}$ and phase observations $L^i_{k,1}$ and $L^i_{k,2}$ in order to eliminate the effect of ionosphere. Assuming that the satellite clock and orbit errors are accounted for by using precise orbit and clock products and that the systematic errors are eliminated the ionosphere-free code and phase observation can be expressed as follows:

$$P^i_{k,3} = \frac{f_1^2 P^i_{k,1} - f_2^2 P^i_{k,2}}{f_1^2 - f_2^2} = \rho^i_k + c\delta t_k + \delta_{tro} + \varepsilon_{P,3} \quad (1)$$

$$L^i_{k,3} = \frac{f_1^2 L^i_{k,1} - f_2^2 L^i_{k,2}}{f_1^2 - f_2^2} = \rho^i_k + c\delta t_k + \delta_{tro} + \lambda_3 B^i_{k,3} + \varepsilon_{L,3} \quad (2)$$

where the subscript k refers to a receiver and subscript i to a satellite, f_1 and f_2 denote the carrier-frequencies of the pseudo-range and phase observations, ρ^i_k denotes the geometric distance between the satellite and the receiver, δt_k the receiver clock error scaled by the speed of light c, δ_{tro} the slant tropospheric delay, $\lambda_3 B^i_{k,3}$ the IF ambiguity scaled by the corresponding wavelength λ_3 and $\varepsilon_{p,3}$ and $\varepsilon_{L,3}$ denote the noise of the code and phase measurements, respectively. Taking the UPDs into account the IF ambiguity parameter $B^i_{k,3}$ can be written in the following form:

$$B^i_{k,3} = N^i_{k,3} + \Delta\phi^i_3 - \Delta\phi_{k,3} \quad (3)$$

with $\Delta\phi^i_3$ and $\Delta\phi_{k,3}$ being the transmitter and receiver specific UPDs and $N^i_{k,3}$ being an integer number of wavelengths. Usually the UPDs or any linear combination of them are not integer values, thus prevent the fixing of ambiguities to integers.

Figure 1 illustrates an example of a typical PPP float solution. It shows the north, east and up position differences (with respect to the reference position) of a generated float solution of the IGS station Graz-Lustbühel using dual-frequency data and precise orbit and clock products. As it can be seen after some tens of minutes the horizontal position is within a few cm while the height difference is at approximately 1 dm.

In Figure 2 the IF float ambiguity of PRN 15 corresponding to the PPP float solution presented before is shown. Due to the presence of

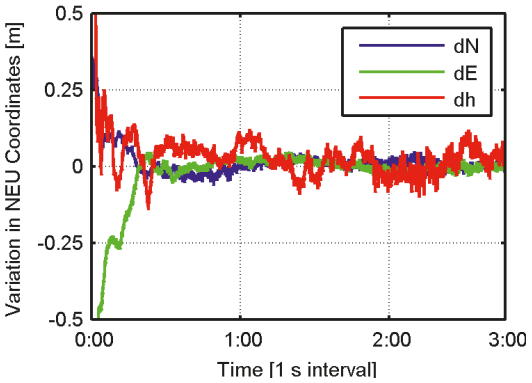

Fig. 1: Float solution of station GRAZ

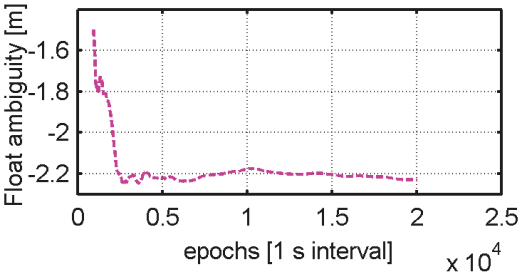

Fig. 2: Transient behavior of float ambiguity of PRN 15

the phase delays the ambiguity estimate lost its integer nature. As it is illustrated in the example the ambiguity parameters seems to be stable after an initialization time of 3000 epochs (interval of 1 s). This time is correlated to the initialization time of the position solution.

2. Project Work

To comply with the aforementioned challenge, the research project "Network based GNSS Phase Biases to enhance PPP Applications – A new Service Level of GNSS Reference Station Provider" (PPPServe) started in April 2012. The project aimed at the provision of UPDs which are the missing link at the user side to allow for real-time PPP based phase ambiguity resolution. The Technische Universität Wien, Forschungsgruppe Höhere Geodäsie (lead), the Graz University of Technology, former Institute of Navigation and the former Wien-Energie Stromnetz GmbH contributed to this project which has been successfully completed in November 2013.

2.1 Concept

During the last years several approaches to recover the integer nature of zero-difference phase ambiguities to perform integer PPP have been developed (see [4], [5], [6] and [7]). Thereby integer resolution is achieved by applying improved satellite products where the UPDs are separated from the integer ambiguities. The concept for the estimation of the UDPs which was developed in context of the project is based on an approach called "phase recovery from fractional parts" which was presented in a study of [6] for the first time. In this approach the undifferenced ambiguities are decomposed into wide-lane WL and narrow-lane NL ones. Thereby, a satellite-to-satellite single-difference (SD) is used to eliminate the receiver-dependent calibration biases. Within a network of reference stations the WL phase biases are determined from averaging the fractional parts of all WL-estimates using the Melbourne-Wübbena combination of the measurements. The NL phase biases are similarly determined by averaging the fractional parts of all NL ambiguity estimates derived from the WL ambiguities and the IF observables. The estimated phase biases can then be applied to ambiguity estimates of single-receivers to recover their integer nature.

Based on the aforementioned approach a fully functional system consisting of a network-side and a user-side module was developed (see Figure 3). The network-side module allows for the estimation of WL and NL UPDs in relation to one chosen reference satellite using observations of a regional network of GPS stations. These corrections can be used by the user-module that applies the calculated UPDs in a modified PPP algorithm to enable integer ambiguity resolution on the basis of wide- and narrow-lane observables. Details on PPPServe and its general system overview can be found in [8].

2.2 Server-side algorithms

In the following especially the algorithms for the estimation of the WL and NL UPDs implemented in the network-side module will be presented. As previously mentioned the UPDs are decomposed into WL and NL ones, which are related to the ambiguity parameter of the IF linear combination $B^i_{k,3}$ (see [9]) according to

$$B_3^{i,j} = \frac{c}{f_1^2 - f_2^2} B_{NL}^{i,j} + \frac{cf_2}{f_1^2 - f_2^2} B_{WL}^{i,j} = \\ = \frac{c}{f_1^2 - f_2^2}\left(N_{NL}^{i,j} + \Delta\phi_{NL}^{i,j}\right) + \\ + \frac{cf_2}{f_1^2 - f_2^2}\left(N_{WL}^{i,j} + \Delta\phi_{WL}^{i,j}\right). \quad (4)$$

This equation is already given at the single difference level (differences between the satellites i and j) in order to eliminate the receiver specific UPD. Subsequently, the index k has been omitted for simplification. The wide-lane part $B_{WL}^{i,j} = N_{WL}^{i,j} + \Delta\phi_{WL}^{i,j}$ and the narrow-lane part $B_{NL}^{i,j} = N_{NL}^{i,j} + \Delta\phi_{NL}^{i,j}$ both consist of the respective integer ambiguity $N^{i,j}$ plus the corresponding satellite specific UPD $\Delta\phi^{i,j}$ originating from oscillator-induced time delays of the satellite while the receiver specific UPD has been eliminated. The WL and NL UPDs cannot be estimated simultaneously therefore a stepwise estimation process is applied which will be described in the next paragraphs.

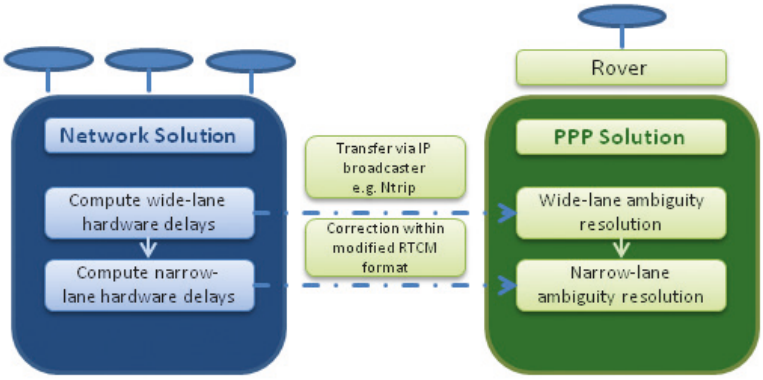

Fig. 3: Concept of the PPPServe System

Determination of the reference satellite

As mentioned above, the parameter estimation is based on the combination of SD observations. In order to be able to use the SD observations of all stations for the parameter estimation it is necessary to choose a common reference satellite. Therefore, a reference satellite must be selected prior to the estimation of the UPDs. Using only a regional network (Figure 4 illustrates the regional station network used by the PPPServe system) simplifies the selection of the reference satellites since the satellite is usually in the field of view at most of the stations. To keep it simple the satellite which is visible at most of the stations is chosen as reference satellite. Since data of a regional network is utilized the reference satellite has to be changed from time to time. Such a change also needs to be considered in the parameter estimation.

Estimation of the wide-lane UPDs

For the estimation of the WL UPDs the Melbourne Wübbena linear combination (MW) of all observations of the station network is built. The

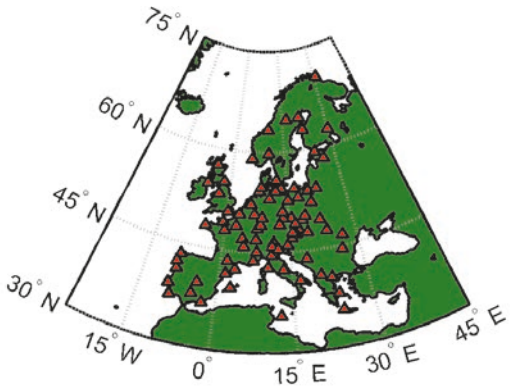

Fig. 4: Reference station network

MW combination is a linear combination of both, carrier phase (L1 and L2) and code (P1 and P2) observables. It eliminates the effect of the ionosphere, the geom etry, the clocks and the troposphere and provides a noisy estimation of the wide-lane ambiguity according to the following equation:

$$L^i_{k,WL} = \lambda_{WL}\left(N^i_{k,WL} + \Delta\phi^i_{WL} - \Delta\phi_{k,WL}\right) + \varepsilon_{WL} \quad (5)$$

where λ_{WL} is the wavelength of the WL combination, $N^i_{k,WL}$ is the integer WL ambiguity, $\Delta\phi^i_{WL}$ and $\Delta\phi_{k,WL}$ account for the satellite and receiver specific UPDs and ε_{WL} is the measurement noise, including carrier phase and code noise. A major disadvantage of the MW combination is the increased measurement noise which is highly dominated by the noise of the code measurements which is slightly reduced by calculating the moving average of the MW combination.

In the next step every possible SD observation is built at each station, by subtracting the observations of the difference satellites from the observation of the prior chosen reference satellite. Building the difference between two ZD MW observations (Eq. 5) and dividing the equation by the WL wavelength leads to the following equation with the receiver specific UPD being eliminated

$$B^{i,j}_{WL} = \frac{Lk^{i,j}_{WL}}{\lambda_{WL}} = N^{i,j}_{WL} + \Delta\phi^{i,j}_{WL} + 2 * \varepsilon_{WL} \quad (6)$$

where $N^{i,j}_{WL}$ is the SD integer wide-lane ambiguity, $\Delta\phi^{i,j}_{WL}$ is the satellite specific SD UPD and ε_{WL} is the measurement noise which is increased by a factor of two due to the built difference. Then, the positive fractional parts of all WL ambiguities observed are estimated. Finally the SD WL UPDs corrections are estimated by combining the corresponding fractional parts of the SD WL ambiguities using a Kalman filter.

The whole procedure is depicted by the following equation:

$$\delta\Delta\phi_{WL}^{i,j} = \mathrm{Kal}\left(\mathrm{Frac}\left(\hat{B}_{WL}^{i,j}\right)\right) \quad (7)$$

where $\delta\Delta\phi_{WL}^{i,j}$ denotes the estimated SD WL UPD correction, Frac() is a function to return the fractional part, Kal() denotes the Kalman filter and $\hat{B}_{WL}^{i,j}$ denotes the SD WL ambiguities observed at the stations. One must be aware that each UPD has an integer and a fractional part, wherein the integer part cannot be separated from the integer ambiguities anyway. Therefore it is only possible to estimate the fractional part of the UPDs. However, this is sufficient to restore the integer nature of the ambiguities.

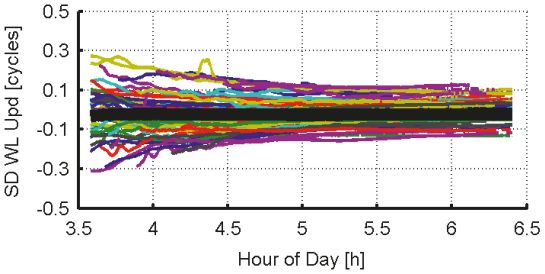

Fig. 5: SD WL UPD PRN19 – PRN32

In Figure 5 the input and output of the Kalman filter for the satellite pair PRN19 – PRN32 are shown. The fractional parts of the SD WL UPDs observed at the stations which serve as input are illustrated by the different colors. Since the network consists of more than 80 stations the same color appears several times. As it can be seen the fractional parts observed at the individual stations are very stable after a short initialization phase and the differences between them are in the range of about 0.3 cycles (one cycle corresponds to ~86 cm). In addition to the observations the UPD correction estimated as parameter of the Kalman filter is shown, which is illustrated by the slightly thicker black line.

Estimation of the narrow-lane UPDs

Following the estimation of corrections for the SD WL UPDs the estimation for the SD NL UPDs is carried out. According to Eq. 4 an estimation of the SD NL UPD correction requires a solution of the SD IF float ambiguity $B_3^{i,j}$ in the first place. The SD IF ambiguities are estimated together with the zenith tropospheric delay within a SD PPP solution at each station. All other errors are modeled or eliminated by building the ionosphere free linear combination and the difference between the observations of two satellites. Following this, the observed SD WL ambiguities are fixed using the previously estimated SD WL UPD corrections according to

$$\hat{N}_{WL}^{i,j} = \hat{B}_{WL}^{i,j} - \delta\Delta\phi_{WL}^{i,j} \quad (8)$$

The fixing is performed by a simple integer rounding of the corrected SD WL ambiguities to the nearest integer using a threshold of 0.25 cycles as fixing decision. This relative high threshold can be used due to the good wavelength/noise ration of the smoothed MW observables. After a successful fix the SD NL ambiguities can be estimated by a reformulation of Eq. 4 and the substitution of Eq. 8 according to:

$$\begin{aligned} N_{NL}^{i,j} + \Delta\phi_{NL}^{i,j} + \frac{f_2}{c\left(f_1 - f_2\right)}\left(N_{WL}^{i,j} - \hat{N}_{WL}^{i,j} + \Delta\phi_{WL}^{i,j}\right) = \\ = \frac{1}{c\left(f_1 - f_2\right)} B_3^{i,j} - \frac{f_2}{c\left(f_1 - f_2\right)} \hat{N}_{WL}^{i,j}. \end{aligned} \quad (9)$$

The difference between $N_{WL}^{i,j}$ and $\hat{N}_{WL}^{i,j}$ must not be necessarily zero which is mainly caused by the integer part of the SD WL UPD $\Delta\phi_{WL}^{i,j}$ and biases of the pseudo-range. Since both of the two terms are constant they can be merged into the SD NL UPD correction according to

$$\begin{aligned} \Delta\hat{\phi}_{NL}^{i,j} = \Delta\phi_{NL}^{i,j} + \frac{f_2}{c * \left(f_1 - f_2\right)}\left(N_{WL}^{i,j} - \hat{N}_{WL}^{i,j} + \Delta\phi_{WL}^{i,j}\right) \\ B_{NL}^{i,j} = N_{NL}^{i,j} + \Delta\hat{\phi}_{NL}^{i,j}. \end{aligned} \quad (10)$$

But this means that one has to keep consistency between the SD NL UPD correction and the related SD WL UPD correction. With the definition given in Eq. 10, Eq. 9 can be rewritten as

$$B_{NL}^{i,j} = \frac{1}{c\left(f_1 - f_2\right)} B_3^{i,j} + \frac{f_2}{c\left(f_1 - f_2\right)} \hat{N}_{WL}^{i,j} \quad (11)$$

with $B_3^{i,j}$ being the real-valued carrier-phase ambiguity estimated within the SD PPP solution and $\hat{N}_{WL}^{i,j}$ being the fixed SD WL ambiguity.

The estimation of the SD NL UPD corrections itself is carried out using the same procedure as for the estimation of the WL UPDs corrections. In a first place the positive fractional parts of the SD NL ambiguities are estimated which are subsequently combined in a Kalman filter. The main difference compared to the estimations of the WL UPDs is the stability of the NL UPDs. The NL UPDs corrections are less stable which is mainly due to the small wavelength of the NL combination which corresponds to ~10 cm as well as unmodelled effects introduced by remaining error sources (remaining troposphere and ionosphere, orbit and clock inaccuracies).

Figure 6 illustrates the input and ouput of the Kalman filter for the estimation of the SD NL

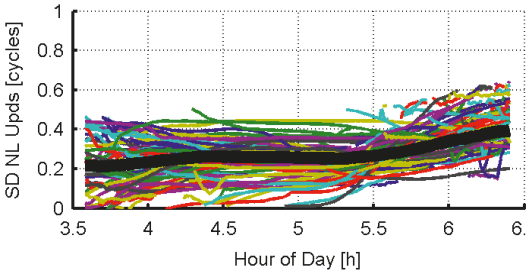

Fig. 6: SD NL UPD PRN19 – PRN32

UPD correction of the previously shown satellite pair (PRN19 – PRN32). As it can be seen the fractional parts of SD NL UPDs observed are in the range of a few tenths of a cycle only (one cycle corresponds to ~10 cm). So the solutions of the different stations are in the range of a few centimetres which leads to the conclusion that all necessary errors are modelled quite well. Another very interesting point is that the fractional parts observed are very stable. This is also true for the other SD NL UPDs. Therefore, a continuous estimate of the UPD correction is possible and no time-dependent change has to be considered in order to provide high quality biases.

2.3 Stability of the UPD corrections

Within this section the stability of the WL and NL UPD corrections will be discussed on the basis of one week of processed data. For the estimation observations of 80 stations of the EUREF network (see Figure 4) in GPS Week 1733 in combination with precise orbit and clock products from the IGS (see [10]) were used. Processing one week of data allows for the analysis of the stability of the WL and NL UPD corrections which is of interest for the estimation process itself and the update rate for transferring the UPDs to the user.

Stability of the SD WL UPD corrections

In Figure 7 the SD WL UPD corrections of three satellites (PRN13, PRN14 and PRN32) with respect to the reference satellite PRN19 are shown over the period of one week.

As it can be seen the estimated SD WL UPD corrections are not only stable during the time they are observed (usually once per day), they are also stable over much longer periods. This is also true for the solution of PRN32 even though it seems to jump. The reason for these artificial jumps is that the fractional parts of an ambiguity which is in the range of an integer, can exhibit differences of one full cycle. However, differences of one full cycle have no influence on the ambiguity fixing. In consideration of an operational service there would be two possibilities to process the SD WL UPD corrections: The first option would be to post process the UPDs with a delay of one day. The second one would be to estimate them in real-time together with the SD NL UPDs. The first option has the advantage of reduced computational burden. On the other hand, due to the high stability of corrections, it is more than sufficient to estimate them only every 15 minutes which does not need a lot of computer power.

Stability of the SD NL UPD corrections

The results of the SD NL UPD shown previously indicate that the corrections are very stable during the time they are observed. Now it is of special interest if they are also stable over longer periods. In Figure 8 the corrections of three satellites (PRN13, PRN14 and PRN32) with respect to the reference satellite PRN19 are shown overthe period of one week.

As it can be seen the estimated corrections are almost stable during the time they are observed (once per day), but contrary to the SD WL UPD corrections they are not stable over longer peri-

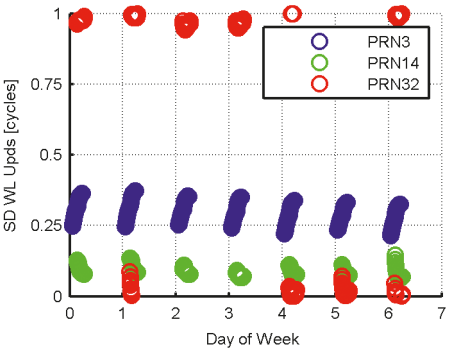

Fig. 7: Stability of SD WL UPDs

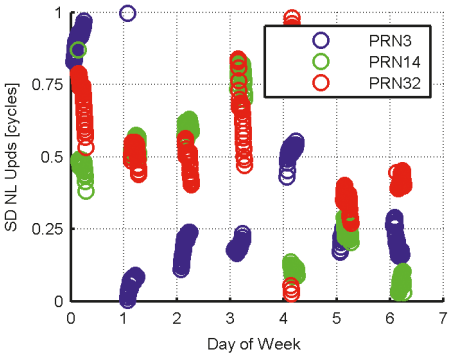

Fig. 8: Stability of SD NL UPDs

ods. Those differences are probably caused by remaining errors in the orbits and satellite clocks and errors introduced by the mapping function. One has to keep in mind that one full NL cycle corresponds to only 10 cm, so the differences between the different "daily" solutions are in the range of a few centimetres only. Furthermore two daily solutions of the estimated SD NL UPDs of PRN32 seem to drift. Those drifts may have their origin in unmodelled satellite specific errors. Due to those drifts the NL UPD corrections require a higher estimation rate compared to the WL UPDs. Since the differences are in the region of a few centimetres only a rate 10 to 30 seconds is still enough.

3. Application of the UPD corrections

In order to test the quality and reliability of the estimated corrections they were tested and evaluated using the user-side module developed at the TU Graz, where the corrections are applied to recover the integer nature of the WL and NL ambiguities. The fixed integer ambiguities can be re-introduced in the PPP solution. In case of successfully established and applied corrections the convergence of the coordinate solution should be extremely short. In other words the applied corrections should allow for an ambiguity fixing in zero-difference mode after introducing only a few epochs of observations.

To show the convergence a PPP solution with ambiguity fixing was calculated. Therefore observation data of the IGS station Graz Lustbühel (GRAZ) from DOY 87 in 2013 was used together with the precise orbit and clock products of the IGS.

As soon as the 4th narrow-lane ambiguity value is fixed to an integer – in the example illustrated in Figure 9 this happens after a couple of minutes – the horizontal position solution stays extremely stable in the surrounding of ±2 cm of the reference coordinates. In contrast to common float PPP solutions the east-component is as accurate as the north-component – this arises from the fact, that now the ambiguities are no unknowns anymore. In general it can be stated that the period required to fix the first four NL ambiguities strongly depends on the quality of corrections as well as on the satellite constellation geometry and on the quality of the approximate coordinates. Under favorable conditions the convergence time is dramatically reduced to a couple of minutes. A much more detailed investigation on the application of the corrections at the user-side module can be found in [11].

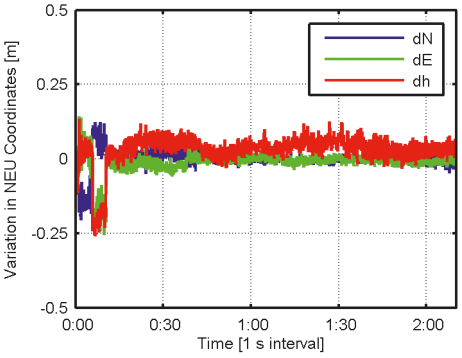

Fig. 9: PPP solution with ambiguity fixing

4. Conclusion and Outlook

This paper shows that a fully functional system enabling integer PPP was developed within the context of the project PPPServe, which is consisting of a network-side and a user-side module. The network-side module allows for the estimation of PPP-corrections to phase observables, which, on the other hand, help to recover the integer nature of WL and NL ambiguities and therefore enable ambiguity resolution at the user-side.

The WL UPD corrections are estimated using the MW combination. Due to the noise introduced by the code observations the single MW observations have to be smoothed by building the mean value over the epochs. The estimation of the WL UPD corrections is carried out using a Kalman filter. Summarizing, the WL UPD corrections are very stable over several days, which would even allow for estimating them in post processing.

The NL UPD corrections are estimated on basis of the estimated IF float and fixed integer WL ambiguities. The IF float ambiguities are generated using a standard PPP solution and the WL ambiguities are fixed to integers by means of the WL UPD corrections. The estimation of the NL UPD corrections is also carried out using a Kalman filter. Due to the relatively short wavelength of the NL combination, unmodelled remaining errors in the orbits and satellite clocks and errors introduced by the mapping function, strongly effect their estimation. This effect may lead to jumps between the different daily solutions.

Nevertheless, it could be shown that the estimated UPD corrections allow for a PPP solution with ambiguity fixing at the user-side, which is extremely precise and stable as soon as only few integer ambiguities can be fixed correctly. Under favorable conditions the convergence time is dramatically reduced to a couple of minutes.

Further, especially the east component of the coordinate solution can be strongly improved compared to a PPP float solution.

Even though the work shown in this paper was only a proof of concept, a PPP service offering UPD corrections is realizable. Possible applications for such a service are:

- Using it in areas were no RTK service is available
- Static and kinematic applications with accuracy requirements of 5–20 cm, taking into account possible long convergence times
- Independent monitoring of the stability of reference stations using PPP

Nevertheless in order to reach the performance of consolidated RTK systems PPP still faces the following challenges:

- In terms of the convergence time PPP still cannot compete with established RTK services. Contrary to RTK the convergence time strongly depends on the initial conditions
- In order to reach the same quality as RTK regional error models are required. Such models can only be derived from regional network data
- Currently there are no industry message standards that would allow for the transmission of all corrections required for PPP with ambiguity fixing. It should be noted that those standards are currently established

Nevertheless, it is expected that the number of PPP solutions will strongly increase in the next couple of years.

Acknowledgments

Financial support for the research project PPPServe came from the Federal Ministry for Transport, Innovation and Technology (BMVIT), represented by the Austrian Research Promotion Agency (FFG). PPPServe is a project of the 8th Austrian Space Applications Programme (ASAP). The PPPServe consortium consisted of the Technische Universität Wien, Department für Geodäsie und Geoinformation, Forschungsgruppe Höhere Geodäsie (lead), the Graz University of Technology, former Institute of Navigation and the former Wien-Energie Stromnetz GmbH operating a nationwide GNSS reference site network (EPOSA-Service).

References

[1] *Kouba J and Héroux P (2001)*: Precise Point Positioning Using IGS Orbit and Clock Products, GPS Solutions, Vol. 5 Nr. 2

[2] *Zumberge J, Heflin M, Jefferson D, Watkins M and Webb F (1997)*: Precise point positioning for the efficient and robust analysis of GPS data from large networks Journal of Geophysical Research 102, pp 5005-5017

[3] *Rizos C (2008)*: The Research Challenges of IAG Commission 4 „Positioning & Applications“, International Association of Geodesy Symposia 132, pp 126-132

[4] *Laurichesse D, Mercier F, Berthias J P, Broca P, Cerri L (2009)*: Integer Ambiguity Resolution on Undifferenced GPS Phase Measurements and its Application to PPP and Satellite Precise Orbit Determination, Journal of The Institute of Navigation, Vol. 56, N° 2, pp. 135-149

[5] *Collins P, Bisnath S, Lahaye F and Héroux P (2010), Undifferenced GPS Ambiguity Resolution Using the Decoupled Clock Model and Ambiguity Datum Fixing, Journal of The Institute of Navigation, Vol. 57, No. 2, pp. 123-135*

[6] *Ge M, Gendt G, Rothacher M, Shi C, and Liu J (2008)*: Resolution of GPS carrier-phase ambiguities in precise point positioning (PPP) with daily observations, Journal of Geodesy 82, pp. 389-399

[7] *Geng J, Meng X, Dodson A H and Teferle F N (2010)*: Integer ambiguity resolution in precise point positioning: method comparison, Journal of Geodesy, Vol. 85, No. 9, pp. 569-581

[8] *Huber K, Hinterberger F, Lesjak R, Weber R, Klug C and Thaler G (2013)*: PPPServe – Network based GNSS Phase Biases to enhance PPP Applications, in: „The European Navigation Conference Proceedings“, published by: ENC2013; The European Navigation Conference, 2013, ISBN: 978-3-200-03154-8

[9] *Hofmann-Wellenhof B, Lichtenegger H and Wasle H (2007)*: Global Navigation Satellite Systems – GPS, Glonass, GALILEO and more. Springer Wien New York

[10] *International Global Navigation Satellite System Service (IGS) (2013)*: IGS Quality of Service Fact Sheet, http://kb.igs.org/hc/en-us/articles/201208216 (06.02.2015)

[11] *Huber K, Hinterberger F, Lesjak R and Weber R (2014)*: Real-time PPP with ambiguity resolution – Determination and Application of Uncalibrated Phase Dealys, Proceedings of the 27th International Technical Meeting of the Satellite Division of the Institute of Navigation (ION GNSS+ 2014, 1 (2014), S. 976 – 985

Contacts

Dipl.-Ing. Fabian Hinterberger, Technische Universität Wien, Department für Geodäsie und Geoinformation, Forschungsgruppe Höhere Geodäsie, Gußhausstraße 27-29, 1040 Vienna, Austria.

E-Mail: fabian.hinterberger@tuwien.ac.at

Ao.-Univ. Prof. Dipl.-Ing. Dr.techn. Robert Weber, Technische Universität Wien, Department für Geodäsie und Geoinformation, Forschungsgruppe Höhere Geodäsie, Gußhausstraße 27-29, 1040 Vienna, Austria.

E-Mail: robert.weber@tuwien.ac.at

Dipl.-Ing. Katrin Huber, Institute of Geodesy, Working Group Navigation, NAWI Graz, Graz University of Technology, Steyrergasse 30/III, 8010 Graz, Austria.

E-Mail: katrin.huber@tugraz.at

Dipl.-Ing. Roman Lesjak, Institute of Geodesy, Working Group Navigation, NAWI Graz, Graz University of Technology, Steyrergasse 30/III, 8010 Graz, Austria.

E-Mail: roman.lesjak@tugraz.at

3D Point clouds for forestry applications

Markus Hollaus, Wien

Abstract

This article gives an overview of the state of the art 3D data acquisition systems (i.e. airborne laser scanning and digital aerial cameras) and the derivation of forestry related information from the derived 3D points clouds. The described examples are focusing on forest area delineation, growing stock and biomass estimation, forest growth assessment, forest road extraction as well as its changes. The shown examples are located in the Alpine space and discuss the possibilities and limitations of integrating these data sources into operational forestry applications.

Keywords: Forest delineation, growing stock, forest roads, image matching, laser scanning

Kurzfassung

In diesem Beitrag wird ein Überblick über gängige Erfassungsmethoden von 3D Informationen gegeben. Die Nützlichkeit derartiger 3D Informationen für die Forstwirtschaft wurde im letzten Jahrzehnt im Rahmen von wissenschaftlichen Studien und praktischen Anwendungsbeispielen im Alpinen Raum eindeutig dargestellt und belegt. Die aus der Differenz von Oberflächenmodellen und Geländemodellen berechnete normalisierte Kronenhöhe spielt dabei eine zentrale Rolle, da sich daraus direkt Baum- und Bestandeshöhen bestimmen lassen und weiterführend auch Informationen über Holzvorrat oder Biomasse durch Regressionsmodelle oder Strukturparameter mittels einer Analyse der vertikalen Punktverteilung ableiten lassen. Liegen multitemporale Daten wie zum Beispiel Oberflächenmodelle aus mehreren Zeitpunkten vor, so können Fragestellungen wie die Abschätzung der Nutzung aber auch des Zuwachses beantwortet werden. Ebenso eignen sich Airborne Laserscanning (ALS) Daten gemeinsam mit multispektralen Orthophotos für die Detektion von Forststraßen sowie deren geometrische Beschreibung. Die in diesem Beitrag beschriebenen Methoden und Beispiele wurden von der Forschungsgruppe Photogrammetrie des Departments für Geodäsie und Geoinformation der TU Wien, oftmals mit Partner aus der Wissenschaft und Praxis entwickelt und durchgeführt.

Schlüsselwörter: Waldabgrenzung, Holzvorratsschätzung, Forststraßen, Image Matching, Airborne Laserscanning

1. Introduction

Forests have a variety of functions and demands such as being habitat for animals and plants, recreation area, source for renewable resources or to fulfill protection and environmental functions. The production of renewable resources, like timber, has positive effects on climate change consequences attenuation, employment and supports a strong regional value chain, which in turn has an enormous impact on rural development. The objective of preserving and improving the efficiency of forests is a point of public interest and can only be guaranteed if the planning and implementation of all respective measures are integrated into an adequate and well known socio-economic context. Especially, the managing of forests in mountain territories is significantly more cost intensive than in plain ones. This is due to the topographic conditions, climatic adversity and limited access which drive partly the economic context. A good knowledge of the forest biomass location, its characteristics and mobilization conditions (exploitability, service roads, and mobilization costs) is therefore, a prerequisite for effective wood harvesting and transporting, which contributes to a sustainable wood industry. The available traditional in-situ forest inventories, which are commonly based on sample plots, provide this required information only with a limited spatial and temporal resolution due to the used sampling design (i.e. sample plots distributed over an area), which allows only statistical analyses for larger administrative units, and the high costs. In terms of spatial and temporal resolution remote sensing technologies have shown their high potential to acquire additional information. For the operational forest management the most important remote sensing technologies are airborne laserscanning (ALS) and digital aerial photography, which allow the derivation of three-dimensional (3D) information of forests (i.e. tree heights, stand density, horizontal and vertical forest structure).

The objective of this paper is to give an overview, how 3D information derived from these two technologies can be used for current forestry ap-

plications. In the following chapters the generations of 3D data from ALS data and digital aerial images, their availability as well as possibilities to extract forestry relevant information are described. The focus of the described methods and its applications is on studies performed at the research group Photogrammetry at the Department of Geodesy and Geoinformation (GEO) at TU Wien. Therefore, this paper doesn't include a thoroughly state of the art on an international level.

2. 3D data acquisition methods

In this article 3D data acquired with different airborne laser scanning systems as well as derived from image matching of digital aerial photos are used for deriving forestry related information. Satellite-based systems (e.g. ICESat/GLAS [1]) are not considered in this paper. In the following two chapters a short state of the art of both technologies is given.

Airborne Laserscanning

Small-footprint airborne laser scanning (ALS), often referred to as LiDAR, is an active remote sensing technique, which was originally designed to measure the topography of the Earth's surface (i.e. of forested areas). A laser mounted in a helicopter, fixed wing airplane or in an unmanned airborne platform emits short infrared pulses towards the Earth's surface and a photodiode measures the backscattered signal. The count of detectable echoes in the backscattered waveform is depending on the used sensor type and the objects within the travel path of the laser pulse. State of the art discrete laser scanner systems measure the round-trip time of multiple echoes from one emitted laser pulse, whereas full waveform (FWF) systems record the entire backscattered waveform [2]. The newest generation of ALS systems has multiple-time-around processing [3] and the capability of multiple wavelengths [4]. The final 3D coordinates of the backscattering objects are derived by the combination of all measurement quantities (e.g. the distance between the sensor and the target, the position (i.e. dGPS) and the orientation (i.e. IMU) of the sensor and the instrument mounting parameters). Further details about the physical principles of LiDAR and about ALS specifications and sensors available in the beginning phase of small-footprint ALS (i.e. 1990's) are given in Kilian et al. [5], Baltsavias [6, 7] and Wehr and Lohr [8].

To achieve a high precision georeferenced 3D point cloud inaccuracies of the individual ALS system components have to be minimized as for example presented by Kager [9], Burman [10] or Filin [11]. Direct georeferencing requires the position and orientation of the measurement platform, which are measured by dGPS and INS. The laser scanner measurements are the beam direction and the ranges per shot. Additionally, the relative orientation of the laser scanner and the navigation components (lever arm, boresight angles) need to be know. In strip adjustment the lever arm and boresight are estimated from discrepancies between overlapping strips. Additionally, systematic errors in angle and range measurements can be compensated.

Image matching

The introduction of digital cameras has restimulated the traditional stereo photogrammetry towards fully automatic 3D reconstruction of objects from multiple overlapping images. Due to good signal-to-noise ratios (digital vs. analogue detection) and high overlaps between the individual images, digital images and the all-digital workflow have advantages compared to scanned analogue ones with respect to accuracy, reliability and density of automatic point measurement [12]. The principle of image based 3D reconstruction consists of detecting and matching corresponding image features (e.g. points) across two overlapping images. And then, the coordinates of the corresponding 3D object are computed using spatial intersection.

Image matching algorithms can be classified in different manners. Matching may either be performed for salient points or at regular pixel positions (e.g. every n-th pixel). Also, correspondences between points in the images may be found by local or global optimization techniques. Three groups of algorithms are currently used: local area-based [e.g. 13], local feature-based [e.g. 14] and (semi-)global cost-based matching [e.g. 15, 16]. This classification reflects also the historical development of the methods. Other possibilities of categorizing matching approaches are sparse and dense matching or local and global matching methods. An overview of the development of image matching techniques in photogrammetry can also be found in Gruen [17].

For area-based matching, points are selected only in one image, whereas the corresponding points in the other image are found by correlation. This type of matching methods is less robust, slow and needs good initial approximations

but it is capable of achieving very high matching densities. By using least squares matching [13], which is an evolved variant of area-based matching, very high accuracies (~1/10 pixel) are possible.

Feature-based matching methods extract salient features (usually points) together with descriptive attributes (like grey level gradients) in the overlapping images independently and match corresponding image features as the nearest neighbors in the descriptor space. This type of methods is highly robust, fast, needs only a coarse initial approximation and can achieve accuracies of ~1/3 pixels.

Semi-global matching [15] is a dense image matching method that uses a semi-global optimization. Thereby, for each pixel in the first image the corresponding pixel in the other image is searched for, by minimizing a cost function. The latter consists of the difference of a function of the pixel gray values (e. g. census transform [18]) and smoothness penalty terms. The cost function is evaluated along different paths through the image. The penalty terms increase the robustness of this approach and aim at minimizing the disparity difference of neighboring pixels. This means that neighboring 3D points at the object should have the same depth from the image pair. However, since the gray value differences and the smoothness penalty terms are competing in the cost function, obtaining very small gray value differences by hurting the penalty terms with large disparity differences (e. g. at roof edges) is still possible. As summarized in Wenzel et al. [19] the semi-global matching approach has a high matching stability even though the matching is done pixel wise, which minimizes smearing effects like for local methods.

Due to the high overlaps commonly multi-image matching is used, which reduces errors due to disturbances in the intensity distribution of the images. Most of the available matching approaches still perform a pair wise image matching (for selected pairs among all images) and afterwards compute a fusion of the derived surface models. In contrast, Rothermel and Haala [20] suggested to use an overdetermined spatial intersection based on multiple pairwise image matching with one central/master image.

Due to the fact that in stereo photogrammetry 3D coordinates are derived by spatial intersection areas that are visible from only one exposure position can not be reconstructed. This fact has to be considered if the matched 3D point clouds are used for forestry applications. In Figure 1 the 3D points from an ALS acquisition and the points from image matching are shown for a forest cross section. It can clearly be seen that the points along the top surface of the canopy fit well together and that only ALS points are measured within the forest canopy and at the ground. Further information about the derived 3D point clouds from different image matching approaches in comparison to ALS data can be

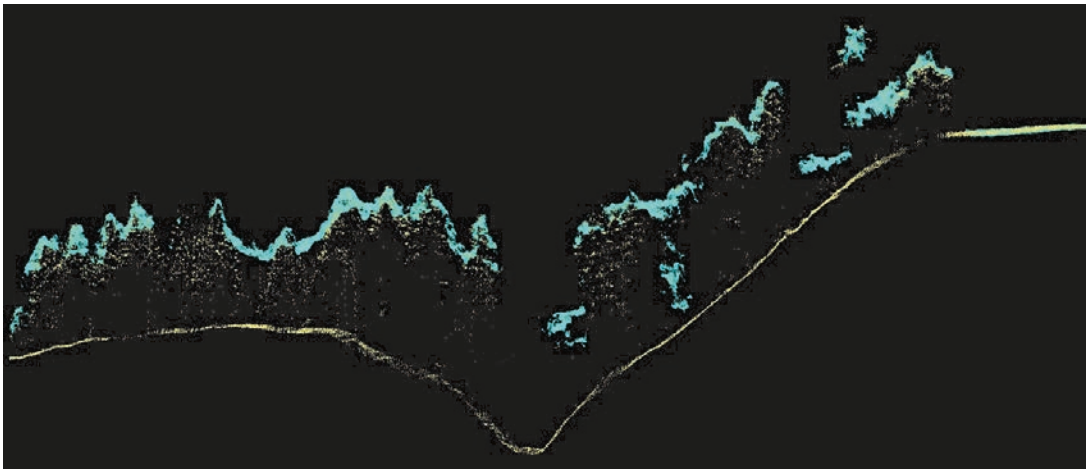

Fig. 1: Cross section of a forest scene. Length of the profile is 200 m, width 2.5 m. The yellow dots are from an ALS acquisition, the blue one from image matching. The image matching points are in the foreground. Aerial photos where acquired with an Ultra-Cam XP with a length overlap of ~80 % and a side overlap of ~50 %. The GSD is ~12.5 cm. For the matching SGM within SURE was applied. The ALS data was acquired in April 2011 with an average laser shot density of ~20 shots/m^2.

found for example in Baltsavias et al. [21] and White et al. [22].

Derivation of topographic models

From the 3D point cloud topographic models, such as the digital terrain model (DTM), the digital surface model (DSM) and the normalized digital surface model (nDSM) are derived. A clear definition of these models can be found in Pfeifer [23].

For the studies outlined at the research group Photogrammetry at TU Wien, the DTMs were calculated using the hierarchic robust filtering approach described in Kraus and Pfeifer [24], implemented into the software Scop++ [25]. An overview of alternative filtering algorithms can be found in Sithole and Vosselman [26]. For forested areas the DTM can only be derived from ALS data because the 3D points from image matching represent the top canopy surface and the terrain for larger forest gaps only. Therefore, it is not possible to derive an appropriate DTM in areas covered with dense forests from matched point clouds. For the calculation of the DSMs a land cover dependent derivation approach [27] is commonly applied. This approach uses the surface roughness to combine two DSMs that are calculated based (i) on the highest 3D point per raster cell (DSM_{max}) and (ii) on moving least squares interpolation (DSM_{mls}) of a local point cloud.

For the final DSM the DSM_{max} is selected for rough surfaces (i.e. forests, building borders, etc.) and the DSM_{mls} for smooth surfaces such as non-forested areas, building roofs, etc. and for raster cells where DSM_{max} is nodata. The nDSM is calculated by subtracting the DTM from the DSM. In addition to these topographic models slope adaptive echo ratio (sER) maps [28], as a measure for local transparency and roughness of the top-most surface, are commonly calculated. The sER map is a useful information source within the forest area delineation workflow. The spatial resolution of the derived raster models is usually $1 \times 1\ m^2$. The applied workflows for calculating the topographic models as well as the subsequent forest relevant products are commonly implemented as Python scripts including Opals software [29] packages.

Data availability

In Austria the data acquisition of ALS data and aerial images is organized in different ways. The ALS data are commonly acquired in federal state wide ALS campaigns whereas each federal state defines its own requirements to the data properties. For the aerial image acquisition an Austria wide acquisition plan exists with a repetition cycle of three years. The standard properties for this acquisition are four spectral channels (i.e. red, green, blue and near infrared) with a ground sampling distance of 20 cm. More information can be found at www.bev.gv.at and at www.geoimage.at.

For the acquisition of the ALS data no Austria wide repetition cycle exists yet. Until now entire Austria is covered by ALS data, whereas the data sets are commonly available at the federal states. For the federal state Vorarlberg an ALS re-flight was already done after ~6 years in 2011. For the other federal states the discussions about a regular acquisition of ALS data have partly been started yet.

On the European level the data availability is similar for the aerial images. The situation for ALS data is diverse. For some countries a full coverage of ALS data is already available, for some other countries the data acquisitions are still ongoing.

3. Forest relevant parameter from 3D point clouds

Forest area

Forest area delineation has a long tradition in forestry and is critical as a broad field of applications (i.e. obligatory reporting) and users (i.e. governmental authorities, forest community) rely on this information. In the past mainly the 2D content of aerial images were used for a manual or semi-automated delineation. Shadow effects and varying radiometric properties of the spectral images make this process to a challenging task, particularly for detecting small forest clearings and the exact delineation of forest borders on a parcel level. Additionally, the quality of the results of a manual delineation is subjective and variable between interpreters and may lead to inhomogeneous, maybe even incorrect datasets [30].

For the practical applications of forest delineations it is essential that the used approaches can consider e.g. national and/or international forest definitions as for example, the one from the FAO (Food and Agriculture Organization of the United Nations) [31, 32]. Most of the forest definitions are based on the parameters crown coverage, minimum area and width, minimum tree height and the land use. Whereas the area, width and tree height are clearly defined parameters the

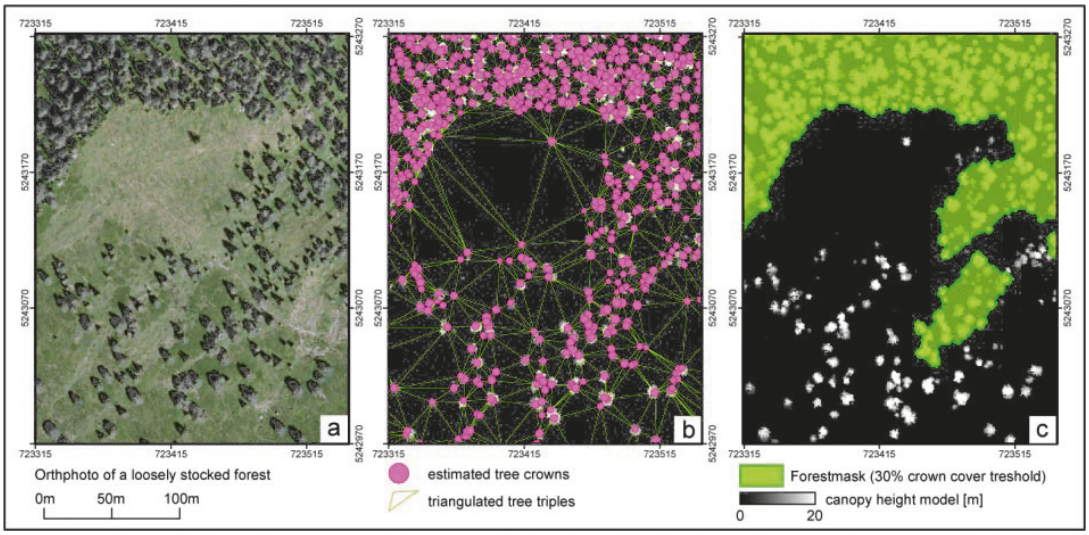

Fig. 2: Delineation of forested areas based on LIDAR data; a) orthophoto of a loosely stocked forest, b) estimated tree crowns and detected tree tripels, c) delineated forest areas (in the background is a z-coded canopy height model) © [39]

crown coverage is often not defined in a unique way, meaning the information about the reference area for calculating the crown coverage is often missing. In general, the crown coverage is defined as the proportion of the forest floor covered by the vertical projection of the tree crowns [33]. With respect to remote sensing based forest area delineation the parameter land use is commonly not extractable from the data itself and therefore, additional information is needed if the land use has to be considered. For example a Christmas tree plantation cannot be differentiated from forests in remote sensing data. Beside this limitation most of the parameters used for forest area delineation need the height information included in 3D data. As shown in Figure 1, ALS provides both the information about the terrain and the canopy surface and is therefore, an excellent data source for this application. If surface models derived from image matching are used a DTM derived from e. g. ALS is needed to calculate the tree heights. This is especially important for areas with high topographic relief energy and a low percentage of forest gaps where it is not possible to assess a reliable DTM from image matching.

In literature several approaches are available that uses 3D data from ALS data and/or images for forest area delineation [e. g. 34, 35-37]. Eysn [38] suggested a new approach for crown coverage estimation based on ALS data which has clear defined geometric properties and which works on a similar way than it is the case for manual assessment of the crown coverage based on aerial orthophotos. This approach uses the area of the convex hull of three neighboring trees as reference unit and thus, overcomes limitations from e. g. pure moving window approaches such as smoothing effects along the forest border or the dependency of the kernel size and shape of the moving window. The positions of single trees are detected by applying a local maxima filter on the nDSMs. Furthermore, Eysn et al. [30] presented a comprehensive approach for forest area delineation based on ALS data by considering the criterions tree height, crown coverage and the minimum area and width. The criterion of land use is not considered in this approach. Based on the sER map, which describes the transparency for laser beams of the top most surface, it is possible to differentiate between buildings and trees. As shown in Figure 2, a reliable and objective forest area can be derived from ALS data by applying this approach.

If ALS-based DTMs and DSMs derived from image matching are used for forest area delineation the surface roughness and/or the spectral properties of the aerial images can be used for excluding buildings from the forest mask instead of the sER map.

Growing stock and biomass

Growing stock is a key parameter in forest management and provides the basis for the estimation of biomass. The term growing stock is commonly used as a synonym for stem volume

and is given in m³/ha. Biomass is often derived from the growing stock by using tree species specific biomass expansion factors [40, 41]. For the estimation of growing stock and biomass from ALS data two principle approaches are available. The first one models individual trees [e.g. 42, 43] based on ALS data with point densities greater than e.g. 3–5 points/m² whereas the second one works on a larger scale e.g. on a plot- or stand level. These so-called area-based approaches can be applied for large areas and for ALS data with lower point density for assessing e.g. the mean canopy height (m), growing stock (m³/ha) or basal area (m²/ha). Due to their robustness this type of models are already included into operational forest inventories [e.g. 22, 44, 45-49]. The area-based approaches can further be divided into empirical, semi-empirical and physical models, whereas the application of the physical models is often limited due to missing data for the model parameterization. For the calibration of the empirical and semi-empirical regression models reference data are needed. Commonly data from local or national forest inventories (i.e. inventory plots) are used for this purpose. Often these models have the limitation of a lacking sensitivity to local forest conditions. This means that growing stock or biomass models are often calibrated for large areas (e.g. entire federal districts) and thus, local changes of the forest structure are not considered, which has the effects that the resulting models are smoothing the local situation. Within several research projects at the research group Photogrammetry at the TU Vienna, the semi-empirical regression model from Hollaus et al. [50] was applied to different strata. This model assumes a linear relationship between the growing stock/biomass and the ALS derived canopy volume, stratified according to four canopy height classes to account for height dependent differences in canopy structure. For the stratification different information obtained from remote sensing data can be used. This information can for example be a tree species classification based on aerial images as presented in Waser [51] or from full-waveform ALS data presented in Hollaus et al. [52]. In addition to tree species information crown coverage based stratification has shown a high potential to consider local forest conditions. For our studies we used the criterion "species" to classify the forest into deciduous, mixed and coniferous forest and the criterion "crown coverage" to differentiate between dense and sparse coverage. To use a stratified growing stock assessment it is beneficial if the information needed for the stratification can be derived from the analyzed data (i.e. ALS data, aerial images that are used for reconstructing the canopy surface) itself. Otherwise issues concerning different spatial resolution and acquisition times as well as geo-referencing issues have to be solved. For operational large area applications the stratification should be possible in a highly automatic way. Our studies have shown that the stratification based on the main tree species group and the crown coverage leads to an enhancement of the assessed growing stock by reducing the relative standard deviation of ~4%. Furthermore, the

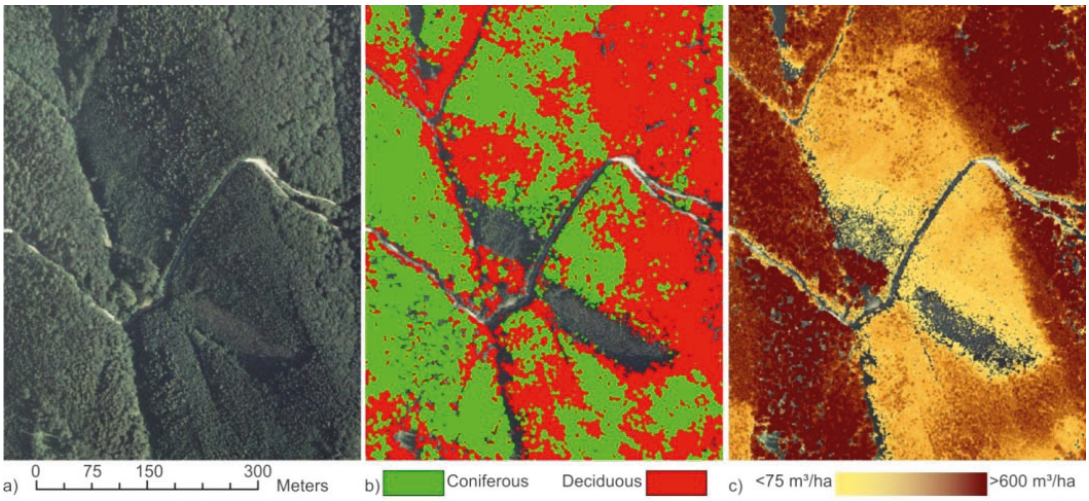

*Fig. 3: **(a)** Orthophoto © bing maps, **(b)** classified tree species map and **(c)** tree species dependent growing stock map © [57]*

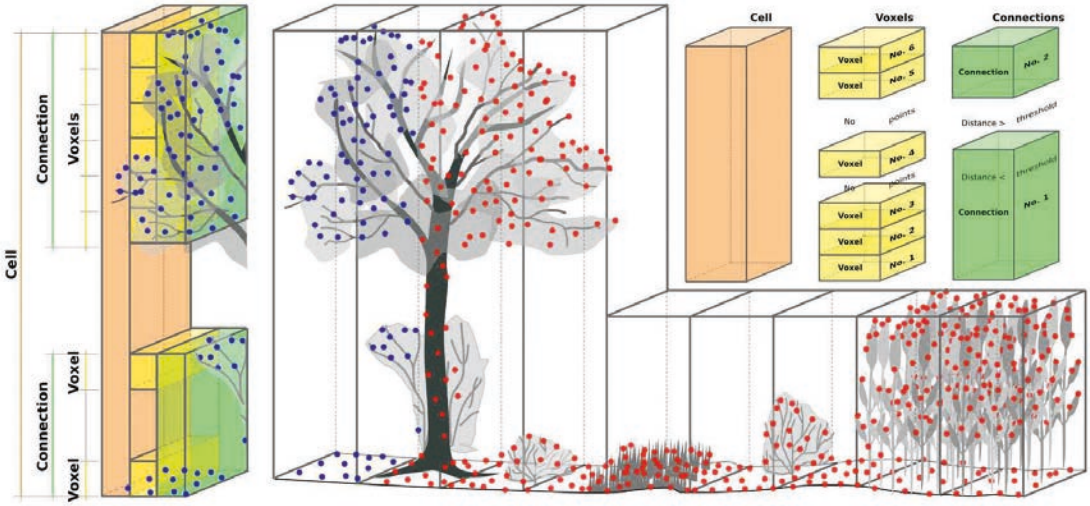

Fig. 4: Schematic view of vertical structure extraction from 3D point clouds © [68]

analyses have shown that growing stock maps with very high spatial resolution can be derived from ALS and forest inventory data. These maps allow comprehensive forest management for large areas and serve as input data for various forest planning activities. In Figure 3 an example from a stratified (i. e. coniferous and deciduous forests) growing stock map is shown. The stratification was based on full-waveform ALS data.

In literature most of the studies about growing stock estimation are based on ALS data. Due to the increasing availability of multi-epoch DSMs from image matching a research project was done together with the Austrian research center for forests (BFW) to investigate the potential of image matching in combination with ALS-based DTMs for estimating growing stock and its changes for different Austrian test sites [53]. It could be shown that compared to previous ALS studies similar accuracies of the assessed growing stock could be achieved. The high potential of 3D point clouds derived from stereo images in combination with ALS-DTMs for stem volume estimation is also confirmed in e. g. Straub et al. [54] and Bohlin et al. [55]. Finally, regional stem volume estimations derived from e. g. ALS data provide an excellent data source for calibrating as well as validating biomass models derived from optical satellite data [e. g. 56].

Forest structure

The information on horizontal and vertical forest structure and its diversity is one of the most valuable indicators for forest habitat quality assessment. Diversity of structure indicates diversity of species and also different ecological niches are created [58]. For mapping the vertical structure ALS provides excellent data because the laser beams are able to penetrate through small gaps in the top canopy surface and depict the vertical canopy structure down to the forest ground [e. g. 59, 60-63]. Especially, full-waveform ALS system sample the full backscattered pulse information, which allows the extraction of more echoes compared to discrete ALS systems [64, 65]. This makes full-waveform ALS data to an excellent data source for describing the highly complex structure of dense forests such as old unmanaged deciduous forests or tropical rainforests. An overview of the potential of full-waveform ALS data for forest structure extraction is given in Hollaus et al. [66]. In Mücke [67] different methods for extracting structure information from ALS data on pixel and plot levels are given. This structure information includes the number of vegetation layers (e. g. one-, two- or multi-layered forests) and the amount of standing and fallen deadwood. One of the most important forest structure quantities is the number and the geometric extend of the vertical vegetation layers. This information can be derived from ALS derived 3D point cloud or from 2,5D rasterized topographic models such as the nDSM derived from ALS or image

matching. Depending on the used input data (i. e. 3D point cloud, nDSM) different reference areas can be analyzed. If 3D ALS point clouds are available Vetter et al. [68] suggested a voxel-based approach for extracting detailed vertical layers. In Figure 4 it can be seen that so-called connections, which represent a forest layer, are defined by connecting voxels that are occupied by laser echoes. This type of analyzes can be done on a voxel level. Also Leiterer et al. [60] developed a physically-based extraction method of canopy structure variables on grid level. In the opposite of these analyzes the study of Maier [69] uses the nDSM as an input data, whereas larger reference units (e. g. forest stand, forest plots) are used. The canopy height is classified into three classes (i. e. height layers), which are used for classifying a forest stand for example into single- and multi-layered forests.

Change detection

The high potential of ALS data for forestry applications has been confirmed in many studies during the last decade. The open question is still the application of ALS data for monitoring applications. Due to the ALS data acquisitions costs re-acquisition are rare and only few regular acquisition plans are available until now. Consequently there is on the one hand a lack of data and on the other hand a lack of knowledge of using multi-temporal 3D data for forest monitoring tasks. Therefore, the capabilities of 3D data for operational forest monitoring applications were analyzed in several research projects.

For change detections applications it is essential that height differences between the individual topographic models originating from inaccuracies in the georeferencing are minimized. To avoid errors for example in the assessed growing stock change originating from DTM errors due to different terrain point densities one reference DTM can be used for both dates. It can be assumed that the DTM within the forests don't change during two acquisitions. Therefore, the DTM with the highest accuracy should be used, which can normally be determined from the ALS data set with the highest terrain point density. In our projects the quality checks of the topographic models have shown that even for stable objects (i. e. open areas, roofs and streets) height differences occur. For the change detection analyses of our projects these height differences were minimized by applying a least square matching (LSM). Calculating the LSM of the identified stable objects 3D shift parameters are determined and applied to one of the DSMs. Using the LSM the DSM differences could be halved (e. g. <10 cm). Due to this height adjustment the remaining height differences can mainly be connected to changes of tree heights and consequently to growing stock changes.

Based on DSM difference maps changes in the wooded land can be detected. For differentiating between exploitation and forest growth the area is classified into areas with an (a) increased (= forest growth) and (b) decreased (= exploitation) surface height. As for each 3D data set small differences in the tree crown representation

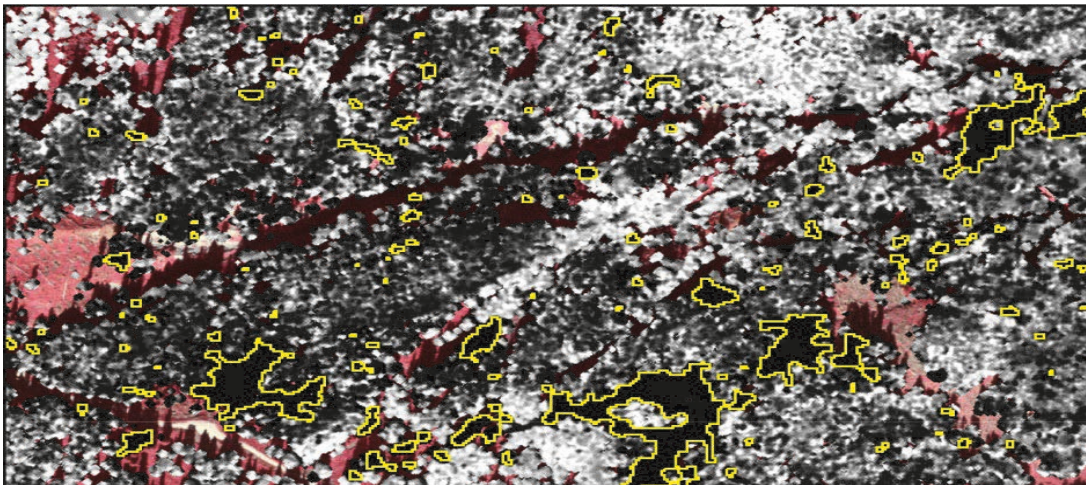

Fig. 5: Difference map of estimated growing stocks (2011–2004) overlaid with the detected outlines of the harvested forest areas. In the background a CIR orthophoto is shown [53].

within the DSMs can occur, morphologic operations (i. e. open / close) and a minimum mapping area of e. g. 10 m^2 are applied to the DSM difference map.

The calculated nDSMs are used as input for the growing stock regression models (see previous chapter), whereas each data set is calibrated with the corresponding forest inventory data. For each classified area (exploitation, forest growth) the changes for the assessed growing stock are analyzed separately. Finally the derived growing stock maps are validated with the corresponding FI data. It could be shown that the total amount of growing stock changes, divided into exploitation and forest growth, derived from the estimated growing stock maps from the entire study area, are similar to those derived from the statistical analyses of the in-situ forest inventory data. In Figure 5 a difference map of estimated growing stocks (2011 – 2004) overlaid with the detected exploitation areas is shown. The visual validation shows that the applied work flow for detecting harvested areas work well even on the level of single trees. Using GIS tools the total amount of harvested growing stock can be calculated for example for each exploitation polygon. For the estimation of the forest growth an averaging within homogenous areas (e. g. forest stands) is required to avoid errors originating from different tree crown representations (i. e. due to varying ALS point density, ALS sensors, ALS acquisition properties, image matching quality, wind effects, etc.) on a single tree level.

Forest road extraction

An optimal planning of forest harvesting and logging relies on an up-to-date forest roads network. Ideally this network allows automatic routing for optimizing the transportation routes. Additionally the combination of growing stock maps and a routable forest roads graph enables efficient planning and optimizing of cable crane positions. In contrast to public roads, which are of high interest for the society, forest roads are often not mapped or were mapped with insufficient information for routing. Therefore, the task of updating the forest roads network is fundamental for heading into the direction of an efficient forest management and wood supply chain. Within several research projects at the research group Photogrammetry, a semi-automatic method for extracting forest roads from ALS data was developed. ALS data can deliver terrain information below dense canopies which enables an extraction of forest roads even in dense forested areas. This is an advantage compared to methods which purely rely on orthophotos. The developed algorithm relies on a weighted graph, automatically extracted from ALS data using watershed methods and slope information of the terrain. Additionally information from orthophotos is used. Based on this graph the forest roads are extracted as follows: A human interpreter defines starting and ending points of road sections. Between these points the shortest, best voted path within the weighted graph is automatically found. Using this method the forest roads network is sequentially extracted by the interpreter in an efficient way.

The weighted graph methodolgy enabled fully automatically pre-processing of the input data and can be applied for different terrain conditions. To enable comfortable digitizing of forest roads in a functional Open Source GIS environment, a Quantum GIS Plugin was implemented. Based on the weighted graph and knowledge from a human interpreter a topologically correct forest road network can be extracted using this Plugin. The sequentially digitization process delivers user controlled results where errors can be corrected immediately during the process. This is a big advantage to fully automatically methods where only little user interaction is given. The semi automatically digitization process was found to be more efficient than a manually extraction as large road segments can be digitized easily. Additional attributes as for example road width, curve radii and gradient of segments can be derived for the extracted roads (see Figure 6). This information is important for routing purposes. Attributes can also be extracted from existing datasets originating from other sources as for example Open Street Maps or GIP [70] where only the street axis is available.

4. Conclusion

During the last decade the technological developments of airborne laserscanning and digital photogrammetry lead to efficient workflows for gathering 3D information. Especially for forestry applications the object heights, which are included in the 3D data, provide new information for the monitoring of quantitative forest parameters such as e. g. tree growth, growing stock or harvested biomass. Even though several success stories can be found in literature, there are still open issues to be solved until these data sources are included into operational forest management applications on large scale. On the one hand there are open questions about the data availability on

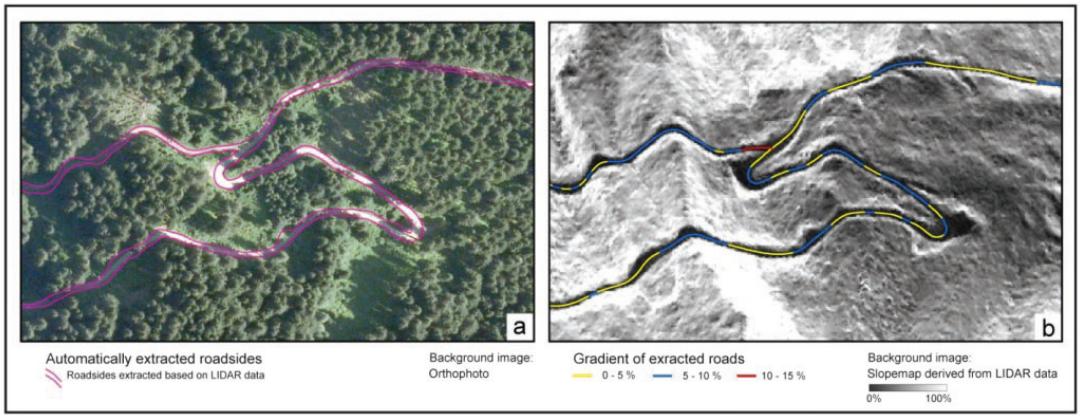

Fig. 6: Example for extracted forest roads. ***a)*** *forest road outlines overlaid over an orthophoto and* ***b)*** *gradient of extracted forest road network overlaid over a shaded DTM. The road segments are colour coded by gradient (adapted from [71].*

a regular base with reasonable costs. For operational applications of remote sensing data in forest community the availability of comparable data over several decades is of special importance. With respect to this demand country-wide data acquisition plans with a minimum of data quality standards are highly desirable. On the other hand the huge amount of data implies new challenges for available methods and software programs. For example, the requirement to the georeferencing accuracy of ALS data is much higher for change detection studies than for analyses using only one acquisition time and often the available data has to be re-processed for improving the positional accuracy. Furthermore, the combined analyses of 3D data originating from different acquisition methods (i. e. image matching, ALS) need the adaption of available methods to consider the properties of the different data sources (e. g. ALS data describe the entire vertical profile of forests whereas image matching provide mainly information about the top most canopy surface). At the research groups of Photogrammetry and Remote Sensing at GEO at the TU Wien, several research projects are ongoing in which these research questions are studied together with national and international partners from the remote sensing as well as the forest community.

Acknowledgement

This work is founded from the European Community's Seventh Framework Programme (FP7/2007–2013) under grant agreement No. 606971, the Advanced_SAR (Advanced Techniques for Forest Biomass and Biomass Change Mapping Using Novel Combination of Active Remote Sensing Sensors) project. The Basics of this work were done in the previous research projects NEWFOR financed by the European Territorial Cooperation Alpine Space, LASER-WOOD (822030) funded by the Klima- und Energiefonds in the framework of the program "NEUE ENERGIEN 2020", ChangeHabitats2 (Marie Curie – FP7-PEOPLE-2009-IAPP - Grant Agreement Number 251234), TransEcoNet implemented through the CENTRAL EUROPE Program co-financed by the ERDF and the project "Ableitung des Forststraßennetzes in Österreich aus Airborne Laserscanning Daten" financed by the Austrian Federal Ministry of Agriculture, Forestry, Environment and Water Management. Finally I would like to thank my current and former colleagues at the research groups Photogrammetry and Remote Sensing at TU Wien for their contribution to the mentioned research projects.

References

[1] *Zwally, H.J.; Schutz, B.; Abdalati, W.; Abshire, J.; Bentley, C.; Brenner, A.; Bufton, J.; Dezio, J.; Hancock, D.; Harding, D., et al.*: ICESat's laser measurements of polar ice, atmosphere, ocean, and land. Journal of Geodynamics 2002, 34, 405-445.

[2] *Wagner, W.; Ullrich, A.; Melzer, T.; Briese, C.; Kraus, K.*: In From single-pulse to full-waveform airborne laser scanners: Potential and practical challenges, International Society for Photogrammetry and Remote Sensing XXth Congress, Vol XXXV, Part B/3, 12–23 July 2004, Commission 3, Istanbul, Turkey, 2004; Altan, O., Ed. Istanbul, Turkey, p 6.

[3] *Rieger, P.; Ullrich, A.*: Resolving range ambiguities in high-repetition rate airborne light detection and ranging applications. Journal of Applied Remote Sensing 2012, 6.

[4] *Briese, C.; Pfennigbauer, M.; Lehner, H.; Ullrich, A.; Wagner, W.; Pfeifer, N.*: Radiometric Calibration Of Multi-Wavelength Airborne Laser Scanning Data. ISPRS Ann. Photogramm. Remote Sens. Spatial Inf. Sci. 2012, 1-7, 335-340.

[5] *Kilian, J.; Haala, N.; Englich, M.*: Capture and evaluation of airborne laser scanner data. International Archives of Photogrammetry and Remote Sensing 1996, XXXI, B3, 383-388.

[6] *Baltsavias, E.P.*: Airborne laser scanning: existing systems and firms and other resources. ISPRS Journal of Photogrammetry & Remote Sensing 1999, 54, 165-198.

[7] *Baltsavias, E.P.*: Airborne laser scanning: basic relations and formulas. ISPRS Journal of Photogrammetry & Remote Sensing 1999, 54, 199-214.

[8] *Wehr, A.; Lohr, U.*: Airborne laser scanning - an introduction and overview. ISPRS Journal of Photogrammetry & Remote Sensing 1999, 54, 68-82.

[9] *Kager, H.*: Discrepancies between overlapping laser scanner strips - simultaneous fitting of aerial laser scanner strips. International Archives of Photogrammetry, Remote Sensing and Spatial Information Sciences 2004, XXXV, 555-560.

[10] *Burman, H.*: Laser strip adjustment for data calibration and verification. International Archives of Photogrammetry and Remote Sensing 2002, XXXIV, 3, 67-72.

[11] *Filin, S.*: Recovery of systematic biases in laser altimetry data using natural surfaces. Photogrammetric Engineering & Remote Sensing 2006, 69, 1235-1242.

[12] *Haala, N.; Wolf, K.; Hastedt, H.; Ressl, C.; Baltrusch, S.; Stößel, W.*: Digital Photogrammetric Camera Evaluation - Generation of Digital Elevation Models PFG Photogrammetrie, Fernerkundung, Geoinformation 2010, 2, 99-115.

[13] *Förstner, W.*: In On the Geometric Precision of Digital Correlation, Proceedings of the ISPRS Symposium Mathematical Models, Accuracy Aspects and Quality Control, Finland, 1982; Finland, pp 176-189.

[14] *Förstner, W.; Gülch, E.*: In A Fast Operator for Detection and Precise Location of Distinct Point, Corners and Centers of Circular Features, Proceedings of the ISPRS Conference on Fast Processing of Photogrammetric Data, Interlaken, 1987; Interlaken, pp 281-305.

[15] *Hirschmüller, H.*: Stereo Processing by Semiglobal Matching and Mutual Information. IEEE Transactionon on Pattern Analyses and machine Intelligence 2008, 30, 328-341.

[16] *Pierrot-Deseilligny, M.; Paparoditis, N.*: A multiresolution and optimization-based imagematching approach: An application to surface reconstruction from SPOT5-HRS stereoimagery. In IAPRS, Vol. XXXVI-1/W41 in ISPRS Workshop On Topographic Mapping From Space (With Special Emphasis on Small Satellites), Ankara, Turkey, 2006.

[17] *Gruen, A.*: Development and status of image matching in photogrammetry. The Photogrammetric Record 2012, 27, 36-57.

[18] *Zabih, R.; Woodfill, J.*: In Non-parametric local transforms for computing visual correspondence, Proceedings of 3rd European Conf. Computer Vision, Stockholm, 1994; Stockholm, pp 151-158.

[19] *Wenzel, K.; Rothermel, M.; Haala, N.; Fritsch, D.*: SURE – The ifp Software for Dense Image Matching In Photogrammetric Week '13, Fritsch, D., Ed. Wichmann, Berlin/Offenbach: 2013; pp 59-70.

[20] *Rothermel, M.; Haala, N.*: Potential of dense matching for the generation of high quality digital elevation models. International Archives of the Photogrammetry, Remote Sensing and Spatial Information Sciences 2011, XXXVIII-4/W19, 271-276.

[21] *Baltsavias, E.; Gruen, A.; Eisenbeiss, H.; Zhang, L.; Waser, L.T.*: High-quality image matching and automated generation of 3D tree models. International Journal of Remote Sensing 2008, 29, 1243-1259.

[22] *White, J.C.; Wulder, M.A.; Vastaranta, M.; Coops, N.C.; Pitt, D.; Woods, M.*: The Utility of Image-Based Point Clouds for Forest Inventory: A Comparison with Airborne Laser Scanning. Forests 2013, 4, 518-536.

[23] *Pfeifer, N.*: Oberflächenmodelle aus Laserdaten. Österreichische Zeitschrift für Vermessung & Geoinformation (VGI) 2003, Heft 4/2003, 243-252.

[24] *Kraus, K.; Pfeifer, N.*: Determination of terrain models in wooded areas with airborne laser scanner data. ISPRS Journal of Photogrammetry and Remote Sensing 1998, 53, 193-203.

[25] *Scop++. Programpackage for Digital Terrain Models, http*://photo.geo.tuwien.ac.at/software/scop/; http://www.trimble.com/Imaging/Inpho.aspx?tab=Geo-Modeling_Module. Last accessed June 2015.

[26] *Sithole, G.; Vosselman, G.*: Experimental comparison of filter algorithms for bare-Earth extraction from airborne laser scanning point clouds. ISPRS Journal of Photogrammetry & Remote Sensing 2004, 59, 85-101.

[27] *Hollaus, M.; Mandlburger, G.; Pfeifer, N.; Mücke, W.*: In Land cover dependent derivation of digital surface models from airborne laser scanning data, ISPRS Commission III Symposium PCV2010, Saint-Mandré, France, 2010; Saint-Mandré, France, pp 6-6.

[28] *Höfle, B.; Mücke, W.; Dutter, M.; Rutzinger, M.; Dorninger, P.*: Detection of building regions using airborne LiDAR – A new combination of raster and point cloud based GIS methods. GI_Forum 2009 - International Conference on Applied Geoinformatics, Salzburg 2009, accepted.

[29] *Pfeifer, N.; Mandlburger, G.; Otepka, J.; Karel, W.*: OPALS - A framework for Airborne Laser Scanning data analysis. Computers, Environment and Urban Systems 2014, 45, 125-136.

[30] *Eysn, L.; Hollaus, M.; Schadauer, K.; Pfeifer, N.*: Forest Delineation Based on Airborne LIDAR Data. Remote Sensing 2012, 4, 762-783.

[31] *Zhu, Z.; Waller, E.*: Global forest cover mapping for the United Nations Food and Agriculture Organization Forest Resources Assessment 2000 program. Forest Sci 2003, 49, 369–380.

[32] *FAO/FRA. Definitions of Forest and Forest Change. In Forest Resources Assessment Programme. In FAO*: Rome, Italy, 2000; p 15.

[33] *Jennings, S.B.; Brown, N.D.; Sheil, D.*: Assessing forest canopies and understorey illumination: canopy closure, canopy cover and other measures. Forestry 1999, 72, 59-59.

[34] *Wang, Z.; Boesch, R.; Ginzler, C.*: Forest delineation of aerial images with "Gabor" wavelets. Int. J. Remote Sens 2011, 33, 2196-2213.

[35] *Wang, Z.Y.; Boesch, R.; Ginzler, C.*: Integration of High Resolution Aerial Images And Airborne Lidar Data for Forest Delineation. In ISPRS XXI Congress, Beijing, China, 2008; pp 1203-1208.

[36] *Mustonen, J.; Packalén, P.; Kangas, A.S.*: Automatic segmentation of forest stands using a canopy height model and aerial photography. Scandinavian Journal of Forest Research 2008, 23, 534-545.

[37] *Straub, C.; Weinacker, H.; Koch, B.*: A Fully Automated Procedure for Delineation and Classification of Forest and Non-Forest Vegetation Based on Full Waveform Laser Scanner Data. International Archives of the Photogrammetry, Remote Sensing and Spatial Information Sciences 2008, 37, 1013-1019.

[38] *Eysn, L.; Hollaus, M.; Schadauer, K.; Roncat, A.*: In crown coverage calculation based on ALS data, 11th International Conference on LiDAR Applications for Assessing Forest Ecosystems (Silvilaser 2011), Hobart, Australia, Oct. 16-20, 2011; Hobart, Australia, p 10.

[39] *Eysn, L.; Hollaus, M.; Berger, F.*: In NEWFOR - Enhancing the wood supply chain within the alpine space – An insight in forest delineation, stratification of growing stock models and forest roads extraction based on LIDAR data, ForestSat 2014, At Riva del Garda, Italy, 2014; At Riva del Garda, Italy, p 6 pages.

[40] *Weiss, P.; Schieler, K.; Schadauer, K.; Radunsky, K.; Englisch, M.*: Die Kohlenstoffbilanz des Österreichischen Waldes und Betrachtungen zum Kyoto-Protokoll; Forstliche Bundesversuchsanstalt; Umweltbundesamt: Wien, 2000; p 93.

[41] *Cháidez, J.*: Allometric equations and expansion factors for tropical try forest trees of eastern Sinaloa, Mexico. Trop. Subtrop. Agroecosyst 2009, 10, 45-52.

[42] *Hyyppä, J.; Inkinen, M.*: Detecting and estimating attributes for single trees using laser scanner. The Photogrammetric Journal of Finland 1999, 16, 27-42.

[43] *Popescu, S.C.; Wynne, R.H.; Nelson, R.F.*: Measuring individual tree crown diameter with lidar and assessing its influence on estimating forest volume and biomass. Canadian Journal of Remote Sensing 2003, 29, 564-577.

[44] *Næsset, E.*: Practical Large-scale Forest Stand Inventory Using a Small-footprint Airborne Scanning Laser. Scandinavian Journal of Forest Research 2004, 19, 164-179.

[45] *Maltamo, M.; Packalén, P.; Peuhkurinen, J.; Suvanto, A.; Pesonen, A.; Hyyppä, J.*: In Experiences and possibilities of ALS based forest inventory in Finland, ISPRS Workshop Laser Scanning 2007, Espoo, Finland, 09-12-2007 - 09-14-2007, 2007; Espoo, Finland, pp 270-279.

[46] *Hollaus, M.; Dorigo, W.; Wagner, W.; Schadauer, K.; Höfle, B.; Maier, B.*: Operational wide-area stem volume estimation based on airborne laser scanning and national forest inventory data. International Journal of Remote Sensing 2009, Accepted on march 15, 2009.

[47] *Schardt, M.; Ziegler, M.; Wimmer, A.; Wack, R.; Hyyppä, J.*: Assessment of Forest Parameters by Means of Laser Scanning. International Archives of Photogrammetry, Remote Sensing and Spatial Information Sciences 2002, XXXIV (Part 3/A), 302-309.

[48] *Jochem, A.; Hollaus, M.; Rutzinger, M.; Höfle, B.*: Estimation of aboveground Biomass in Alpine Forests: A Semi-Empirical Approach Considering Canopy Transparency Derived from Airborne LiDAR Data. Sensors 2011, 11, 278-295.

[49] *Næsset, E.*: Area-Based Inventory in Norway – From Innovation to an Operational Reality. In Forestry Applications of Airborne Laser Scanning: concepts and Case Studies, Maltamo, M.; Næsset, E.; Vauhkonen, J., Eds. Springer Netherlands: 2014; Vol. 27, pp 215-240.

[50] *Hollaus, M.; Wagner, W.; Schadauer, K.; Maier, B.; Gabler, K.*: Growing stock estimation for alpine forests in Austria: a robust LiDAR-based approach. Canadian Journal of Forest Research 2009, 39, 1387-1400.

[51] *Waser, L.T.*: Airborne remote sensing data for semi-automated extraction of tree area and classification of tree species. Zürich, E., Ed. 2012; p 153 S.

[52] *Hollaus, M.; Mücke, W.; Höfle, B.; Dorigo, W.; Pfeifer, N.; Wagner, W.; Bauerhansl, C.; Regner, B.*: Tree species classification based on full-waveform airborne laser scanning data. SilviLaser 2009, October 14-16, 2009 – College Station, Texas, USA 2009.

[53] *Hollaus, M.; Eysn, L.; Karel, W.; Pfeifer, N.*: In Growing stock change estimation using Airborne Laser Scanning data, 13th International Conference on LiDAR Applications for Assessing Forest Ecosystems (SilviLaser 2013), Beijing, China, 2013-10-09 - 2013-10-11, 2013; Beijing, China, p 8.

[54] *Straub, C.; Stepper, C.; Seitz, R.; Waser, L.T.*: Potential of UltraCamX stereo images for estimating timber volume and basal area at the plot level in mixed European forests. Canadian Journal of Forest Research 2013, 43, 731-741.

[55] *Bohlin, J.; Wallerman, J.; Fransson, J.*: Forest variable estimation using photogrammetric matching of digital aerial images in combination with a high-resolution DEMx. Scandinavian Journal of Forest Research 2012, 27, 692-699.

[56] *Lefsky, M.A.; Turner, D.P.; Guzy, M.; Cohen, W.B.*: Combining lidar estimates of aboveground biomass and Landsat estimates of stand age for spatially extensive validation of modeled forest productivity. Remote Sensing of Environment 2005, 95, 549-558.

[57] *Hollaus, M.; Mücke, W.; Eysn, L.*: Forest structure and stem volume assessment based on airborne laser scanning. Ambiência 2012, 8, 471-482.

[58] *Tews, J.; Brose, U.; Grimm, V.; Tielbörger, K.; Wichmann, M.C.; Schwager, M.; Jeltsch, F.*: Animal species diversity driven by habitat heterogeneity/diversity: the importance of keystone structures. Journal of Biogeography 2004, 31 79-92.

[59] *Coops, N.C.; Hilker, T.; Wulder, M.A.; St-Onge, B.; Newnham, G.; Siggins, A.; Trofymow, J.A.T.*: Estimating canopy structure of Douglas-fir forest stands from discrete-return LiDAR. Trees 2007, 21, 295-310.

[60] *Leiterer, R.; Morsdorf, F.; Schaepman, M.; Mücke, W.; Pfeifer, N.; Hollaus, M.*: In Robust characterization of forest canopy structure types using full-waveform airborne laser scanning, SilviLaser 2012, Vancouver, British Columbia, Canada, 2012-09-16 - 2012-09-19, 2011; Vancouver, British Columbia, Canada, p 8.

[61] *Hall, S.A.; Burke, I.C.; Box, D.O.; Kaufmann, M.R.; Stoker, J.M.*: Estimating stand structure using discrete-return lidar: an example from low density, fire prone ponderosa pine forests. Forest Ecology and Management 2005, 208, 189-209.

[62] *Zimble, D.A.; Evans, D.L.; Carlson, G.C.; Parker, R.C.; Grado, S.C.; Gerard, P.D.*: Characterizing vertical forest structure using small-footprint airborne LIDAR. Remote Sensing of Environment 2003, 87, 171-182.

[63] *Lim, K.; Treitz, P.; Wulder, M.; St-Onge, B.; Flood, M.*: LIDAR remote sensing of forest structure. Progress in Physical Geography 2003, 27, 88-106.

[64] *Wagner, W.; Ullrich, A.; Ducic, V.; Melzer, T.; Studnicka, N.*: Gaussian decomposition and calibration of a novel small-footprint full-waveform digitising airborne laser scanner. ISPRS Journal of Photogrammetry & Remote Sensing 2006, 60, 100-112.

[65] *Reitberger, J.; Schnörr, C.; Krzystek, P.; Stilla, U.*: 3D segmentation of single trees exploiting full waveform LIDAR data. ISPRS Journal of Photogrammetry and Remote Sensing 2009, 64, 561-574.

[66] *Hollaus, M.; Mücke, W.; Roncat, A.; Pfeifer, N.; Briese, C.*: Full-Wavform Airborne Laser Scanning Systems and Their Possibilities in Forest Applications. In Forestry Applications of Airborne Laser Scanning: concepts and Case Studies, Maltamo, M.; Næsset, E.; Vauhkonen, J., Eds. Springer Netherlands: 2014; Vol. 27, pp 43-61.

[67] *Mücke, W.*: Full-Waveform Airborne Laser Scanning for Landscape Ecological Mapping: Methods and Applications. Vienna University of Technology, Vienna, 2014.

[68] *Vetter, M.; Höfle, B.; Hollaus, M.; Gschöpf, C.; Mandlburger, G.; Pfeifer, N.; Wagner, W.*: In Vertical Vegetation Structure Analysis And Hydraulic Roughness Determination Using Dense Als Point Cloud Data - A Voxel Based Approach, ISPRS Workshop Laser Scanning 2011, Calgary, Canada, 2011-08-29 - 2011-08-31, 2011; ISPRS: Calgary, Canada, p 6.

[69] *Maier, B.*: Characterising Mountain Forest structure using Airborne Laser Scanning. Master thesis, Salzburg University, Salzburg, 2007.

[70] *GIP. Graphenintegrations-Plattform. http*://www.gip.gv.at/. Last accessed June 2015.

[71] *Hollaus, M.; Eysn, L.; Grafl, A.; Schadauer, K.; C., B.*: Digitale Forststraßen bei der Waldinventur. Forstzeitung 2014, 125, 10-11.

Contact

Dipl.-Ing. Dr. Markus Hollaus, TU Wien, Department of Geodesy and Geoinformation (E120-7), Gusshausstraße 27-29, 1040 Vienna, Austria.
E-Mail: Markus.Hollaus@GEO.tuwien.ac.at


Laser Ranging to Space Debris from Graz Laser Station

Georg Kirchner and Franz Koidl, Graz

Abstract

The Satellite Laser Ranging (SLR) station Graz is measuring distances to satellites – equipped with retro-reflectors – with an accuracy of a few millimetres, since several years. In addition, in 2012 we started to measure also distances to space debris – e.g. old rocket bodies, which are NOT equipped with retro-reflectors ('non-cooperative targets'). In several experimental sessions, we have tracked some hundred passes of about 60 objects of different sizes, in distances between 500 km and up to 3000 km. In 2013, Graz started with 'multi-static' laser ranging: While Graz ranged to the debris target, other European SLR stations – synchronized to the Graz laser shots – detected the diffusely reflected Graz photons, thus adding one-way measurements (from target to the stations).

Keywords: Space Debris, Laser Ranging

Kurzfassung

Die 'Satellite Laser Ranging (SLR)' Station Graz misst die Entfernung zu Satelliten, die mit Retro-Reflektoren ausgestattet sind, mit einer Genauigkeit von 2 bis 3 mm. Zusätzlich begannen wir 2012 auch die Entfernungen zu Weltraumschrott zu messen – z.B. zu alten Raketenstufen, die NICHT mit Retro-Reflektoren ausgestattet sind. In mehreren Experimental-Sessions von jeweils etwa 2 Stunden wurden über 200 Durchgänge von insgesamt mehr als 60 Objekten verschiedener Größen in Entfernungen zwischen 500 km und mehr als 3000 km gemessen.

Schlüsselwörter: Weltraumschrott, Laser Ranging

1. Introduction

The Satellite Laser Ranging (SLR) station Graz is located at the Observatory Lustbühel, on a hill close to and about 150 m above the city of Graz (Figure 1). It uses a 2 kHz laser (400 µJ per shot @ 532 nm, 10 ps pulse duration) to measure distances to satellites, which are equipped with retro-reflectors; the accuracy is a few millimetres. The 2 kHz repetition rate allows to apply statistics to form very accurate Normal Points, which can reach an ultimate resolution of about 0.2 mm. Calculating a best-fit orbit using SLR data of about 40 stations distributed around the world, shows the excellent accuracy of the Graz SLR station (Figure 2).

Fig. 1: Observatory Graz-Lustbühel: SLR Dome, SLR telescope

2. The Space Debris Problem

2.1 General space debris information

Space debris is created by rocket bodies, upper stage engines, decommissioned satellites, and fragmentation due to break-ups, collisions, explosions of non-empty fuel tanks etc. The number of space debris objects is increasing rapidly, and within a few years it could reach a run-away point in the most populated LEO orbits between 800 km and 1200 km, where the number of debris items constantly increases due to progressively unavoidable collisions. This scenario is called the *Kessler Syndrome* [1] and is predicted with high probability even for the very unlikely case that all future launches are stopped.

Pieces of space debris – travelling at high speeds of about 8 km/s in crowded orbits - pose increasing hazards to manned and unmanned space flights and space operations. There have been already several collisions in space, some with minor consequences (Jason-1, March 2002) [2], some catastrophic (Iridium33 collision with Cosmos 2251 in 2009), and some even intentionally generated: China destroyed 2007 its own aging Fengyun-1C weather satellite during an anti-satellite rocket test, increasing the total number of radar traceable debris objects by 22 %.

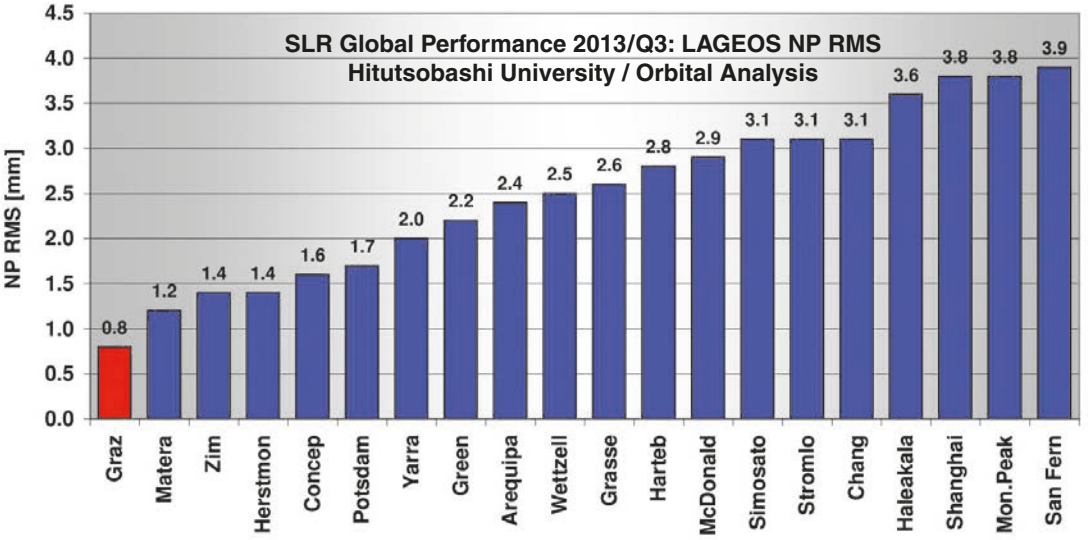

Fig. 2: SLR Graz delivers very accurate Normal Points of satellite LAGEOS

The estimated number of space debris objects down to a size of about 1 cm is already in the order of about 600,000. While particles smaller than about 1 cm can be mitigated by proper shielding of spacecrafts, collisions with larger objects are most likely catastrophic due to the high kinetic energy involved at relative propagation velocities above 8 km/s. To avoid collisions, spacecraft manoeuvres are required, which are costly in terms of available propellant. Threats from space debris have caused already 16 collision avoidance manoeuvres of the ISS since October 1999 [2].

2.2 Determination of space debris orbits

Space debris orbits are determined mainly by tracking with big radar systems, like the U.S. Space Surveillance Network, and the TIRA (Tracking and Imaging RAdar) near Bonn (Fraunhofer Institute), or by passive optical tracking with telescopes [3], [4]. The radar systems usually operate in 'staring mode': The radar dish pointing remains fixed and all objects passing within the radar beam are recorded.

Passive optical methods usually work in a similar way: Telescopes observe the sky and record accurate tracks of sunlit objects with cameras; this method has additional limitations by needing clear weather and darkness at the observing site, and the objects to be sunlit.

While these well established methods are effective, and have taken the main burden of space debris orbit determination, their nominal accuracy is relatively low, and the resulting orbit predictions may have offsets of up to a kilometre or more [10]. The accuracy can be increased only with repeated measurements focussed on selected targets; this is costly and time consuming. Inaccurate orbits are a problem for proper scheduling of collision avoidance manoeuvres - any unnecessary manoeuvre is a waste of limited propellant – and also for ambitious plans aiming for the removal of space debris from orbit by laser ablation [5], [6].

3. Laser Ranging to space debris targets

3.1 Laser Ranging to space debris from a single Satellite Laser Ranging station: Graz

An evolving method to improve space debris orbit predictions uses high energy laser pulses, fired to space debris objects, detecting the diffusely reflected photons and measuring the time-of-flight to determine the distance. The results reported up to now used kW lasers [7], or more recently a 2 J/20 Hz laser [8], or a 2 J/10 Hz laser at the lunar laser ranging station in Grasse / France [9]. At the satellite laser ranging (SLR) station Graz, the first laser ranging measurements to debris objects started in 2012 [10], using a diode-pumped laser (on loan from DLR Stuttgart) with 1 kHz repetition rate, with a relatively low energy of 25 mJ per pulse, and 10 ns pulse width.

This first laser was replaced in 2013 by a flash lamp pumped laser (also on loan from DLR

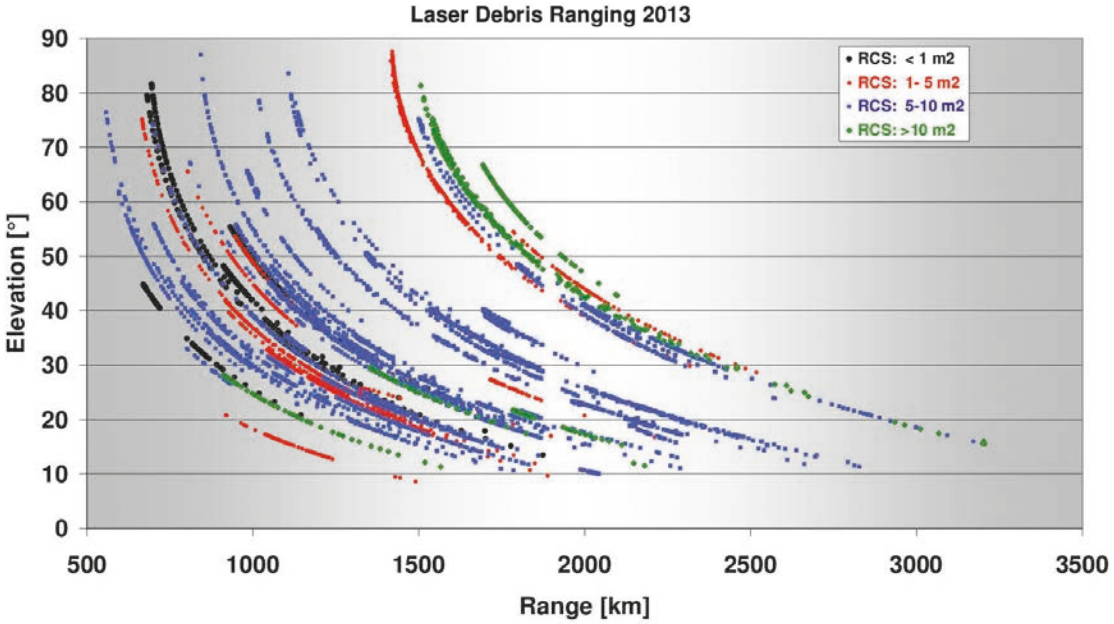

Fig. 3: SLR Graz: Laser Ranging to Space Debris Objects in 2013: > 200 Passes, about 60 different objects, 13 sessions; up to 3000 km distance

Stuttgart) with 99.9 Hz maximum repetition rate, 200 mJ per pulse and 3 ns pulse width. Both lasers operated at 532 nm, the most common wavelength used for satellite laser ranging, and were successfully used to measure distances of up to about 3000 km to larger targets with several m^2 Radar Cross Section (RCS), and to smaller targets (down to 0.3 m^2 RCS) at shorter distances (Figure 3)

3.2 Multi-Static Laser Ranging to space debris

We extended this basic concept by including multiple SLR stations into the measurement process, in order to achieve Multi-Static Laser Ranging to space debris objects. One station (called the 'active' station ⇒ Graz) fires laser pulses to the object and detects the diffusely reflected photons measuring the time-of-flight. Additional stations ('passive' stations) track the same target with their telescopes without firing their own laser, and detect diffusely reflected photons of the active station (Figures 4 and 5).

The 'passive' stations have to be synchronized to the 'active' station Graz; that means they have to know the Graz firing epochs to significantly better than 1 μs. This was achieved by predefining all Graz firing epochs in advance, with an accuracy of < 100 ns; to make this as simple as possible, we selected an accurate 80 Hz laser repetition rate, which is repeated within each one-second period; the offset of the first firing epoch from the 1 pps was published to the passive stations in advance for each session.

These 'passive' stations measure pseudo-ranges, because of the unknown clock offsets between the active and each passive station. These measurements are only quasi-simultaneous since the small percentage of laser shots that generate an echo at the Graz SLR will mostly correspond to different laser fire times as those

Fig. 4: Graz fired laser pulses to debris targets passing over Middle Europe; the photons - diffusely reflected from the debris targets - were detected at 4 SLR stations: Graz; Zimmerwald (600 km); Wettzell (400 km); Herstmonceux (1200 km); Graphics: Peter Ruzek/ AIUB

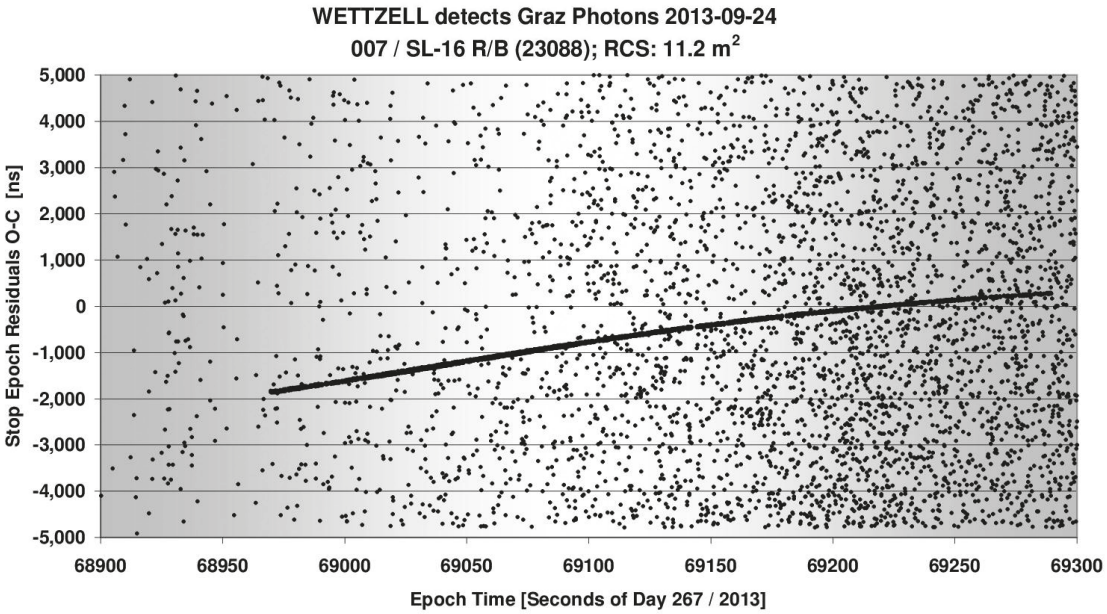

Fig. 5: Graz photons, diffusely reflected from an old rocket body (NORAD 23088; 11 m² RCS (Radar Cross Section), in an 850 km orbit) and detected at the SLR station Wettzell; shown are the residuals, ZERO is the predicted time-of-flight (Graz – Target – Wettzell)

laser shots generating echoes at each individual passive station.

The main goal of the here described technique is to generate a significantly more precise orbit prediction for a selected target which is accurate to 10–20 arc seconds for the next 24 or 48 hours and to do so in a significantly shorter time of approximately 3 hours (2 revolutions of the target around the Earth). First results indicate a possible 10 times improvement [11] when using multi-static laser ranging data.

4. Conclusion, outlook, future plans

Synchronizing the SLR stations at Zimmerwald, Wettzell and Herstmonceux to the Graz laser firing times, these three 'passive' stations could detect the laser pulses from Graz, diffusely reflected from space debris targets. The Graz laser fired at a wavelength of 532 nm pulses with 80 Hz, 200 mJ per pulse and 3 ns pulse width.

Using one uplink and several quasi-simultaneous downlink trajectories, multi-static laser ranging to space debris targets has demonstrated the prerequisites for a more accurate orbit determination (10–20 arc seconds for the next 24 or 48 hours) in significantly shorter time (24 hours) needing fewer passes (e. g. 2).

The 4 SLR stations – including Graz – involved in the experiment are located in 4 different weather zones; this reduces heavily the probability for acceptable laser ranging conditions at all sites. As a consequence, only during 1 out of 9 sessions we obtained triple ranges (Graz, Zimmerwald and Wettzell). During the other 8 sessions, we had acceptable laser ranging conditions only in Graz and one of the 'passive' stations: Weather simply was the main limitation for successful multi-static sessions in the optical regime. However, there are several possible ways to improve this:

- More participating *'passive'* (receive-only) stations: Potsdam, Borowiec, Riga, Grasse and Matera have already expressed their interest
- Increase the number of *'active'* stations (transmitting strong laser pulses): This is more limited because more expansive equipment (high energy laser) is necessary. This method could however resolve the time scale differences (or clock offset) issue: Two stations both firing and receiving not only their own echoes, but also echoes from the other transmitting station, corresponds to the conditions of asynchronous transponder operations [12]
- Adding a few receive-only stations within e. g. 200 km of a transmitting station:
  - It is more likely to have consistent weather conditions within shorter distances;

- These stations could be much cheaper than a complete SLR station (no laser, no Coudé optical feeding path)
- Remote-controlled / automatic; no costs for operators; no laser / aircraft problems etc.

Even with the present configuration, the existing pool of SLR stations in Europe, linked within the EUROLAS sub-network of the ILRS, already offers a unique opportunity to perform such multi-static laser ranging to space debris.

Future plans include measurements with at least 3 or 4 stations simultaneously, which assumes that more European SLR stations will become available for this purpose. These measurements will establish how fast and how well the initial orbit prediction accuracy can be improved using a minimum number of acquisitions.

References

[1] Kessler, D.J., Cour-Palais, B.G. Collision Frequency of Artificial Satellites: The Creation of a Debris Belt. Journal of Geophysical Research, Vol. 38, No. A6, pp. 2647-2646, 1978.

[2] *NASA*: Orbital Debris Quarterly News, Volume 15, Issue 3, July 2011. http://orbitaldebris.jsc.nasa.gov/newsletter/pdfs/ODQNv15i3.pdf.

[3] Shell, James R. Optimizing orbital debris monitoring with optical telescopes. US Air Force, Space Innovation and Development Center. 2010. http://www.dtic.mil/cgi-bin/GetTRDoc?AD=ADA531931

[4] Milani, A., Farnocchia, D., Dimare, L., Rossi, A., Bernardi, F. Innovative observing strategy and orbit determination for Low Earth Orbit space debris. Planetary and Space Science, 2011, doi: 10.1016/j.pss.2011.11.012.

[5] Schall, W. O., Orbital Debris Removal by Laser Radiation. Acta Astronautica Vol. 24, pp 343-351, 1991.

[6] Phipps, C.R., Baker, K.L., Libby, S. B., Liedahl, D. A., Olivier, S. S., Pleasance, L.D., Rubenchik, A., Trebes, J.E., George, E. V., Marcovici, B., Reilly, J.P., Valley, M.T. Removing Orbital Debris With Lasers; DOI: 10.1016/j.asr.2012.02.003.

[7] Greene, B., Gao, Y., Moore, C., Wang, Y., Boiko, A., Ritchie, J., Sang, J., Cotter, J., Laser Tracking of Space Debris. Proceedings of 13th Laser Ranging Workshop, Washington, 2003.

[8] Zhang, Z.P., Yang, F.M., Zhang, H. F., Wu, Z.B., Chen, J. P., Li, P., Meng, W. D. The use of laser ranging to measure space debris. Research in Astronomy and Astrophysics (RAA), Vol. 12, No 2, 2012; pg. 212-218.

[9] *Samain, E., Albanese, D., Esmiller, B., Laas-Bourez, M., Exertier, P., Haag, H., Paris, J., Mariey, H., Vial, S., Blanchet, G., Lorblanches, T., Torre, J. M.*: Demonstration of laser ranging observation on non-cooperative satellites with the MéO telescope, 39th COSPAR Scientific Assembly, 2012, India, Abstract E1.13-15-12, p. 1663.

[10] *Kirchner, G.; Koidl F., Friederich, F., Buske, I., Völker, U., Riede, W.*: Laser Measurements to Space Debris from Graz SLR Station. Advances in Space Research, Volume 51, Issue 1, 1. January 2013, pg 21.-24; JASR 11082; DOI: 10.1016/j.asr.2012.08.009; http://dx.doi.org/10.1016/j.asr.2012.08.009.

[11] *Wirnsberger, H., Baur, O., Kirchner, G.*: Space debris orbit prediction errors using bi-static laser observations. Case study: ENVISAT. Advances in Space Research; accepted / in press; doi:10.1016/j.asr.2015.02.018.

[12] *Degnan, J. J.*: Asynchronous laser transponders for precise interplanetary ranging and time transfer, Journal of Geodynamics, vol. 34, pp. 551–594, Aug. 2002.

Contacts

Dr. Georg Kirchner, Observatory Lustbuehel, Lustbuehelstrasse 46, A-8042 Graz, Austria.
E-Mail: Georg.Kirchner@oeaw.ac.at

Ing. Franz Koidl, Observatory Lustbuehel, Lustbuehelstrasse 46, A-8042 Graz, Austria.
E-Mail: Franz.Koidl@oeaw.ac.at

Development of the lunar gravity field model GrazLGM300a




Sandro Krauss, Beate Klinger, Oliver Baur and Torsten Mayer-Gürr, Graz

Abstract

In this contribution we present the latest activities (methods and results) at the Space Research Institute of the Austrian Academy of Sciences for the determination of the gravity field of the Moon, starting from the GrazLGM200a model, which has been published in early 2014. Our research is based on high-precision inter-satellite Ka-band ranging (KBR) observations collected by the Gravity Recovery And Interior Laboratory (GRAIL) mission during the primary mission phase (March 1 to May 29, 2012). We exploit the ranging measurements by an integral equation approach using short orbital arcs. The basic idea of the technique is to reformulate Newton's equation of motion as a boundary value problem. This method has already been successfully applied for the recovery of the Earth's gravity field from data provided by the Gravity Recovery And Climate Experiment (GRACE). For the development of our new Graz Lunar Gravity Model, GrazLGM300a, we refined modeling and parameterization. We validate our results with the GL660B solution - a recent GRAIL model computed at NASA-JPL, which is also based on observations from the primary mission phase. We show that the actual solution GrazLGM300a represents a distinctive improvement compared to the predecessor model and is close to the models developed at NASA, apart from the spectral resolution.

Keywords: Satellite Geodesy, Gravity, Moon, GRAIL

Kurzfassung

Ausgehend von der Schwerefeldlösung GrazLGM200a, die Anfang des Jahres 2014 publiziert wurde, werden in diesem Beitrag die aktuellen Forschungsergebnisse hinsichtlich der Schwerefeldbestimmung des Mondes am Institut für Weltraumforschung der Österreichischen Akademie der Wissenschaften präsentiert. Die Untersuchungen basieren auf hoch präzisen Ka-Band Distanzmessungen der Gravity Recovery And Interior Laboratory (GRAIL) Mission während der ersten Messphase (1. März bis 29. Mai, 2012). Die Messungen werden anhand eines Integralgleichungsansatzes unter Verwendung kurzer Bahnbögen analysiert. Die grundlegende Idee dahinter ist eine Umformulierung der Newton'schen Bewegungsgleichung als Randwertproblem. Diese Methode wurde bereits erfolgreich zur Schwerefeldbestimmung der Erde im Zuge der Gravity Recovery And Climate Experiment (GRACE) Mission verwendet. Für die Erstellung des aktuellen Mondschwerefeldes GrazLGM300a wurden Modellierung und Parametrisierung überarbeitet. Die Lösung wird mit dem NASA-JPL Modell GL660B, welches ebenfalls auf Beobachtungen während der ersten Messphase beruht, verglichen. Die aktuelle Lösung GrazLGM300a stellt eine deutliche Verbesserung zum Ausgangsmodell dar und entspricht, bis auf die spektrale Auflösung, annähernd den NASA Modellen.

Schlüsselwörter: Satellitengeodäsie, Schwerefeld, Mond, GRAIL

1. Introduction

Since the beginning of the space age in the late 1950's, the satellite-based exploration of the Moon is an important subject in scientific research. As a result, nearly 100 lunar missions with a wide range of science objectives were launched (more or less successfully) between 1959 and 1976.

Concerning lunar gravity, a milestone was the discovery of mass concentrations, so called mascons [16], based on data from the Lunar Orbiter V mission (1968). A major improvement in lunar gravity field mapping was achieved with the Lunar Prospector (LP) orbiter, launched in 1998 [1]. Due to the low average altitude of the mission tracking data to the LP spacecraft provided the first lunar gravity field from a low-altitude polar orbiter; based on these findings, research on the tidal deformation and thermal evolution of the Moon as well as the composition, state and size of the lunar core experienced considerable advance (e.g. [7], [8]).

Typically, the determination of the lunar gravity field is accomplished by analyzing orbit perturbations from Doppler shift observations (S-band and X-band) between a Moon-orbiting spacecraft and Earth-bound stations (e.g. the Deep Space Network, DSN or the Universal

Space Network, USN). However, due to the 1:1 spin-orbit resonance of the Earth-Moon system, tracking observations are restricted to the lunar nearside. As a consequence, the incorporation of constraints on the solution, for instance in terms of spectral-domain regularization is necessary [3]. The first satellite mission, which also provided observations over the farside of the Moon, was the Japanese Selenological and Engineering Explorer (SELENE) launched in 2007. The sophisticated mission design incorporated three satellites: a main orbiter in a circular orbit and two sub-satellites in elliptical orbits. In addition to classical (radiometric) tracking data, four-way Doppler tracking between the main orbiter and a relay satellite was employed as well as Very Long Baseline Interferometry (VLBI) measurements between the two sub-satellites and two ground stations on Earth resulting in a considerable improvement of the farside lunar gravity field [4], [17]. Nevertheless, observation accuracy still remained a limiting factor.

The lunar science mission which eclipses any previous attempts to recover detailed gravitational features of the Moon is the Gravity Recovery And Interior Laboratory (GRAIL) mission [20] launched by NASA on September 10, 2011. The mission concept is inherited from the Gravity Recovery And Climate Experiment (GRACE) project, a space gravimetry mission mapping the Earth's gravity field [19]. It consists of two identical spacecraft following each other in a low-altitude near-polar orbit. Table 1 gives an overview of the different mission phases and the orbit characteristics.

For our present gravity field investigations we focus on data solely from the primary mission.

Mission phases	
Launch	September 10, 2011
Primary mission	March 1 to May 29, 2012
Extended mission	August 30 to December 14, 2012
Decommissioning	December 17, 2012
Orbit characteristics	
Altitude	~55 km (±35 km)
Inclination	~89.9° (w.r.t. lunar equator)
Revolution period	113 min
Separation distance	82–218 km
Mean velocity	1.65 km/s

Tab. 1: GRAIL mission phases and orbit characteristics

The primary science instrument aboard each wGRAIL spacecraft is the Lunar Gravity Ranging System (LGRS; [6]), operating in the Ka-Band frequency (Ka-Band Ranging, KBR). Owing to these high-precision inter-satellite observations (about 0.03 µm/s) with global coverage, the twin-satellite mission allows to infer the lunar gravity field with unprecedented accuracy and spatial resolution [10], [12].

This contribution summarizes the processing strategies used for the development of GrazLGM300a – the latest lunar gravity field model computed in Graz. The work represents an extension to the achievements by [5], i.e. improvements over the predecessor model GrazLGM200a. We compare our results with gravity field models from the pre-GRAIL era as well as to recent GRAIL models computed at NASA-GSFC (Goddard Space Flight Center) and NASA-JPL (Jet Propulsion Laboratory).

2. Method and Parametrization

As an alternative to the GRAIL gravity field solutions from NASA, which are based on the solution of the equation of motion via variational equations (e.g., [15]), we propose a short-arc integral equation approach. The basic idea behind the integral equation approach is to reformulate Newton's equations of motion in the inertial space,

$$\acute{r}(t) = g(t) + a(t) = g(t) + a_b(t) + a_t(t) + a_n(t) + a_r(t), \quad (1)$$

as a boundary value problem [13]. This method has already been successfully applied to the recovery of the Earth's gravity field from data provided by the GRACE mission [14] and is implemented within the GROOPS (Gravity Recovery Object-Oriented Programming System) software package.

The total acceleration $\acute{r}(t)$ acting on the GRAIL spacecraft can be split into the Moon's gravitational attraction on the satellite $g(t)$ and additional perturbing forces $a(t)$, including third-body accelerations $a_b(t)$, accelerations due to solid Moon tides $a_t(t)$, non-gravitational accelerations $a_n(t)$ and relativistic effects $a_r(t)$. For the compilation of GrazLGM200a [5], solely gravitational perturbations – i.e. a_b and a_t were modelled. Our successor model GrazLGM300a also considers non-gravitational accelerations a_n in terms of solar radiation pressure and relativistic accelerations (Schwarzschild). The latter is in

the order of 1E-10 ms^{-2} and determined following the IERS Conventions 2010 [18].

In order to evaluate the influence of solar radiation pressure we use a 28-plate macro-model of the GRAIL spacecraft published by Fahnenstock [2]. Thus, it is possible to calculate the acceleration for each plate separately and sum up the individual contributions:

$$a_{srp} = \frac{\Phi r_p^2 \upsilon}{m_{s/c} c} \sum_{i=1}^{28} A_i \cos\varphi_i \Big[\hat{r}\left(1 - C_{s_i}\right) - \\ - \hat{n}_i \left(\frac{2}{3}\left(C_{d_i} + \alpha_i \varepsilon_i\right) + 2\cos\varphi_i C_{s_i} \right) \Big] \quad (2)$$

In the equation above, $\Phi = 1367\, Wm^{-2}$ denotes the solar flux constant at a distance of 1 astronomical unit, r_p represents the scaling factor to adjust Φ to the actual distance satellite-Sun. Lunar shadowing is solved purely geometrically from the angular separation and diameters of the Earth and Moon [15] with the associated shadowing function υ. The mass of the spacecraft is indicated by $m_{s/c}$, c is the velocity of light, A_i the individual plate area, $\hat{r}$ the direction from the Sun to the satellite, $\hat{n}_i$ the particular unit plate normal (outward directed), φ is the angle between $\hat{r}$ and $\hat{n}_i$, and C_{si}, C_{di}, α_i and ε_i describe the plate specific specular and diffuse reflectivity, the absorptivity and the emissivity, respectively. It has to be kept in mind that only plates which are illuminated by the Sun must contribute to the final solution.

The plot in Figure 1 illustrates the calculated acceleration over the primary mission phase (March 1 to May 29, 2012). Due to the fact that in April 2012 the solar beta angle was always close to 90 degrees, the spacecraft was permanently illuminated by the Sun and thus not shaded by the Moon at any time. At the beginning and the end of the primary mission phase the situation is different. During these times the spacecraft was shaded by the Moon once per revolution (Figure 1 bottom) – implying that the accelerations due to solar radiation pressure to become occasionally zero.

An overview of processing details and standards used for the compilation of the GrazLGM200a and GrazLGM300a models are given in Table 2.

For the computation of the GrazLGM300a model we used release 04 satellite ephemeris and KBR-observations. This has the advantage that time tagging inconsistencies, which were present in the previous releases, are already removed. Nevertheless, for our latest solution we co-estimated a time bias for the KBR observations (1E-04 to 1E-05 seconds) and included the estimation of empirical parameters (1 cycle per revolution and degree-2 polynomials). In case of thruster events the respective satellite observations were rejected. In order to avoid spectral aliasing, short-wavelength signals (from degree and order (d/o) 301 to 660) were reduced from the KBR data using the GL660B model [9]. A better approach would be to determine the gravity field beyond d/o 300; however, this requires enormous computational resources which are presently not available for the authors.

3. Results

In order to assess the quality of different lunar gravity field models we determined degree-error root mean square (DE-RMS) values according to

$$DE - RMS_n = \\ = \sqrt{\frac{1}{2n+1} \sum_{m=0}^{n} \left[\left(C_{nm}^{ref} - C_{nm}\right)^2 - \left(S_{nm}^{ref} - S_{nm}\right)^2 \right]} \quad (3)$$

where n and m are the degree and order, respectively, of the spherical harmonic expansion; C_{nm}^{ref}, S_{nm}^{ref} refer to the reference model GL660B developed by NASA-JPL. Figure 2 shows the performance of various gravity field solutions. The solid black curve indicates the GL660B signal; the orange curve is the difference to the GRGM660PRIM [11] model by NASA-GSFC, which can be considered as the empirical error

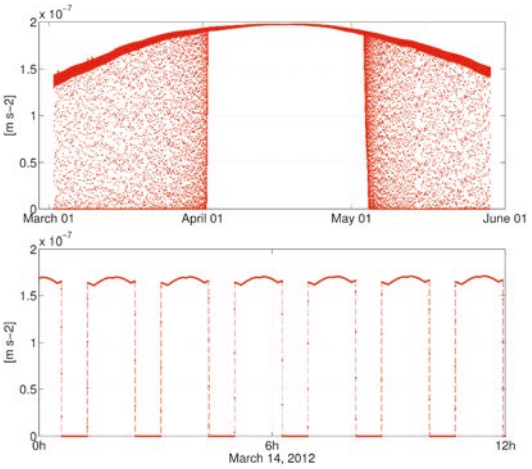

Fig. 1: Accelerations due to solar radiation pressure during the primary mission phase (top) and for half a day in March 2012 (bottom)

	GrazLGM200a	GrazLGM300a
Method	Integral equation approach using short arcs	
Arc length [min]	60	60
Spectral resolution	200	300
Evaluation period	March 2 – May 29, 2012	March 2 – May 29, 2012
A priori gravity field model	JGL165P1	JGL165P1
Planetary ephemeris	JPL DE421	JPL DE421
Spacecraft ephemeris	GNI1B, Release 02	GNI1B, Release 04
KBRR data	KBR1C, Release 02	KBR1C, Release 04
Thruster information	—	THR1B, Release 04
Satellite model	—	28-plate macro-model
Non-gravitational forces	—	Solar radiation pressure
Gravitational forces	Third body accelerations Solid Moon Tides	Third body accelerations Solid Moon Tides Relativistic (Schwarzschild)
Further estimates	—	Time bias Empirical parameters
Outlier handling	Individual weighting of arcs	Individual weighting of arcs
Regularization	—	—

Tab. 2: Standards and models used for the gravity field solutions GrazLGM200a and GrazLGM300a

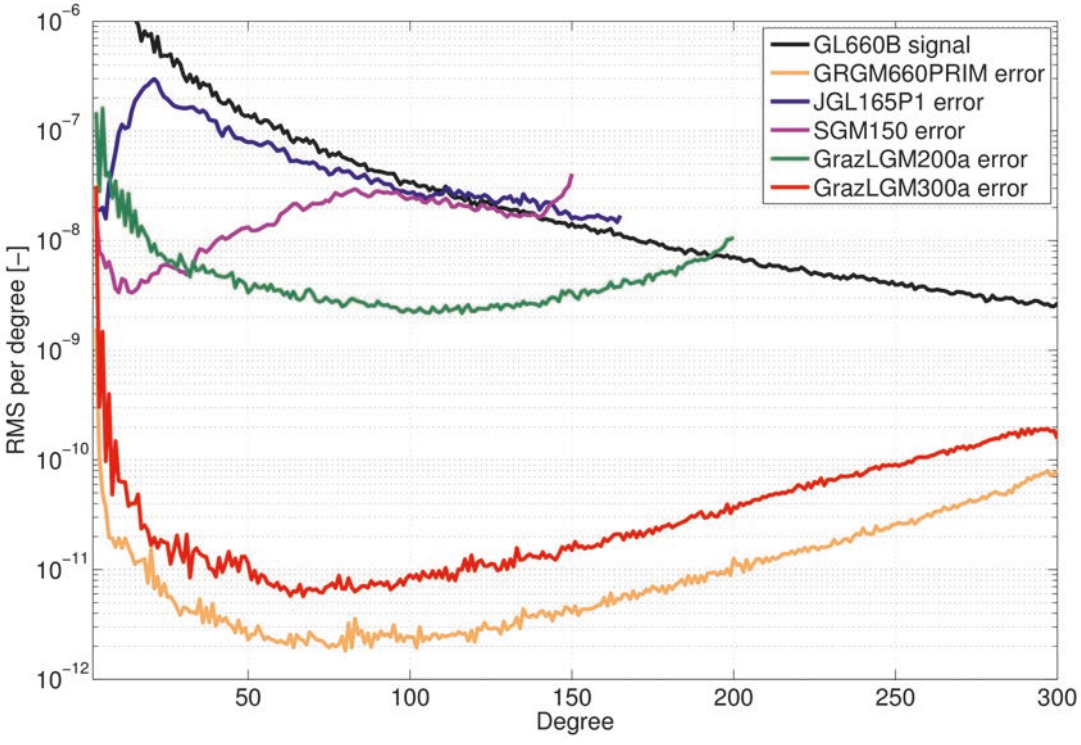

Fig. 2: RMS values per degree. Black solid graph: GL660B signal, other colors: differences to GL660B model.

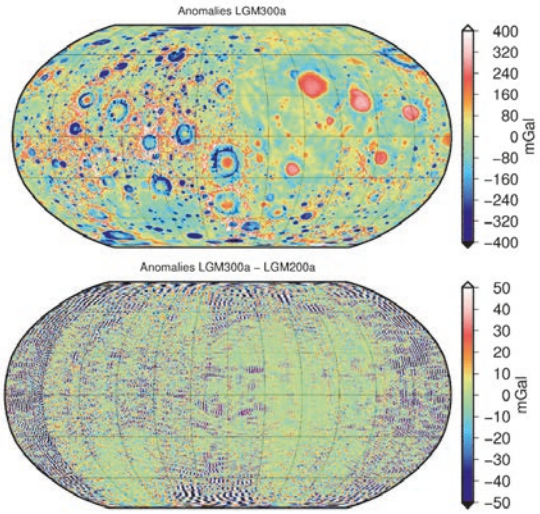

Fig. 3: Free-air gravity field anomalies, evaluated on a spherical 0.5×0.5 grid, top: GrazLGM300a bottom: difference GrazLGM300a-GrazLGM200a. [Projection is centered at 270° eastern longitude; nearside is on the right and the farside on the left of the figure]

of GL660B. Just like our own solutions, both of them are based on data from the primary mission only.

Even though the GrazLGM200a model (green) is based on the worse release 02 data set and considers only gravitational perturbations, it is already superior to the pre-GRAIL models JGL165P1 (LP; blue; [8]) and SGM150 (Selene; magenta; [17]) over almost the entire spectrum. This can be attributed to the high-precision inter-satellite observations of GRAIL and its global coverage. Beside the refined modeling and parametrization, especially the usage of the latest data release led to a distinctive improvement of the GrazLGM300a (red) model compared to GrazLGM200a. Furthermore, due to the correction of KBR data with GL660B (for d/o 301-660) our latest solution remains stable also at higher degrees, whereas GrazLGM200a is getting worse in the short wavelengths. It is gratifying to see that both solutions (GL660B and GrazLGM300a) have nearly the same structure over the whole spectrum and differ just about half an order of magnitude.

In terms of free-air gravity field anomalies the differences between these two models are in the range of ±2mGal, thus Figure 3 (top) shows only results based on the GrazLGM300a model; numerous craters are clearly visible on the near-side and farside of the Moon. In comparison, the GrazLGM200a model shows a much noisier picture on a global scale – mainly originating in the short wavelength range (Figure 3, bottom).

4. Discussion and conclusion

With the availability of high-precision inter-satellite observations by the GRAIL mission, lunar gravity mapping has raised to an unprecedented level in terms of accuracy and spatial resolution. Gravity models based on data from this outstanding mission perform significantly better than earlier models. Therefore, GRAIL gravimetry provides the opportunity to improve our knowledge about the interior structure and thermal evolution of the Moon.

As far as lunar gravity field recovery at the Space Research Institute of the Austrian Academy of Sciences is concerned, we showed that our latest model GrazLGM300a represents a distinctive improvement compared to the predecessor model. Apart from the spectral resolution, the model is close to those developed at NASA over the respective analysis period (primary mission phase). Open issues include the modeling of accelerations due to lunar radiation, the application of a more sophisticated self-shadowing technique, and a refined covariance handling.

Acknowledgement

The data for this study were made freely available by NASA; GRAIL orbit and inter-satellite information was retrieved from the Planetary Data System. We acknowledge financial support by the Austrian Research Promotion Agency (FFG) within the Austrian Space Application Program (ASAP, Phase 10, Project 844348).

References

[1] *Binder, A.B. (1998)*: Lunar Prospector: Overview. Science 4, 1475-1476.

[2] *Fahnestock, E.G., Park, R.S., Yuan, D.-N., et al. (2012)*: Spacecraft thermal and optical modeling impacts on estimation of the GRAIL lunar gravity field. AIAA/AAS Astrodynamics. Specialist Conference, Minneapolis, MN, AIAA, August 13-16.

[3] *Floberghagen, R. (2002)*: Lunar Gravimetry - Revealing the Far-Side. Kluwer Academic. Publishers, Dordrecht, The Netherlands.

[4] *Goossens, S., Matsumoto, K., Rowlands, D.D., et al. (2011)*: Orbit determination of the SELENE satellites using multi-satellite data types and evaluation of SELENE gravity fieldmodels, Journal of Geodesy 85, 487-504.

[5] *Klinger, B. Baur, O., Mayer-Gürr, T. (2013)*: GRAIL gravity field recovery based on the short–arc integral equation technique: Simulation studies and first real data results, Planetary and Space science, Vol. 91, pp. 83-90, 2014.

[6] *Klipstein, W.M., Arnold, B.W., Enzer, D.G., et al. (2013)*: The lunar gravity ranging system for the Gravity Recovery and Interior Laboratory (GRAIL) mission. Space Science Reviews 178, 57-76.

[7] *Konopliv, A.S., Binder, A.B., Hood, L.L., et al. (1998)*: Improved gravity field of the Moon from Lunar Prospector. Science 281, 1476-1480.

[8] *Konopliv, A.S., Asmar, S.W., Carranza, E., et al. (2001)*: Recent gravity models as a result of the Lunar Prospector mission. Icarus 150, 1-18.

[9] *Konopliv, A.S., Park, R.S., Yuan, D.N., et al. (2013)*: The JPL lunar gravity field to spherical harmonic degree 660 from the GRAIL primary mission. Journal of Geophysical Research: Planets 118, 1415-1434.

[10] *Konopliv, A.S., Park, R.S., Yuan, D.N., et al. (2014)*: High resolution lunar gravity fields from the GRAIL primary and extended mission. Geophysical Research Letters 41, 1452-1458, doi: 10.1002/2013GL059066.

[11] *Lemoine, F.G., Goossens, S., Sabaka, T.J., et al. (2013)*: High-degree gravity models from GRAIL primary mission data. Journal of Geophysical Research, Planets 118: 1676-1698.

[12] *Lemoine, F.G., Goossens, S., Sabaka, T.J., et al. (2014)*: GRGM900C: A degree 900 lunar gravity model from GRAIL primary and extended mission data. Geophysical Research Letters, 3382-3389, doi: 10.1002/2014GL060027.

[13] *Mayer-Gürr, T. (2006)*: Gravitationsfeldbestimmung aus der Analyse kurzer Bahnbögen am Beispiel der Satellitenmissionen CHAMP und GRACE. PhD Thesis, Rheinische Friedrich-Wilhelms-Universität zu Bonn.

[14] *Mayer-Gürr, T., Kurtenbach, E., Eicker, A. (2010)*: The satellite-only gravity field model ITGGrace2010s. Web: http://www.igg.uni-bonn.de/apmg/index.php?id=itggrace2010.

[15] *Montenbruck, O., Gill, E. (2000)*: Satellite Orbits: Models, Methods and Applications. Springer, Berlin, Heidelberg, New York.

[16] *Muller, P.M., Sjogren W.L. (1968)*: Mascons: Lunar Mass Concentrations. Science 16, 680-684.

[17] *Namiki, N., Iwata, T., Matsumoto, K., et al. (2009)*: Gravity field of the Moon from four-way Doppler measurements of SELENE (Kaguya). Science 323, 900-905.

[18] *Petit, G., Luzum, B. (2010)*: IERS Conventions (2010): IERS Technical Note 36, Frankfurt am Main: Verlag Bundesamt für Kartography und Geodäsie, 179 pp., ISBN 3-89888-989-6.

[19] *Tapley, B.D., Bettadpur, S., Ries, J.C., et al. (2004)*: GRACE measurements of mass variability in the Earth system. Science 305, 503-505.

[20] *Zuber, M.T., Smith, D.E., Watkins, M.M., et al. (2013)*: Gravity field of the Moon from the Gravity Recovery and Interior Laboratory (GRAIL) mission. Science 339, 668-671.

Contacts

Dr. techn. Sandro Krauss, Space Research Institute, Austrian Academy of Sciences, Schmiedlstrasse 6, A-8042 Graz, Austria.
E-Mail: sandro.krauss@oeaw.ac.at

Dipl.-Ing. Beate Klinger, Graz University of Technology, Institute of Theoretical Geodesy and Satellite Geodesy, Steyrergasse 30/III, 8010 Graz, Austria.
E-Mail: beate.klinger@tugraz.at

Dr.-Ing. Oliver Baur, Space Research Institute, Austrian Academy of Sciences, Schmiedlstrasse 6, A-8042 Graz, Austria.
E-Mail: oliver.baur@oeaw.ac.at

Univ.-Prof. Dr.-Ing. Torsten Mayer-Gürr, Graz University of Technology, Institute of Theoretical Geodesy and Satellite Geodesy, Steyrergasse 30/III, 8010 Graz, Austria.
E-Mail: mayer-guerr@tugraz.at

Scheduling Strategies for the AuScope VLBI network






David Mayer, Johannes Böhm, Wien; James Lovell, Lucia Plank, Hobart; Jing Sun, Bejing; Oleg Titov, Canberra

Abstract

In recent years Australia established the AuScope VLBI array which consists of three new 12-m radio telescopes across the continent (Hobart, Katherine and Yarragadee). With this network, the independent AUSTRAL observing program is carried out, regularly adding two more telescopes, the 12-m telescope in New Zealand and the 15-m telescope in South Africa. The observing plans (schedules) are created in Vienna, Austria and the correlation is done in Perth, Australia. The network engages in different AUSTRAL experiments (astrometric and geodetic) with contradictory aims, therefore scheduling approaches have to be adjusted to fit the required needs. We discuss the different techniques used to create these schedules, and provide first results, suggesting that solutions from the AuScope VLBI network are on a similar level of accuracy as standard global VLBI sessions performed by the International VLBI Service for Geodesy and Astrometry (IVS).

Keywords: VLBI, AuScope, Scheduling, Geodesy, Astrometry

Kurzfassung

In den letzten Jahren wurde in Australien das AuScope VLBI-Netzwerk errichtet. Es handelt sich um drei neue VLBI-Teleskope (Hobart, Katherine und Yarragadee), welche über den Kontinent verteilt wurden. Mit diesen drei Teleskopen, und gelegentlich zwei weiteren, dem 12-m-Teleskop in Neuseeland und dem 15-m-Telescop in Südafrika, wird das AUSTRAL Beoabachtungsprogramm durchgeführt. Die Beobachtungspläne (sogenannte Schedules) werden in Wien, Österreich erstellt und die Korrelation der Beobachtungen wird in Perth, Australien durchgeführt. Das AUSTRAL Beobachtungsprogramm beinhaltet verschiedene Experimente (astrometrisch und geodätisch) mit gegensätzlichen Zielen, weshalb die Methode zum Erstellen der Schedules den benötigten Anforderungen angepasst und erweitert werden muss. Wir diskutieren die verschiedenen Techniken, welche zum Erstellen dieser Schedules verwendet werden und präsentieren erste Resultate, die zeigen, dass das AuScope VLBI-Netzwerk Ergebnisse mit einem vergleichbaren Genauigkeitslevel wie globale VLBI-Experimente (durchgeführt vom International VLBI Service for Geodesy and Astrometry – IVS) liefert.

Schlüsselwörter: VLBI, AuScope, Beobachtungsplanung

1. VLBI introduction

Very Long Baseline Interferometry (VLBI) is one of the oldest space geodetic techniques. It uses radio telescopes to observe extra galactic radio sources (quasars) on the edge of the observable universe, which are assumed to be point-like and with no detectable proper motion. VLBI measurements of the positions of these fixed sources is used to define and maintain an inertial coordinate system which is used for many other applications. Furthermore, since VLBI-telescopes are fixed to the Earth's surface and the observed sources are fixed in the sky, a transformation from the terrestrial to the celestial system has to be implemented. As a result, transformation angles, the so called Earth Orientation Parameters (EOP), have to be estimated as well. VLBI is the only space geodetic technique which is capable of determining all five EOP (two angles for polar motion, one Earth rotation angle and two angles for nutation) at once.

One product which can only be derived from VLBI is the International Celestial Reference Frame (ICRF), with the newest realisation being the ICRF-2 (Ma et al. 2009). Furthermore, VLBI provides a major contribution to the International Terrestrial Reference Frame (ITRF), with the current release being the ITRF2008 (Altamimi et al. 2011). It is particularly important for the scale of the reference system. For more details on VLBI,

see Sovers et al. (1998) or Schuh and Böhm (2013).

2. AuScope Network

The AuScope VLBI array (Lovell et al, 2013) consists of three recently constructed (finished in 2010) 12-m telescopes, located in Hobart (Tasmania), Katherine (Northern Territory) and Yarragadee (Western Australia), see Figure 1, from here on referred to as Hobart12m, Kath12m and Yarra12m respectively. Other telescopes, such as the 15-m antenna at HartRAO (Hart15m), South Africa and the 12-m antenna in Warkworth (Wark12m), New Zealand, contribute to AUSTRAL sessions on a regular basis. The 26-m telescope in Hobart (Hobart26m) and the 26-m telescope at HartRAO (Hart26m) are utilised occasionally for special experiments.

The aims of the AuScope VLBI network are geodetic and astrometric. On one hand, the coordinate time series of telescopes should be precise and as long as possible which represents a geodetic goal. On the other hand, the number of observations of new and poorly observed sources in the Southern Hemisphere should be increased which resembles an astrometric goal. These aims are somewhat contradictory and require specific scheduling optimization. The geodetic sessions are split into normal geodetic sessions and special campaigns such as twin and continuous experiments. Twin sessions are used to study the implementation of twin telescopes (such as the co-located 12-m and 26-m telescopes) into the current VLBI framework. The term "twin telescopes", in the context of the VLBI2010 Global Observing System (VGOS, Petrachenko et al. 2009), refers to two identical, fast slewing telescopes which is not the case presented here, where we have two completely different telescopes at the same site (usually named "sibling telescopes" in the literature). However, since we named these experiments twin sessions, it makes sense to maintain consistency and keep the term twin telescopes for two different antennas at the same site.

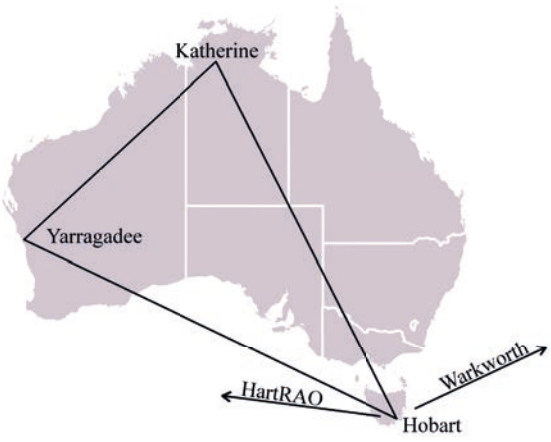

Fig. 1: Map of AuScope VLBI stations

The purpose of the continuous sessions (15 consecutive days) is to practice and establish continuous operation and enable determination of geodetic parameters with the highest accuracy, much like the recent CONT14, IVS campaign which is a 15 day experiment that incorporates a global network of 17 stations. More information on the AuScope VLBI array can be found in Lovell et al. (2013).

3. Scheduling

Sessions with different aims need different scheduling strategies. In this section we will provide information on the scheduling strategies used for all previously mentioned session types.

All schedules are created in Vienna, Austria using the Vie_SCHED module (Sun et al. 2014) of the Vienna VLBI Software (VieVS, Böhm et al. 2012).

Catalogue files, including all the necessary station specific information, such as antenna hardware and observing sensitivity, are updated and maintained in Hobart which gives us the ability to apply changes fast and use up to date information to create the schedules.

3.1 Geodetic sessions

The aim of the geodetic sessions in general is to estimate precise station coordinates. To do so the largest error source, which is the troposphere, has to be eliminated in the best possible manner. The best way to estimate the wet part of the troposphere in a geodetic session, is to schedule as many observations as possible and to spread them evenly in different directions (elevations and azimuths). In this sense, the sky coverage for each station is maximized in the schedule. This approach is called a station-based scheduling strategy (Sun et al 2014). The same basic principle is also applied for the continuous sessions.

The following parameters are set for the creation of a station-based schedule:

- SNR (signal to noise ratio) targets of 15 and 20 in S- and X-band respectively

- Minimum Sun distance of 4°
- Strong sources (>0.5 Jy) from the Goddard Space Flight Center source catalogue are used
- Minimum scan length is set to be 20 s
- Maximum scan length is set to be 200 s
- The same source will not be observed twice in 30 min
- No constraints were set for slewing time

The continuous campaigns 15 consecutive VLBI sessions with identical network geometries. The aim is to estimate parameters with the highest possible accuracy (similar to a regular geodetic session). Shabala et al. (2015) pointed out that the biggest systematic source of error, which is not accounted for in VLBI, is the structure of sources. This implies that the observed radio sources are not necessarily all point-like and could have structure that varies in both space and time. To account for this systematic effect we create special schedules which we will refer to as "sidereal schedules" from here on. The basic idea is to keep the angle (azimuth and elevation) at which a source is observed from the telescopes the same for each day, resulting in a constant error due to source structure. This will not decrease the effect of source structure, but the systematics stay the same and thus better baseline length repeatability can be expected. In order to schedule a sidereal session the difference between a solar day and a sidereal day (as seen in Figure 2) has to be accounted for. At

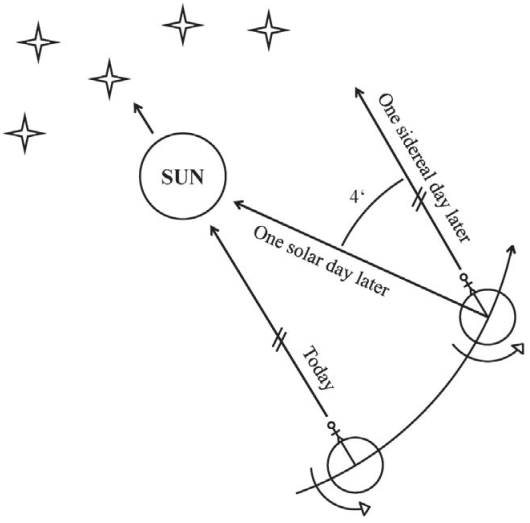

Fig. 2: Sketch to illustrate the concept of a sidereal day, which is approximately 4 minutes shorter than a solar day

a specific time on a sidereal day the geometry of the Earth w.r.t. the stars is always the same and therefore the angles between telescope and quasar are the same. A sidereal day is approximately four minutes shorter than a solar day.

3.2 Astrometric sessions

The aim of the AUSTRAL astrometric sessions is to generate observations of new or poorly observed sources. Historically there has always been fewer VLBI telescopes in the south, and therefore the observational history of the ICRF is highly imbalanced and southern sources are much less often observed and show higher positional uncertainties than northern ones (Ma et al. 2009). For the scheduling of the AUSTRALs, we use a special source list with new and poorly observed southern sources which is provided through private communication with O. Titov. It is updated on a regular basis and flux densities (the nominal strength of a source) are amended if necessary. The strategy for scheduling these experiments is slightly different from the one used for geodetic sessions. For astrometric sessions the scheduling is optimised to cover the entire celestial sky while for geodetic sessions the individual sky coverage at each station is considered. With this approach we can generate observations of as many sources as possible and still have an acceptable sky coverage at each station. This approach is called a source-based scheduling strategy.

Following parameters are set for the creation of the schedule (not listed parameters are the same as in the geodetic schedule):

- A special source list is maintained
- The maximum scan length is set to be 500 s

3.3 Special experiments

Sessions which use a combination of smaller (Hobart12m and Hart15m) and larger (Hobart26m and Hart26m) telescopes at the same site are called twin experiments. The aim of these sessions is to investigate the managing of twin telescopes in the scheduling, observation, correlation and analysis procedures. Combining different telescopes such as these (in terms of sensitivity and slew speed) in a single schedule is a complex task and is not yet included in the scheduling software packages by default.

In a first experiment two different schedules, one with the 12-m and 15-m telescopes and one with the 26-m telescopes were drafted and

combined afterwards. The fact that no connecting observations between the two sub-networks were scheduled caused trouble in the analysis chain and led to a subsequent separation of the original schedule into two sessions. This, however, will be corrected in the future.

Another twin experiment, which was conducted recently, included the Hobart26m telescope in a normal geodetic AuScope session. The aim was to schedule as many observations as possible with the Hobart12m – Hobart26m baseline and then test analysis implementations, such as combined troposphere and clock parameters.

In recent times (19.10.2014 and 09.01.2015) two experiments were performed with the aim of testing relativity. To do so observations in a short interval (3 minutes) of a quasar which came close to the Sun were included in the schedule. The sources 1334-127 and 1908-201 were used in the first and second session respectively. Only strong sources (>1 Jy) were used for these sessions.

3.4 Comparison of schedules

In Figure 3 the sky plots (for Hobart12m) of an astrometric (AUST72) and a geodetic session (AUST66) are compared. Both sessions use the same network which consists of the Hobart12m, Kath12m, Wark12m and Yarra12m telescopes. One can see that an astrometric session generates far fewer observations than a geodetic session (15 versus 75 sources in this case). This is due to the smaller source list and weaker sources (that require longer integration times) used in the astrometric mode. The source list for the astrometric session includes only sources with negative declination, which can be seen in the sky plot. The optimisation criteria for geodetic sessions is the individual sky coverage at each station which results in many observations at different elevations and azimuths, the distribution can be seen in the sky plot.

No constraints on slew time are set in the astrometric and geodetic schedules. This is justified by the fact that only fast antennas are observing in the network. Since weaker sources are used in an astrometric schedule the observing time is longer, and therefore less time is spent on slewing (e.g. 70 % of the total time is spent on observing and 7 % on slewing for the AUST72 session). In the geodetic mode only strong sources are utilised. Therefore, less time is spent on observing sources and more on slewing between observations (e.g. 49 % of the total time is spent on observing and 24 % on slewing for the AUST66 session).

The scheduling performed in Vienna is subject to steady improvement. In Figure 4 we show the total number of scans (black), the scans per hour (red) and the scan lengths (blue) for the observed AUSTRAL sessions. Astrometry sessions are marked in green. It is noted that the data

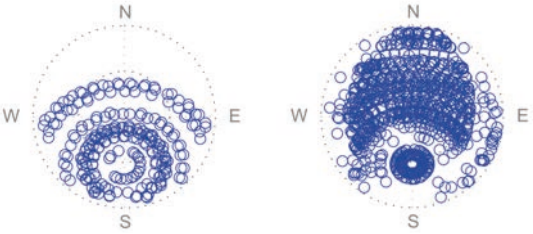

Fig. 3: Sky plot for the Hobart12m station, for the astrometric session, AUST72 (on the left) and the geodetic session, AUST66 (on the right)

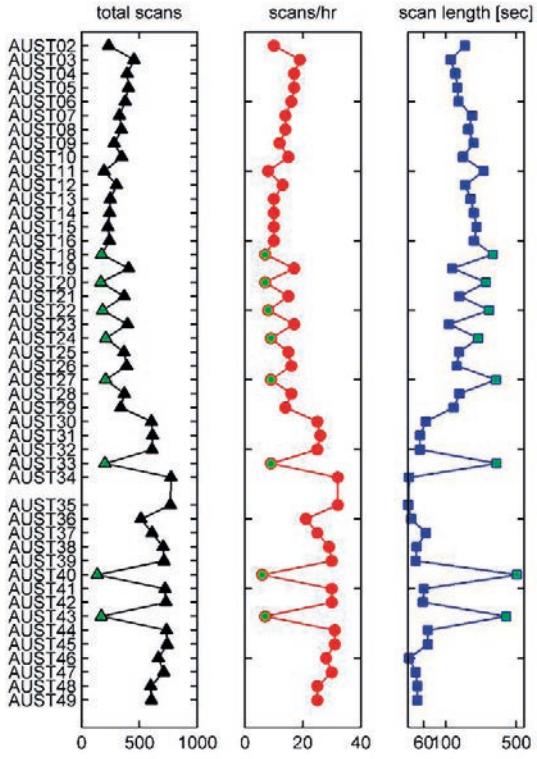

Fig. 4: Statistics of AuScope VLBI sessions. The plot on the left depicts the total number of scans per session. In the middle plot the average scans per hour per session are illustrated. On the right side the average scan length per session can be seen. Astrometric sessions are marked in green.

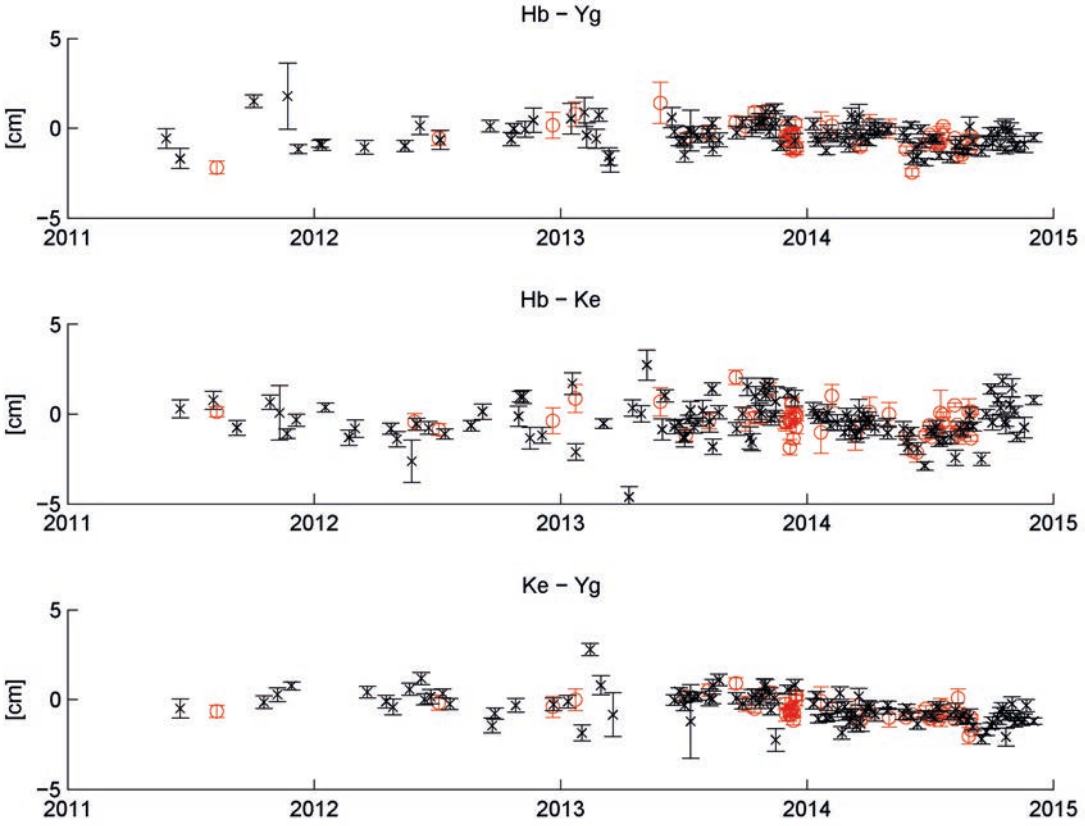

Fig. 5: Estimates and formal errors of AuScope baselines, from IVS-R1 and IVS-R4 sessions (in black), and from AuScope sessions (in red)

are from actual observed and correlated scans, which can differ from the original schedules due to bad observations or failures. The gradual improvement of scan length and scans per hour is clearly visible. This is due to the continuous enhancements of scheduling strategies and fine tuning of parameters as well as the improvement of data acquisition at the stations.

4. Results

In this section we will provide some results from the AUSTRAL sessions. Figure 5 depicts the baseline estimates and formal errors between the three AuScope VLBI telescopes. The results are from standard global IVS-R1 and IVS-R4 sessions where the AuScope VLBI network participated and from the AUSTRAL sessions (in red). We find good agreement between the estimates and formal errors from the AUSTRAL sessions and from the IVS sessions. Some systematic effects are still present in some baselines. The reason for this has not yet been identified and is subject to further research.

Table 1 lists the weighted root mean square error (wrmse) of the previously mentioned baselines calculated once from the IVS-R1/R4 sessions and once from the AuScope sessions. Overall the wrmse of baselines estimated with the AuScope sessions is better.

Figure 6 illustrates the distribution of source observations in the IVS-R1/R4 and AuScope VLBI sessions. One can see that the AuScope VLBI

	Ke-Yg	Hb-Ke	Hb-Yg
IVS-R1/R4	6,2	10,1	6,5
AuScope	4,6	7,3	6,9

Tab. 1: Weighted root mean square error of Australian baselines for R1/R4 and AuScope sessions in mm

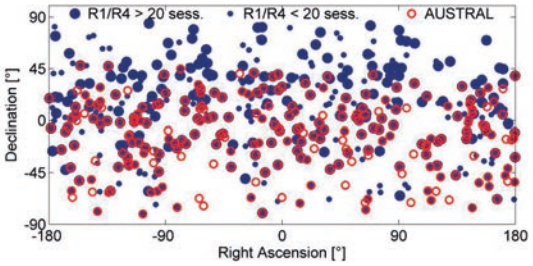

Fig. 6: The sky distribution of sources observed in IVS-R1/R4 and AuScope VLBI sessions. The size of the markers refers to the number of sessions this source was observed in.

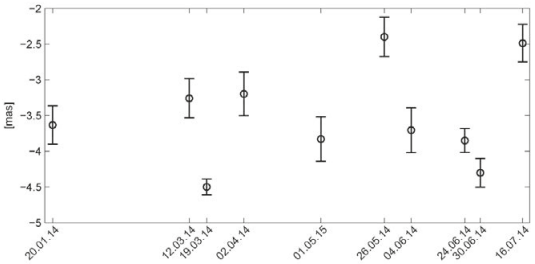

Fig. 7: Time series of the declination of the source 0758-737 estimated from AuScope VLBI sessions in 2014. This source has never been observed in S/X-band before and might complement future realizations of the ICRF.

network mainly observes sources in the Southern Hemisphere whereas the IVS-R1/R4 sessions by comparison observe primarily sources north of the Equator.

The astrometric sessions, observed with AuScope, are primarily dedicated to finding new suitable sources for the ICRF and generating observations to poorly observed sources. Overall, we found eleven (three were previously only observed in single X-band; five are non-defining and three are VCS sources, in both cases with a small number of observations) suitable sources for the ICRF, more details can be found in Plank et al. (2015). Faint sources, such as 0758-737 (the flux density was found to be 0.11 Jy in X-band and 0.21 Jy in S-Band) were observed, but many observations were lost due to the small dish size of the antennas. However, sources, such as 1842-289, with flux densities of 0.35 Jy in X-Band and 0.24 Jy in S-Band have a higher success rate. Therefore, a reasonable limit for flux densities is somewhere between 0.2 and 0.3 Jy for the current astrometric settings.

Besides using the AUSTRAL astrometric sessions to increase the number of observations of poorly observed sources in the south, we also search for new sources potentially suitable for future realizations of the ICRF. In Figure 7 the time series of the declination of the source 0758-737, a source that has never been observed at S- and X-band before, is shown. The right ascension experiences no significant offset and is therefore not illustrated. Estimates from this source (up to –4 mas) reveal an offset with respect to the a-priori coordinate, which was taken from previous single frequency X-band observations. On one hand, this could suggest that the data obtained from dual frequency, S- and X-band, observations are more accurate than data from single frequency X-band observations only. On the other hand, it could be an indicator that the center of emission is frequency dependent. However, recent observations with the New Technology Telescope (NTT, ESO) in Chile revealed that the radio source 0758-737 is well aligned with a foreground star (less than 2", O. Titov, private communication). Therefore, the data could also suggest that the offset is due to a constant light deflection effect.

5. Conclusion

The AuScope VLBI network takes part in different (geodetic, astrometric and special) AUSTRAL experiments with contrasting goals. Distinct scheduling strategies have to be applied to accomplish the desired results. A close cooperation between scheduler, observer and correlator is maintained which facilitates the adaption and enhancement of the scheduling strategy to meet the desired goals.

The results from the geodetic VLBI experiments suggest that the regional AUSTRAL sessions deliver reasonable results which are comparable with estimations from global IVS-R1 and IVS-R4 sessions. However, some baselines experience a systematic movement which can be seen in both the IVS and the AuScope sessions. The reason for this movement is not yet clear and is subject to further research.

The astrometric sessions provide observations of new and poorly observed sources in the south, that can be used to expand catalogues of reference sources in the south and to improve source positions.

Acknowledgements

This paper is based on observations collected at the European Organisation for Astronomical Research in the Southern Hemisphere, Chile (092.A-0021(A)).

References

Altamimi Z., Collilieux X., Métivier L. (2011): ITRF2008: an improved solution of the international terrestrial reference frame. J Geod 85(8): pp 457–473.

Böhm J., Böhm S., Nilsson T., Pany A., Plank L., Spicakova H., Teke K., Schuh H. (2012): The new Vienna VLBI software VieVS. In: Proceedings of the 2009 IAG symposium, Buenos Aires, 31 Aug. - 4 Sept 2009. International Association of Geodesy Symposia, vol 136, pp 1007–1011.

Lovell J., McCallum J., Reid P., McCulloch P., Baynes B., Dickey J., Shabala S., Watson C., Titov O., Ruddick R., Twilley R., Reynolds C., Tingay S., Shield P., Adada R., Ellingsen S., Morgan J., Bignall H. (2013): The auscope-geodetic VLBI array. J Geod. 87(6): pp 527–538.

Ma C. et al. (2009): The second realization of the international celestial reference frame by very long baseline interferometry. IERS technical note 35, 1. Verlag des Bundesamts für Kartographie und Geodäsie, Frankfurt am Main.

Petrachenko B., Niell A., Behrend D., Corey B., Böhm J., Charlot P., Collioud A., Gipson J., Haas R., Hobiger T., Koyama Y., MacMillan D., Malkin Z., Nilsson T., Pany A., Tuccari G., Whitney A., Wresnik J. (2009): Design aspects of the VLBI2010 system. Progress report of the IVS VLBI2010 committee, Technical report. http://ads-abs.harvard.edu/abs/2009vlbi.rept....1P .

Plank L., Lovell J., McCallum J., Rastorgueva-Foi E., Shabala S., Böhm J., Mayer D., Sun J., Titov O., Weston S., Gulyaev S., Natusch T., Quick J. (submitted 2015): Results from the regional AUSTRAL VLBI sessions for southern hemisphere reference frames. In: Proceedings of the IAG Commission 1 Symposium 2014: Reference Frames for Applications in Geosciences (REFAG2014) 13-17 October 2014, Kirchberg, Luxembourg.

Schuh H., Böhm J. (2013): Very long baseline interferometry for geodesy and astrometry. In: Xu G (ed) Sciences of geodesy-II. Springer, Berlin, pp 339–376.

Shabala S., McCallum J., Plank L., Böhm J. (2015): Simulating the effects of quasar structure on parameters from geodetic VLBI, submitted to J Geod.

Sovers O.J., Fanselow J.L., Jacobs C.S. (1998): Astrometry and geodesy with radio interferometry: experiments, models, results. Rev Mod Phys 70(4): pp 1393–1454.

Sun J., Böhm J., Nilsson T., Krásná H., Böhm S., Schuh H. (2014): New VLBI2010 scheduling strategies and implications on the terrestrial reference frames. J Geod 88(5): pp 449–461.

Contacts

Univ.Ass. Dipl.-Ing. David Mayer, Technische Universität Wien, Department für Geodäsie und Geoinformation E120.4, Gußhausstraße 27-29, 1040 Wien, Austria.
E-Mail: david.mayer@geo.tuwien.ac.at

Univ.-Prof. Dr. Johannes Böhm, Technische Universität Wien, Department für Geodäsie und Geoinformation E120.4, Gußhausstraße 27-29, 1040 Wien, Austria.
E-Mail: Johannes.Boehm@geo.tuwien.ac.at

Dr. James Lovell, University of Tasmania, School of Physical Sciences, Private Bag 37, Hobart, Tas 7001, Australia.
E-Mail: jim.lovell@utas.edu.au

Dr. Lucia Plank, University of Tasmania, School of Physical Sciences Private Bag 37, Hobart, Tas 7001 Australia.
E-Mail: lucia.plank@utas.edu.au

Dr. Jing Sun, National Key Laboratory of Science and Technology on Aerospace Flight Dynamics, Beijing Aerospace Control Center, Beijing, China.
E-Mail: sunjing@shao.ac.cn

Oleg Titov, Ph.D., PO Box 378, Canberra ACT 2601, Australia.
E-Mail: oleg.titov@ga.gov.au


OLG REPRO2 – Start of reprocessing the densification networks

Philipp Mitterschiffthaler and Günter Stangl, Graz

Abstract

OLG (Observatory Lustbuehel Graz) as a joint cooperation of the AAS (Austrian Academy of Sciences) and the BEV (Bundesamt für Eich- und Vermessungswesen) acts also as an international analysis center for GNSS networks since more than 20 years. Apart from the EPN (European Reference Frame Permanent Network) sub-network four densification networks are permanently analyzed with regions in Austria, Central Europe, Greece and around the Arabian Plate. Now the international REPRO2 project enables the reprocessing of about 20 years of data using reprocessed orbits and clocks and new models of the ionosphere and troposphere to reach a precision near several millimeters. The first results and comparisons of the years 2006 and 2007 are presented.

Keywords: GNSS, reference networks, geokinematics, time series, reprocessing

Kurzfassung

OLG (Observatorium Lustbühel Graz) ist ein Gemeinschaftsprojekt der ÖAW (Österreichische Akademie der Wissenschaften) und des BEV (Bundesamt für Eich- und Vermessungswesen). Ein Teil davon ist das internationale Auswertezentrum für GNSS-Netze, das seit mehr als 20 Jahren aktiv ist. Außer dem Sub-Netz des EPN (European Reference Frame Permanent Network) werden vier weitere Netze permanent bestimmt. Die regionalen Schwerpunkte sind dabei Österreich, Mitteleuropa, Griechenland und die Arabische Platte. Das internationale Projekt REPRO2 macht es möglich, dass die Beobachtungen der letzten 20 Jahre mit Bahndaten im aktuellen Referenzsystem und neuen Modellen von Ionosphäre und Troposphäre in einer Genauigkeit von wenigen Millimetern neu ausgewertet werden. Die ersten Resultate der Jahre 2006 und 2007 werden im Vergleich mit den früheren Resultaten vorgestellt.

Schlüsselwörter: GNSS, Referenznetzwerke, Geokinematik, Zeitserien, Reprocessing

1. Introduction

More than 20 years ago the analysis of GNSS signals (at that time GPS only) started to introduce a modern 3D-reference frame. State of the art models have been used to achieve a precision of centimetres. The models of orbits, clocks, ionosphere, troposphere, the antenna calibration and other parameters have been improved since that time. Therefore the coordinates can be estimated almost at the millimetre level. Stacking old and new solutions together results in a time series of products containing systematic biases. This degrades the results even the GNSS signals would have provided better results since the beginning. When it was possible to combine GPS and GLONASS the analysis had to be extended.

The first IGS reprocessing, called repro1, started in 2008 to compute orbits and station coordinates[1]. Afterwards repro2 started in 2013 and is expected to finish within short time[2]. The goal is to provide a modern and precise contribution to the current geodetic reference frame, e.g. ITRF2014 (International Terrestrial Reference Frame 2014) coming soon. OLG (Observatory Lustbuehel Graz) is contributing to the densification of ITRF on a regional basis. Out of the four different regions (Austria, Central Europe, Greece, Eastern Mediterranean) the Austrian part is presented in the article. The usual products are weekly coordinate results in SINEX (Solution Independent Exchange) formats. For climatology also zenith troposphere delays are provided too. Reference frames are not only mandatory for geodetic issues but also for several geo-related sciences, like climatology and tectonics [1].

The densification networks of OLG as a joint cooperation between the Federal Office of Metrology and Surveying (BEV) and the Austrian Academy of Sciences (AAS) have two main targets: geodetic reference and reference for geokinematics as a part of modelling crustal deformations. Analysing permanent GNSS stations with international standards the products of time series refer to different models and references and ignored completely GLONASS until 2014. The time series of coordinates combining the different results cause systematic biases which cannot be neglected by increasing the precision to a target of ± 1 mm. The need of improving this

1) http://acc.igs.org/reprocess.html
2) http://acc.igs.org/reprocess2.html

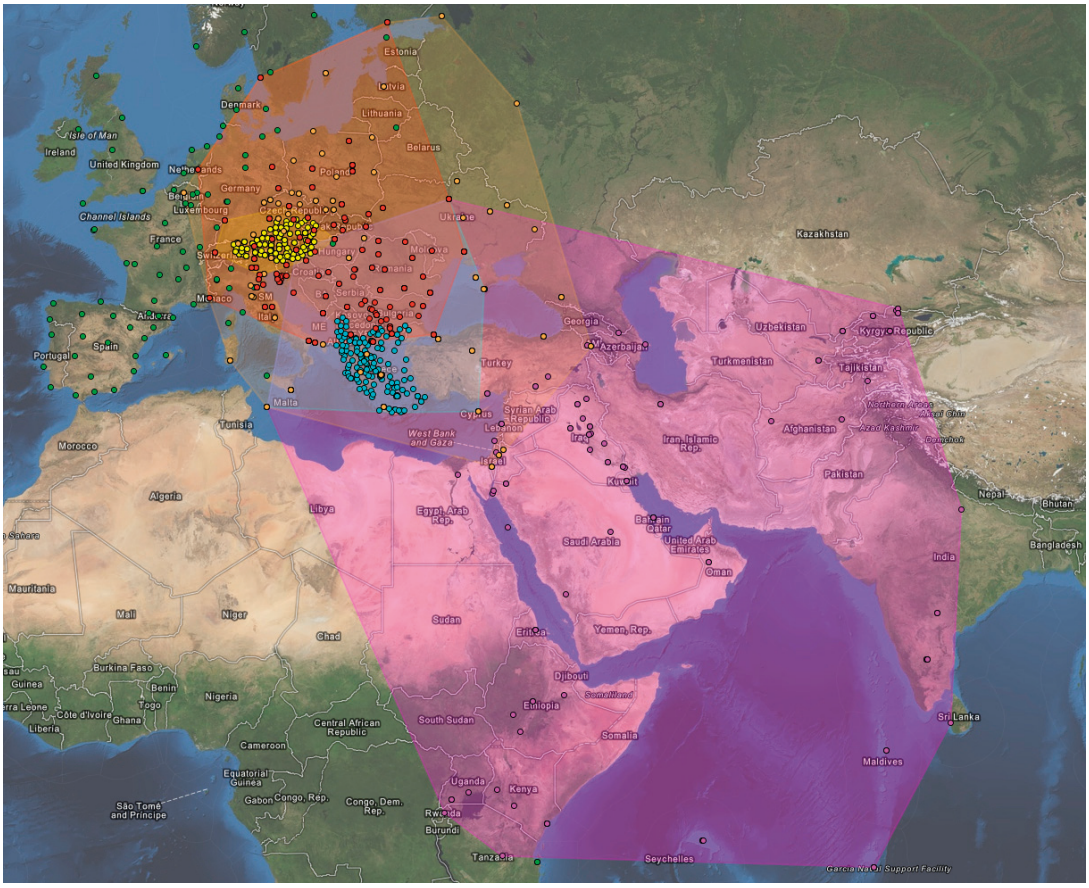

Fig.1: Geographical overview of AMON (yellow), CERGOP (red), GREECE (cyan) and MON (magenta) with selected stations for REPRO2

situation was felt several years ago also at OLG. A small repro1-type effort was done in 2012, only for the Austrian Network and a subnetwork of EPN (EUREF Permanent Network) of year 2006. With new resources, new models and the switch to an analysis of both GPS and GLONASS in 2014 the decision was made to start with the actual analysis like repro2. The features of repro2 were adopted for all OLG networks except EPN. The results should follow the guidelines of the IAG (International Association of Geodesy) Working Group "Integration of dense velocity fields into the ITRF"[3] [2] even if the results will come too late for the new ITRF2014 publication. It is supposed that the work will continue. A further decision was made that OLG REPRO2 should start with the year 2006 because the number of stations increased significantly at that time. The first step would be a reprocessing of the years 2006–2014. The second step should follow with years 2006 back to 1994. The final step should be the inclusion of epoch campaigns 1992–2012 mainly within and around Austria. The reprocessing started late in 2014 with 2006 and is still in progress. Since 2014 the actual weekly results are submitted to the IAG Working Group mentioned above to support the densification. Concerning the reprocessing IAG working group (representation European densification) decided to take over only a reprocessing of all years, therefore the results have to be stored meanwhile.

2. Data Overview

With an increase in the number of stations the extent and also the numbers of analysed networks increased. Presently there are four networks outside the EPN contribution, AMON (Austrian Monitoring Network), CERGOP (Central European Research on Geodynamics Project), GREECE and MON (Monitoring Oriental Network).

3) http://iagvf.oma.be/index.php?page=final_guidelines

While AMON's first target is the monitoring of the Austrian reference tied to ETRS89 (European Terrestrial Reference System 1989), CERGOP tracks intraplate movements of the Eurasian Plate in Central Europe, GREECE the boundary zone between Eurasian Plate, Nubian Plate, Anatolian Plate and diverse other plate fragments around the southern Balkan Peninsula. MON finally is determined to track the movements of the Arabian Plate against its surrounding plates. Between 2006 and 2014 the number of stations to be processed raised from approximately 250 to 400. Before 2006 the numbers drop significantly because several parts are not covered at all or with poor station density (e.g. Greece). In general the networks to be reprocessed contain more stations than those submitted every week for densification. The reason is the inclusion of former stations and also stations with a long history to get a better reference in early times are added. Providing IGb08 values as constraints are consistent and there should be no significant biases due to varying numbers of reference stations within the last 20 years. An overview of the networks is shown in Figure 1.

OLG REPRO2 is mainly focussed on positions, velocities and zenith troposphere delays of the stations. Therefore GNSS orbits and clocks, pole rotations, tidal corrections etc. will be taken from repro2 results of IGS (International GNSS Service) even though they are provisional. The guidelines of analysis are taken from EPN[4]. As reference sites several IGS and EPN sites with their coordinates and velocities in IGb08 (update IGS 2008) are taken trying to have a well distributed coverage if possible. The antenna calibration values are taken also from IGb08, combining IGS, EPN and national (individual) values.

3. Analysis Strategy

For analysis the Bernese Software version 5.2 was used[5]. The processing is based on the guidelines of EPN analysis centres in the current form[6]. They demand a combination of GPS and GLONASS observations. Some adaptions to the guidelines have been made. The GPS and GLONASS orbits and clocks are taken from IGS repro2 and for the troposphere a priori models the VMF1 (Vienna Mapping Function [4]) was chosen. The data were combined to baselines which formed the four networks shown above. It was decided to keep the four networks in general without change to a clustering of all stations into one network. This decision was more a matter of different institutional targets (IAG and BEV, reference frames, CERGOP and others, geokinematics) than keeping the traditional way. Having enough overlapping stations the networks can be combined for a single densification solution as well as the single networks may be submitted to special users and contributors of data. The clustering has to be introduced around 2010 when the number of stations in some networks (AMON, GREECE) starts to reach the number of 100 stations for analysis. At present the computation time of the networks increases exponentially with the number of stations. The final step for one day needs about four minutes for 50 stations while it increases to 25 minutes with 100 stations.

For the analysis the Bernese Processing Engine is used as an automatic procedure to produce results from observations and other inputs. Having different stations from different sources which do not fulfil the IGS and EPN [5] guidelines sometimes a pre-analysis is necessary to add or change meta-information. Also stations with bad data have to be eliminated during the automatic reprocessing. Finally the results are checked by stacking the daily normal equations to a time series which should show outliers, discontinuities or biases by bad referencing stations.

4. First Results and Comparisons

In Table 1 the number of analysed stations for REPRO2 in 2006 and 2007 is shown. The increase of the number of stations from 2006 to 2007 is clearly seen. For all networks an increase can be seen which proceeds until today. Figure 2 and Figure 3 show the changes of the time series for one example station ASCH (Aschau) in Germany. The part of 2006 was already corrected by repro1. Therefore the differences are quite small

Network	Number of stations analysed	
	2006	2007
AMON	87	99
CERGOP	64	80
GREECE	27	39
MON	51	75

Tab. 1: Number of analysed stations for years 2006 and 2007

4) http://www.epncb.oma.be/_documentation/guidelines/guidelines_analysis_centres.pdf

5) The manual is not yet published. Basic features can be seen in [3], the manual of version 5.0

6) http://www.epncb.oma.be/_documentation/guidelines/guidelines_analysis_centres.pdf

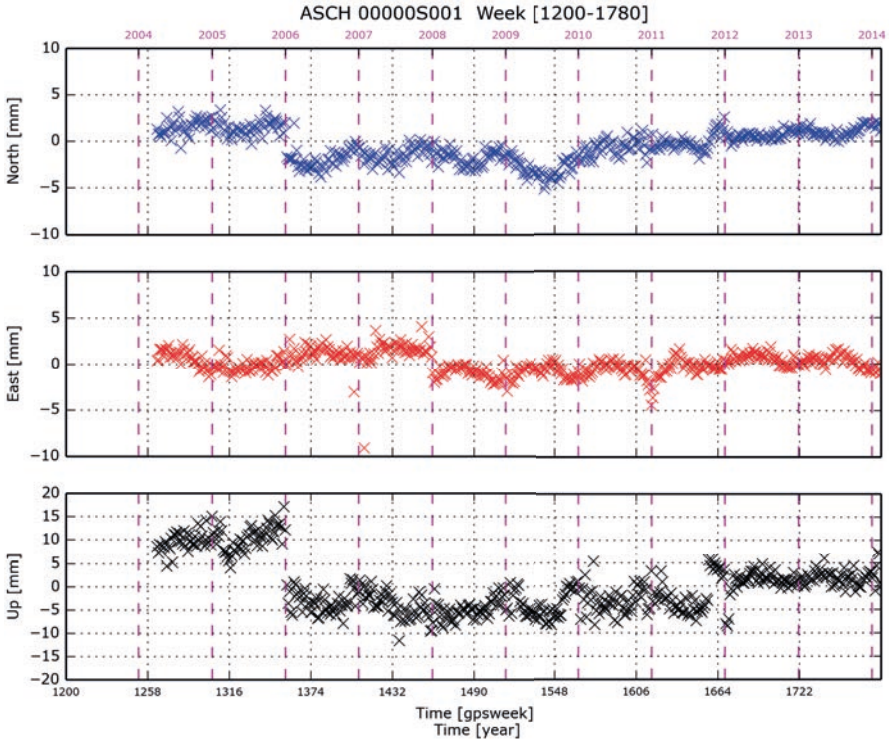

Fig. 2: Example of time series for station ASCH (Aschau, Germany) with REPRO2 2006+2007 included

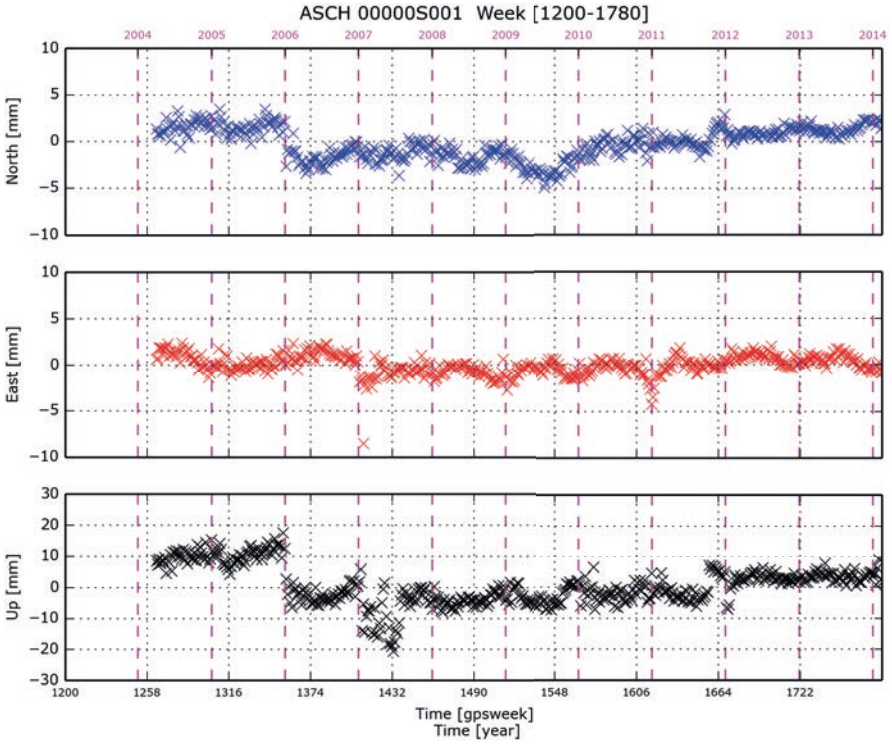

Fig. 3: Example of time series for station ASCH (Aschau, Germany) without REPRO2, but with repro1 2006

because repro1 already improved the original results as can be seen in Figures 2 and 3. The jump in the Up-component before 2006 was located originally in 2006 at GPS week 1400 when several models were changed according to the international standards. However, the 2007 part shows a clear improvement in the Up-component by reducing the largest values from over 20 mm to less than 10 mm. It is assumed that the improved troposphere model is responsible for the reduction.

5. Progress

It is estimated that each year of REPRO2 will need up to two months of work. The improved knowledge of handling wrong or missing meta-information and the increased number of stations will compensate. It is assumed that the effort will remain the same for each year. This would mean that 2015 the years 2006–2013 might be finished in REPRO2. Before 2006 the amount of computer time will be reduced dramatically but the human input of organizing and pre-analysis will increase. There is hope to reduce the effort to one month per year. REPRO2 should basically be terminated by the end of 2016. A further add-on will be started in 2017 to include all valid campaigns within and around Austria (about 300 sites) between 1992 and 2014. While the computation time can be neglected, the time for organization (e.g. correlation of different naming in Austria and internationally) is crucial. There is a pressure on OLG to finish REPRO2 in time for a densification of the international reference frame. Additionally a consistent time series is essential to estimate station velocities for geokinematics. Especially in areas with small intraplate distortions a precision at the millimetre level is requested. There is hope that REPRO2 will be completely finished in 2017 and might be followed by a REPRO3 if it is recommended by the IAG.

Acknowledgement

Many thanks go to the Federal Office of Metrology and Surveying (BEV) in Austria and to the members of the CEGRN Consortium for providing private data for the reprocessing. Also thanks to the Space Research Institute (IWF) of the Austrian Academy of Sciences which provided the computation facilities.

References

[1] *Z. Altamimi, X. Collilieux (eds.)*: Reference Frames for Applications in Geosciences, International Association of Geodesy Symposia 138, Heidelberg, New York, Dordrecht, London, 2013, 137-145.

[2] *C. Bruyninx, J. Legrand, Z. Altamimi, M. Becker, M. Craymer, L. Combrinck, A. Combrink, J. Dawson, R. Dietrich, R. Fernandes, R. Govind, J. Griffiths, T. Herring, A. Kenyeres, R. King, C. Kreemer, D. Lavallée, L. Sánchez, G. Sella, Z. Shen, A. Santamaría-Gómez, G. Wöppelmann*: IAG WG SC1.3 on Regional Dense Velocity Fields: First Results and Steps Ahead, International Association of Geeodesy Symposia Volume 138, 2013, 137-145.

[3] *R. Dach , U. Hugentobler, P. Fridez, M. Meindl, (2007)*: Bernese GNSS Software Version 5.0., Astronomical Institute, University of Bern.

[4] *J. Boehm, H. Schuh (2004)*: Vienna Mapping Functions in VLBI analyses, Geophys. Res. Lett., 31, L01603, doi:10.1029/2003GL018984.

[5] *C. Bruyninx (2004)*: The EUREF Permanent Network: a multi-disciplinary network serving surveyors as well as scientists, GeoInformatics, Vol 7, pp. 32-35.

Contacts

Dipl.-Ing. Philipp Mitterschiffthaler, Federal Office of Metrology and Surveying, Körblergasse 25, 8010 Graz, Austria.
E-Mail: philipp.mitterschiffthaler@bev.gv.at

Dipl.-Ing. Mag. Dr. phil. Günter Stangl, Federal Office of Metrology and Surveying, Körblergasse 25, 8010 Graz, Austria; Space Research Institute, Austrian Academy of Sciences, Schmiedlstrasse 6, 8042 Graz, Austria.
E-Mail: günter.stangl@oeaw.ac.at


Performance Evaluation of the Use of a Low-cost High Sensitivity GPS (HS-GPS) Receiver in Forests

Günther Retscher, Wien; Severin Heuböck, Sankt Pölten

Abstract

For many precise navigation and surveying applications in forests, such as the navigation of tractors, harvesters and forest machines, as well as static cadastral surveys or the determination of the size of agricultural land for European Union funding, the use of low-cost GNSS receivers has become increasingly popular. High Sensitivity GPS (HS-GPS) receivers are frequently employed for these tasks because they provide higher availability and good performance even under unfavourable satellite visibility conditions. This study investigates the practicability of the usage and the achievable quality of a certain low-cost HS-GPS receiver under forest canopy in such types of applications. Different test areas in deciduous, coniferous and young forests representing variations of kind, age and form of trees were selected. Long-term observations in summer, winter and autumn over at least two days at ten selected test points were carried out. Hence, several tests under varying states of foliation could be evaluated which clearly show the influence of the type of forest, tree height and foliage moisture as a matter of the season. It was found that the performance of a HS-GPS receiver is acceptable and static single point positioning generally performs well for the above mentioned applications. For static code measurements the mean horizontal deviations range from few dm up to 2 m with a standard deviation of around 8 m depending on season and length of the observation time. In the case of carrier phase solutions from baseline observations to a virtual reference station, however, a significant reduction of signal quality is seen. Using robust estimation, the influence of outliers could be efficiently reduced. Single frequency relative positioning with robust estimation then yielded a median deviation of less than 10 cm with an interquartile range (IQR) of around 3 m.

Keywords: Low-cost HS-GPS, forest canopies, HS-GPS performance analysis

Kurzfassung

Immer häufiger werden heute low-cost GNSS-Empfänger für viele Navigations- und Vermessungsanwendungen im Wald verwendet. Typische Anwendungen sind die Navigation von Traktoren und anderen Forstmaschinen, Katasteraufgaben, sowie die Bestimmung von förderungswürdigen Flächen für Förderungsprogramme der EU. Sehr oft werden hier High-Sensitivity GPS (HS-GPS) Empfänger verwendet, da sie auch unter schlechten Empfangsbedingungen eine hohe Verfügbarkeit aufweisen und Positionslösungen berechnen können. Diese Studie untersucht die Möglichkeiten der Verwendung und die erreichbaren Genauigkeiten eines HS-GPS Empfängers im Wald. Um die Einflüsse von Art, Alter und Höhe zu untersuchen, wurden mehrere Testgebiete in Nadel-, Laub- und Jungwald bestimmt. Im Winter, Sommer und Herbst wurden Messungen über mindestens zwei Tage an zehn vorher bestimmten Messpunkten durchgeführt. Dadurch konnten in den Auswertungen der Einfluss der vorherrschenden Baumart, Baumhöhe und der saisonal bedingten Änderungen des Blätterdaches bestimmt werden. In dieser Testreihe funktionierte der HS-GPS Empfänger zufriedenstellend und auch die statische Positionsbestimmung erwies sich als einsetzbar für die betrachteten Anwendungen. Statische Codemessungen zeigten eine mittlere Lageabweichung von wenigen dm bis zu 2 m mit einer Standardabweichung von rund 8 m abhängig von der Jahreszeit und Beobachtungslänge. Werden Trägerphasenlösungen im Zuge einer Basislinienmessung zu einer Referenzstation bestimmt, ist eine deutliche Verschlechterung der Signalqualität festzustellen. Durch robuste Schätzverfahren kann der Einfluss grober Fehler effektiv reduziert werden. Relative Einfrequenzmessungen mit robusten Fehlerdetektion führt zu einem Median von unter 10 cm mit einem Quartilabstand von rund 3 m.

Schlüsselwörter: Low-cost HS-GPS, Waldbedeckung, HS-GPS Leistungsuntersuchung

1. Introduction

GNSS is employed in numerous situations and the use of low-cost receivers in particular has become very popular [2]. Owing to applications in challenging environments, such as in urban canyons or covered areas, it has become very important to further develop GNSS receiver technology and measurement data analysis. A strong impact came from the mobile phone sector in which new more powerful electronic components have been developed. It was possible to build receivers which have a much better performance and higher positioning capabilities. These are called High Sensitivity GPS (HS-GPS) receivers. In contrast to conventional receivers they have millions of integrated correlators. The u-blox LEA-6T receiver used in this study has two million correlators and can acquire signals as

low as –178 dBW. Owing to improved calculating capacities new 'deep' GPS signal search techniques, such as non-coherent integration (see [1]), can be used. Owing to higher calculating capacity the time-to-first-fix can be reduced to less than one second. Under severe conditions, however, the integration time can be extended up to thousand milliseconds [3].

In forests particularly GPS signals are scattered by foliage. Multipath is the major problem due to signal reflections and diffraction effects. This causes that conventional low-cost GPS receivers have serious problems in acquiring and tracking GPS signals. HS-GPS receivers, on the other hand, can acquire signals and track them even under these unfavourable conditions. This study investigates the practicability of a low-cost HS-GPS for usage under forest canopies. The research hypothesis is that low-cost HS-GPS receivers are suitable for applications such as the navigation of forest machines, static cadastral surveys or the determination of the size of agricultural land for European Union funding. The performance is demonstrated by providing general information of accuracy and reliability.

2. Test set-up and data processing

In cooperation with the Austrian Federal Forest Department (ÖBF) a test area near Pressbaum in the Wienerwald west of Vienna was selected. The Wienerwald is a mixed forest with heterogeneous variations in kind, age and form of trees in a relatively small area. As the definition of forest varies also the physical characteristics of wood vary. Therefore ten survey points were established in the test area located in miscellaneous types of forest, i.e., deciduous, coniferous and young forest. The height of the trees was 10 to 20 m in the deciduous and coniferous forest and 5 m in the young forest. The ten test points were conventionally surveyed with traversing using a total station and embedded into a local GPS network. Their standard deviation is in the range of around 1 cm. Long-term static observations of 24 h periods were performed at least twice on each survey point in different measurement campaigns. To cover the whole vegetation cycle measurement campaigns were carried out in three different seasons with different states of foliage. The first one was in summer with moist foliage, the second in October with dry foliage and the last in March without leaves on the trees. In this study a u-blox LEA-6T receiver which also logged the raw data for post processing was used with its standard antenna. For the static measurements the antenna was mounted on a tripod. A thorough analysis of the great number of observations was done in post processing using Leica GeoOffice (LGO) in several ways, i.e., code single point positioning (SPP) solutions using broadcast ephemeris with and without EGNOS corrections, relative carrier phase positioning solutions using baselines to a virtual reference station in the Austrian EPOSA CORS network and the use of either broadcast or precise ephemeris. The different solutions are compared with the absolute coordinates of the survey points. In the following sections selected results of the extensive study are presented.

3. Code solutions

First of all, real time C/A code solutions under open sky and with foliage were carried out to analyse the receiver general performance. Figure 1 on the right visualizes the deviations from the ground truth for the code single point solution of a 24 h session on two survey points, one under open sky (left) and one with coniferous canopy (right). The elevation cut-off angle was set to 15°. The loss of positioning accuracy under forest canopy can easily be seen in the deviation maps. The standard deviation of 2.9 m under open sky increased crucially with foliage. This loss of accuracy is a consequence of the lower signal to noise ratio (SNR). The average C/N_0 as indicator of the SNR decreased from 42.2 dB under open sky to 34.8 dB under canopy.

In the following, three different code SPP solutions of the observations in the forest were analyzed (see Table 1). Solution 1 is a single epoch real-time SPP solution over a 24 h session which was then divided into 3 h observation windows (solution 2) to analyse how static measurements perform over shorter time spans. From the 24 h observation time the resulting deviations of a certain 3 h window are given in the Table. In these tests SBAS-aid (i.e., EGNOS) and receiver autonomous integrity monitoring (RAIM) for blunder detection were used. From the resulting coordinates deviations to the absolute coordinates of the survey test points were calculated. The average horizontal deviations of solution 2 are similar to the one of solution 1, but their standard deviations are far better, i.e., they are around 3 m. The reason for this is that in the certain 3 h session fewer outliers are present. Solution 3 is a post processed SPP solution over 24 h without SBAS and RAIM. The larger horizontal deviations

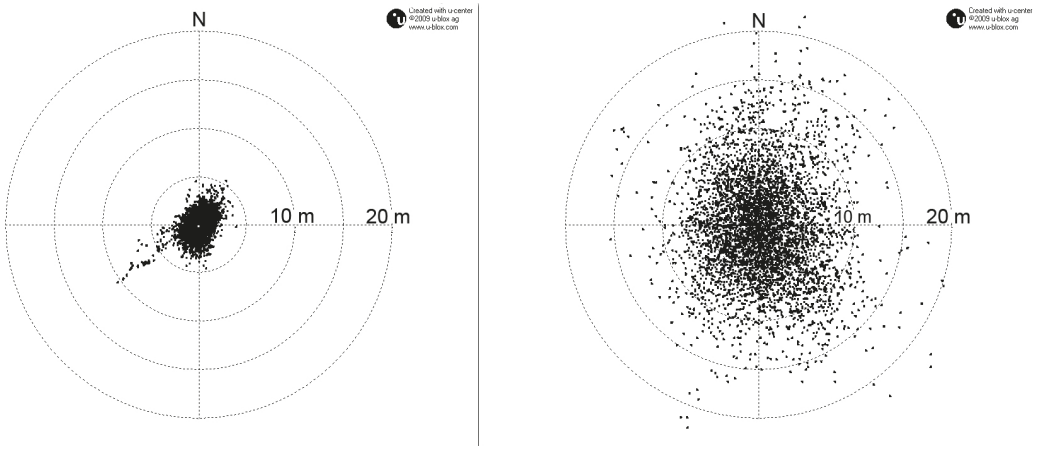

Fig. 1: Comparison of deviation maps of real-time code solutions under open sky on the left and with foliage on the right

of this solution remarkably show that the use of EGNOS and RAIM for blunder detection yields a much better result (i. e., in solution 1). In addition, it can be seen from Table 1 that the results in the coniferous forest are slightly better than in the deciduous and young forest, especially for solution 3.

Furthermore the code SPP solution performance of the receiver in the three different seasons was analysed in more detail. Table 2 shows the results for summer, autumn and winter. The deviations from ground truth of SPP solutions for session lengths of 24 h are given in the Table. In the measurement campaign these sessions were repeated at least twice in all three seasons. Mean horizontal deviations of better than 1 m with a standard deviation of around 8 m are achieved in summer and winter in all three forest types. In autumn, however, the mean horizontal deviations are around 2 m in deciduous and young forest. In the coniferous forest they are 1.1 m. Thus these results indicate that dry leaves cause a higher reduction in positioning accuracy than freshly soaked leaves. As expected, the deviations in height are much larger and the reach over 15 m in the deciduous forest, again in autumn.

4. Differential carrier phase solutions

In this section the results of the L1 carrier phase measurements are discussed. Due to the attenuation and delay by the foliage the carrier phase observations are heavily biased. In the paper we use the term 'phase solution' if all ambiguities can be fixed as integers. If ambiguities cannot be fixed to integers a 'float solution', or if no ambiguities could be fixed a 'code solution' is obtained. This differentiation is an effective way to evaluate the performance and the improvement achieved for measurements under forest canopy, because all three solutions show different behaviour patterns. Due to immense influence of the canopy baseline solutions under high canopy are even worse than the code solutions presented in chapter 3. Table 3 shows a comparison of mean, standard deviation, median and interquartile range (IQR) of the horizontal deviations from ground truth for static baseline solutions in 3 h observation windows over two days. An immense difference in mean and median (which is the largest in deciduous forests) indicates a large number of outliers. Table 4 shows a comparison of horizontal and vertical deviations exemplarily in summer with varying session lengths from 15 minutes up to

Forest type	Horizontal mean and standard deviations in [m]					
	Solution 1		*Solution 2*		*Solution 3*	
Deciduous	0.66	8.31	0.71	2.99	2.27	3.21
Coniferous	0.41	7.90	0.33	2.13	0.53	3.11
Young	0.86	7.45	0.98	3.20	2.58	5.80

Tab. 1: Comparison of horizontal mean deviations from ground truth and their standard deviations in [m] of three different code solutions

Summer	Deciduous		Coniferous		Young	
	horiz.	*vert.*	*horiz.*	*vert.*	*horiz.*	*vert.*
Mean	0.66	12.91	0.42	11.45	0.87	4.38
Std. dev.	8.31	10.19	7.90	9.39	7.45	8.24

Autumn	Deciduous		Coniferous		Young	
	horiz.	*vert.*	*horiz.*	*vert.*	*horiz.*	*vert.*
Mean	1.97	15.80	1.09	13.82	2.23	8.34
Std. dev.	7.54	8.81	7.13	8.19	7.42	7.78

Winter	Deciduous		Coniferous		Young	
	horiz.	*vert.*	*horiz.*	*vert.*	*horiz.*	*vert.*
Mean	0.18	14.07	0.58	8.98	0.65	4.82
Std. dev.	7.38	8.93	5.95	7.19	5.27	5.99

Tab. 2: Comparison of mean horizontal and vertical deviations and their standard deviations in [m] in three different seasons over 24 h session lengths

Forest type	Mean / Std. dev.	Median / IQR		
Deciduous	16.61	72.67	0.74	8.06
Coniferous	8.91	49.93	0.46	5.05
Young	0.50	2.98	0.03	0.91

Tab. 3: Comparison of mean, standard deviation, median and interquartile range (IQR) of horizontal deviations in [m] for static baseline solutions in 3 h observation windows

Summer	15 min.		30 min		1 h		2 h		3 h		6 h	
	horiz.	*vert.*	*horiz.*	*vert.*	*horiz.*	*vert.*	*horiz.*	*vert.*	*horiz.*	*vert.*	*horiz.*	*vert.*
Mean	1.06	12.19	3.50	–7.43	2.29	1.32	3.36	–15.96	3.77	–11.55	2.63	6.39
Std. dev.	254.42	471.44	148.97	345.83	39.11	164.32	43.92	208.70	53.23	254.37	31.44	41.71
Median	0.16	1.77	0.14	1.54	0.07	1.52	0.07	1.33	0.02	1.12	0.03	1.07
IQR	4.32	6.13	4.67	6.03	4.97	6.28	4.93	4.63	3.49	5.68	4.02	4.28

Tab. 4: Comparison of mean, standard deviation, median and interquartile range (IQR) of horizontal and vertical deviations in [m] in summer with varying session lengths

6 h in all forest types. As can be seen, many outliers cause high standard deviations and they are not normally distributed. Median and IQR, on the other hand, show that a high positioning accuracy can be achieved if outliers are eliminated. The percentage of phase, float and code solutions over different observation times can be seen in Figure 2. Focusing on the percentage of phase solutions in deciduous and coniferous forests, the percentage reaches its maximum after two to three hours at around 12 %. Float solutions are dominant and nearly no code solutions occur. In young forests the number of phase solutions increases with the length of observation time and nearly all ambiguities can be solved in observations over 24 h.

Further analyses of phase and float solutions are shown in Figure 3. Here standard deviations and IQR are compared in the three forest types over different observations windows from 15 minutes up to 6 h. The cause for high standard deviations in the float solutions are the large number of outliers. When looking at the IQR it can be seen that robust filters can reduce this influence significantly by eliminating the outliers.

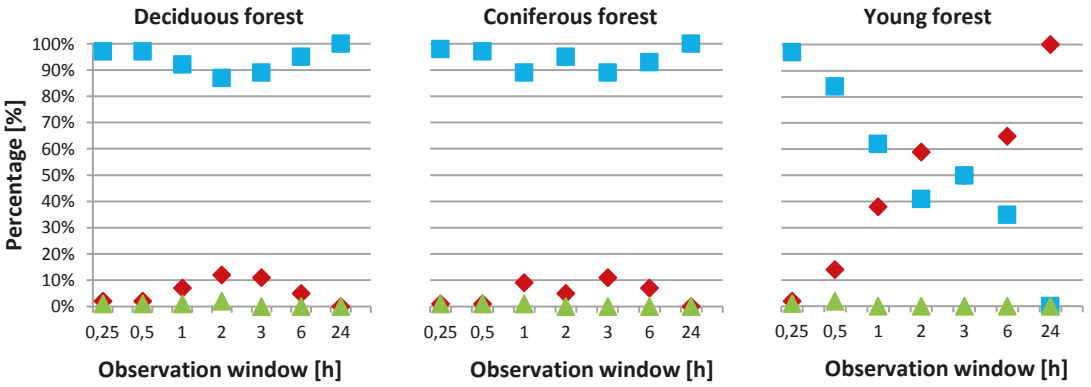

Fig. 2: Comparison of the percentage of phase (red), float (blue) and code (green) solutions over different observation time lengths in the three forest types

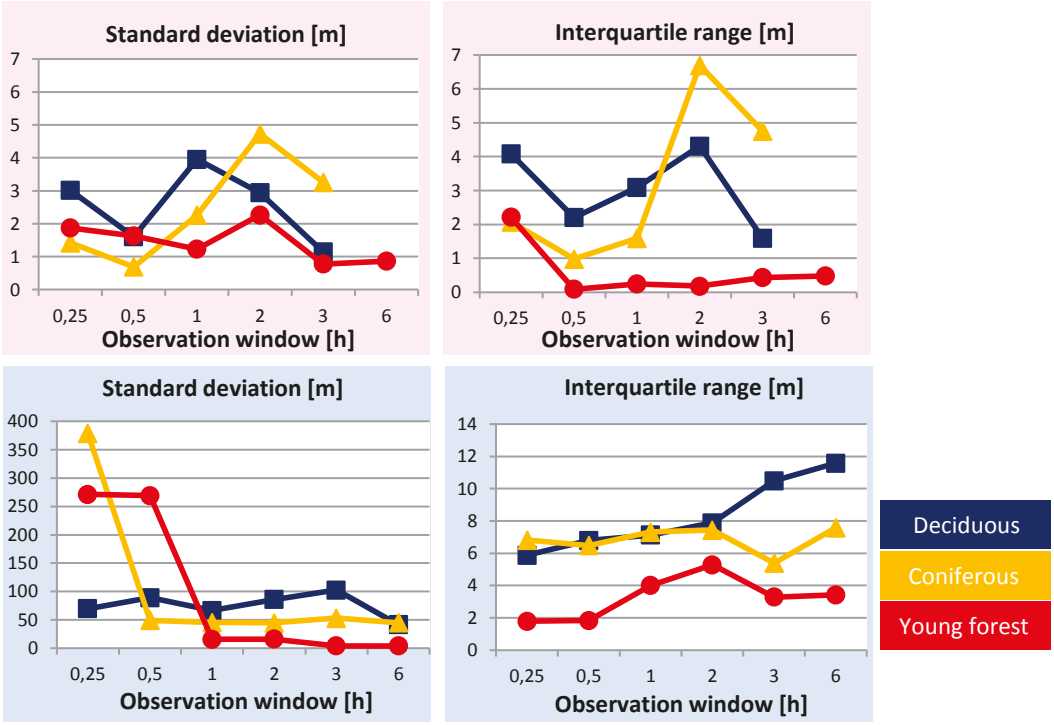

Fig. 3: Comparison of standard deviations and IQR of horizontal deviations of phase (top) and float solutions (below) in [m] in dependence of the observation time length [h]

By evaluating seasonal trends of the phase, float and code solutions it can be recognized that positioning results in summer with moist foliage are better than in autumn when the foliage is dry. As expected, in winter the performance is best. One of these indicators is the percentage of phase solutions which is presented in Figure 4 over different observations windows from 15 minutes up to 6 h. In the longer observation windows it can clearly be seen that in autumn the number of phase solutions is lower than in the other two seasons. For observation windows of longer than 2 h the number of phase solutions reaches around 25 % in summer and up to 30 % in winter. In deciduous and coniferous forests float solutions are usually obtained. These are

highly affected by outliers caused by biased carrier phase observations. This analysis also shows that the number of phase solutions is lowest in deciduous and the highest in young forest. As an example the IQR of the phase and float solutions for the deciduous forest over the three different seasons with varying observation windows ranging from 15 minutes up to 6 h is shown in Figure 5. The IQR of the float solutions is very similar in all seasons whereas the phase solutions vary significantly, but on a lower level. In winter the lowest IQR for the phase solution of less than 1 m occurs for observation windows of 6 h.

5. Statistical analysis of raw data

In the following, a statistical analysis of raw data is presented and discussed. For post processing RINEX files of raw observations were used. The loss-of-lock indicator (LLI) in these files describes if a loss of the carrier phase ambiguity occurred and a new unknown ambiguity has to be introduced and solved for. In case of dual frequency receivers LLI-flags indicate not only if the phase ambiguity is lost, but also if a change of the wavelength factor occurred. For single frequency receivers, however, this distinction is not possible. In the following analysis the LLI flags

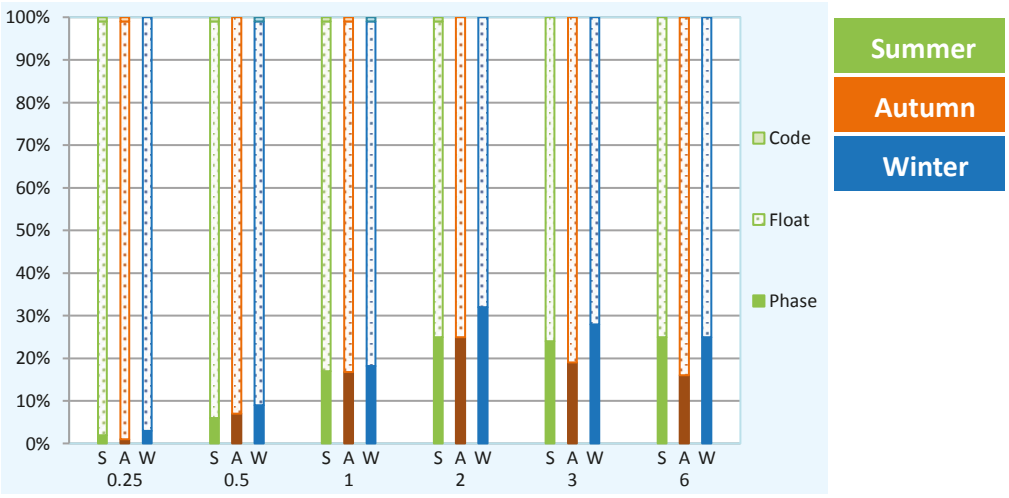

Fig. 4: Comparison of percentage of phase-, float-, and code solutions in summer, autumn and winter depending on the observation time length [h] averaged over all forest types

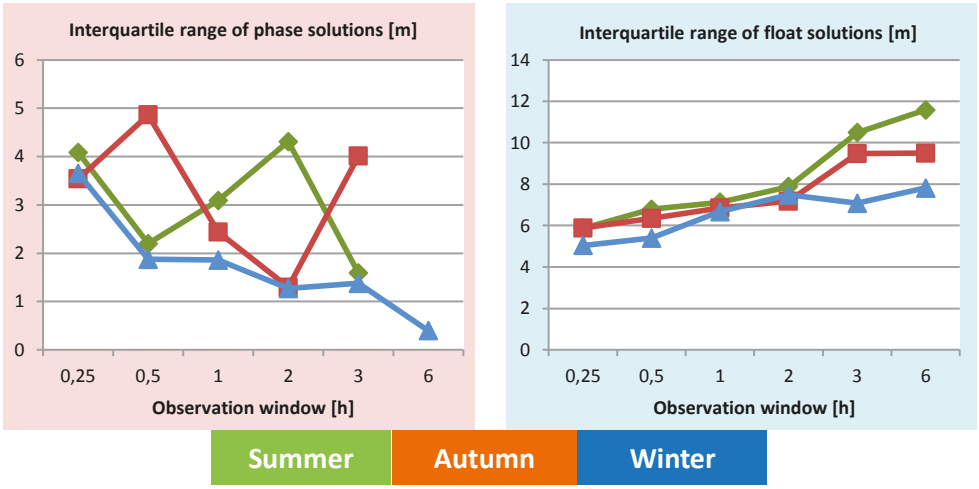

Fig. 5: Comparison of IQR of phase and float solutions in [m] in the deciduous forest in dependent on observation time length [h]

were only regarded as an indication if a loss of the ambiguities occurred or not. Hence it is distinguished between two cases, i. e., one with and the other without LLI flags in the RINEX raw data file. Figure 6 depicts histograms of the carrier-to-noise density ratio C/N_0 distribution showing the magnitude of the signal strength. The percentage of LLI flags corresponds to the dominating signal quality. Looking at the distribution of observations (blue distribution) it can be seen that this distribution can be split into two sub-quantities, i. e., unaffected signals without LLI (green distribution) and affected signals with LLI flags (red distribution). Reference observations under open sky conditions showed that most observations have a C/N_0 ratio of above 35 dBHz. In contrast to these observations the number of observations with LLI flags increases to 43 % in forests and the mean of the C/N_0 ratio of all observations decreases from 42.16 to 34.80 dBHz. For the observations without LLI flags it decreases to 40.67 dBHz whereas the mean of the observations with LLI flags increases slightly. This means that the signal-to-noise ratio is weaker in forests than under open sky conditions which can be compensated only partially when employing HS-GPS receivers. But the observations with LLI flags show a significant rise between 20 and 40 dB which most likely causes the high scattering of the position estimates (compare Figure 1). Furthermore it was investigated if there are major differences depending on the type of forest. The results showed that there are no significant differences in high forest (i. e., deciduous and coniferous) in which about half of the satellite observations are flagged with LLI flags. In the young forest the number of observations with LLI flags is significantly lower, it is at around 30 %. When analyzing the observations in dependence of the season it could be seen that the number of observations without LLI flags is higher in winter than in the other two seasons. To summarize it can be said that the signal-to-noise ratio is 4 dBHz lower in forests than under open sky.

6. Conclusions and outlook

The aim of this study was to investigate the performance of HS-GPS receivers in forests. Measurement campaigns in three different seasons with long-term static observations of 24 h periods were repeatedly performed at each of ten selected survey points serving as ground truth. The coordinates of these test points were obtained from conventional surveying with traversing using a total station with a standard deviation of 1 cm. They are located in deciduous, coniferous and young forests with tree heights ranging from 5 to 20 m. The results were compared according to the forest type and season to the absolute coordinates of the survey points. Code SPP solutions using broadcast and precise ephemeris as well as EGNOS corrections and differential carrier phase baseline solutions to a virtual reference station in the Austrian CORS

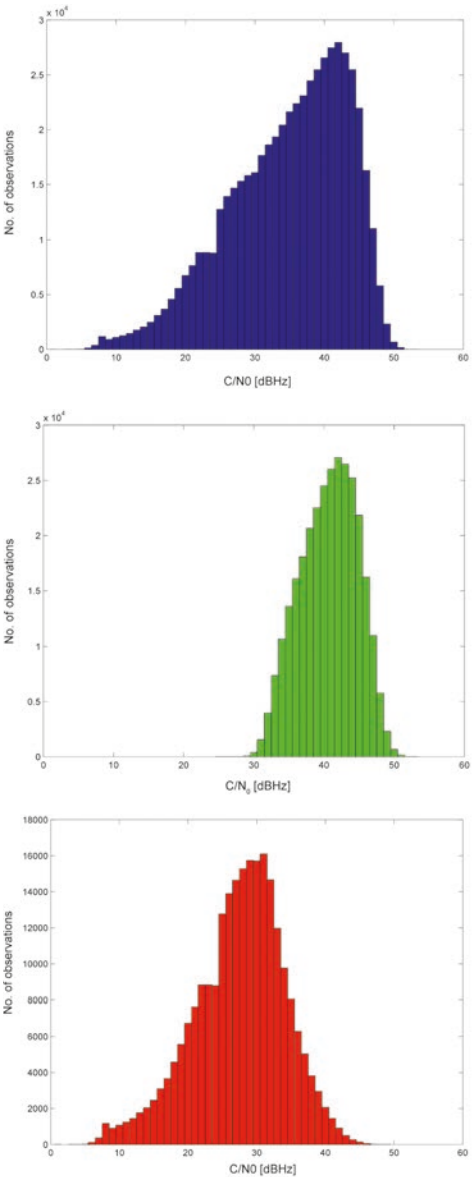

Fig. 6: Histograms of C/N0 ratio distribution for the whole observations (blue), without LLI (green) and with LLI (red) flags of the summer campaign

network EPOSA were processed and analyzed. The employed receiver generally performed well as no complete failures were detected.

For static code SPP the mean horizontal deviations on the ten survey points from the ground truth ranged from few dm up to 1 m with a standard deviation of around 8 m in summer and winter depending on the length of the observation time. In autumn, however, the mean horizontal deviations increased to around 2 m. Reasons for this could be the fact that dry leaves cause a higher reduction in positioning accuracy than freshly soaked leaves. Further investigation regarding this matter has to be carried out. By analyzing the observations depending on the kind of canopy, it could be seen that the positioning results under leaves were inferior to the one under coniferous canopy. In addition, the influence of the foliation in the different seasons could be clearly seen as in winter in deciduous forest, for instance, where there were no leaves on the trees the positioning accuracies were significantly better than in summer or autumn. As expected the code SPP solutions using EGNOS corrections and RAIM were significantly better than the one without.

In the case of carrier phase solutions of baselines to a virtual reference station, however, a significant reduction of signal quality occurred. Due to the influence of the foliation the carrier phase information was heavily disturbed. The analysis indicated that up to 50 % of the observations in a 24 h time period were affected by a loss-of-lock. Hence, the results were divided in carrier phase solutions where all ambiguities could be fixed to integers (referred to as phase solutions in the paper) and float solutions where they are no integers. The results indicated that three quarters of all solutions were float solutions and these showed a large number of outliers. A standard deviation of less than 1 m could only be achieved in the case where nearly all ambiguities could be fixed. Robust estimation is an appropriate tool to eliminate the influence of outliers in the observations. Single frequency relative positioning with robust estimation yielded a median of less than 10 cm with an IQR of around 3 m.

The study clearly shows the influence of the type of forest, tree height and foliage as a matter of the season. Code SPP is suitable for applications ranging from navigation of tractors, harvesters and forest machines to the determination of the size of agricultural land for European Union funding. On the other hand, static differential positioning is usable for applications such as mapping and forest classification, depending on a careful selection of the suitable observation time length and analysis method. In such applications extreme care has to be undertaken to achieve acceptable results.

In this study an investigation of the performance of a certain HS-GPS receiver was conducted. Further investigations and analyses will concentrate on the use of other different geodetic and navigation type receivers and antennas. Particularly with regard to the increasing number of available GNSS satellites the achievable performance, availability and increase in positioning accuracy which goes along with a careful selection and weighting of suitable unbiased satellite signals will be investigated. For single or dual carrier phase observations a first approach is the development of a sound algorithm for a careful selection and weighting of satellite signal observations which are marked with LLI flags resulting in a loss of ambiguities in differential positioning.

Acknowledgements

The observation data of the reference station was kindly made available by EPOSA (an Austrian wide CORS network, see http://www.eposa.at/). The test area was provided by ÖBF, the federal Austrian forest agency (see http://www.oebf.at). We thank both for their support and assistance.

References

[1] *Lachapelle, G., Kuusniemi, H., Dao, D., MacGougan, G. & Cannon, M.E. (2004)*: HSGPS Signal Analysis and Performance Under Various Indoor Conditions, Navigation, Journal of the U.S. Institute of Navigation, 51(1), 29-43.

[2] *Schwieger, V. (2007)*: High-Sensitivity GPS — the Low Cost Future of GNSS ?!, International Federation of Surveyors FIG, Article of the Month, August 2007, 15 pgs, see http://www.fig.net/pub/monthly_articles/august_2007/august_2007_schwieger.pdf (accessed January 2015).

[3] *Zhang, J., Li, B., Dempster, A. G. & Rizos, C. (2011)*: Evaluation of High Sensitivity GPS Receivers, Coordinates, March 2011, Australia, see http://mycoordinates.org/evaluation-of-high-sensitivity-gps-receivers/ (accessed January 2015).

Contacts

A.o. Univ.-Prof. Dr. Guenther Retscher, Vienna University of Technology, Department of Geodesy and Geoinformation, Engineering Geodesy, Gusshausstraße 27-29, E120-5, 1040 Vienna, Austria.

E-Mail: guenther.retscher@tuwien.ac.at

Dipl.-Ing. Severin Heuböck, Vermessung Schubert, Kremser Landstraße 2, 3100 Sankt Pölten, Austria.

E-Mail: s.heuboeck@gmx.at


Renewal of the Austrian Gravimeter Calibration Line HCL

Diethard Ruess and Christian Ullrich, Wien

Abstract

The Hochkar Calibration Line (HCL) was established 1982 between Goestling/Ybbs to Hochkar and has been used yearly for calibrating relative gravimeters in Austria. The gravity difference of 198.3 mGal (1.983 µm/s²) at this line with only 20 km distance is based mostly on the height dependence of gravity. In 1988 and 1995 the HCL was checked and fixed by absolute gravity measurements using the free fall gravimeter JILAg6. Due to changes (constructions) at the top station Hochkar in 2013 it was necessary to define a new end-point combined with some new secondary points. In 2014 at the still existing absolute stations in Goestling and Hochkar absolute observations were repeated with an absolute gravimeter FG5. The long time observations by several relative gravimeters since 1982 are analysed and combined with the absolute gravity results. The new results show a small gravity change at the top station of approximately –20 µGal in comparison to 1995. The BEV now provides for the users of the HCL an updated and high accurate calibration facility for relative gravimeters.

Keywords: Relative gravimetry, Absolute gravimetry, Calibration, metrology, FG5, Scintrex

Kurzfassung

Die “Hochkar-Eichlinie” – Hochkar Calibration Line (HCL) wurde 1982 zwischen Göstling/Ybbs und dem Hochkar eingerichtet und wird seither jährlich zur Kalibrierung der Relativgravimeter in Österreich verwendet. Die Schweredifferenz von 198.3 mGal (= 1.983 µm/s²) dieser Linie mit bloß 20 km Länge wird hauptsächlich durch die Höhenabhängigkeit der Schwere verursacht. Infolge von Veränderungen (Umbauten) an der oberen Station Hochkar im Jahr 2013 wurde es nötig, den Endpunkt mit einigen neuen Versicherungspunkten neu festzulegen. An den noch vorhandenen Absolutstationen in Göstling und Hochkar wurden die Absolutschweremessungen mit einem Absolutgravimeter FG5 wiederholt. Die über lange Zeit erfolgten Relativmessungen seit 1982 wurden mit den Absolutschweremessungen kombiniert und analysiert. Die neuen Messungen zeigen eine kleine Schwereänderung von etwa –20 µGal an der oberen Station gegenüber 1995. Durch die Aktualisierung steht den Nutzern der HCL weiterhin eine hochgenaue Einrichtung zur Kalibration von Relativgravimetern zur Verfügung.

Schlüsselwörter: Relativgravimeter, Absolutgravimeter, Kalibrieren, Metrologie, FG5, Scintrex

1. Introduction

Austrians gravimeter calibration line was installed 1982 between Goestling/Ybbs and Hochkar in Lower Austria [1]. It’s easily reachable from Vienna in about two hours in a driving distance of 160 km (Figure 1). The top station Hochkar gave the name: “Hochkar Calibration Line – HCL”. Since that time the HCL was frequently used for checking and calibrating relative gravimeters. The total gravity difference of about 200 mGal between the end points is mostly based on the height dependence of gravity. This gravity difference covers the measuring range of the two LCR[1)]-D relative gravimeters which were mostly used at the IMG-UW[2)] and the BEV[3)] for a very high number of gravity observations in Austria. Moreover the HCL is used for all other used relative gravimeters. The calibration line consists of four main stations. That enables to check also the non linearity of gravimeter factors which strongly occurs by LCR meters [2]. The time needed to access these sites successive by car is less than 30 minutes at a distance of 20 km. Therefore a fast and economic procedure for calibrating improves the quality of drift determinations. Nevertheless the total height difference of about 950 m of the HCL affects the measurement uncertainty of the results due to air pressure effects and consequential a hysteresis behaviour of the LCR meters.

1) LCR gravimeters manufactured by LaCoste&Romberg

2) Institute of Meteorology and Geophysics, University of Vienna; http://img.univie.ac.at/

3) Bundesamt für Eich und Vermessungswesen (Federal Office of Metrology and Surveying); www.bev.gv.at

2. Reference frame / datum

In the beginning the gravity stations were determined by 3 LCR gravimeters which were calibrated by using the results of the Austrian

Site	Station nb.	φ	λ	Height [m]	geology
Goestling	S1-071-00	47°48.49'	14°56.16'	528,9	Alluvial gravel
Lassing	S1-101-10	47°44.82'	14°54.06'	684,8	Alluvial gravel
Aiblboden	S1-101-20	47°44.10'	14°54.56'	1115,9	Limestone
Hochkar	S1-101-37	47°43.14'	14°55.04'	1489,8	Limestone, dolomite

Tab. 1: Main gravity stations at the Hochkar Calibration Line – HCL

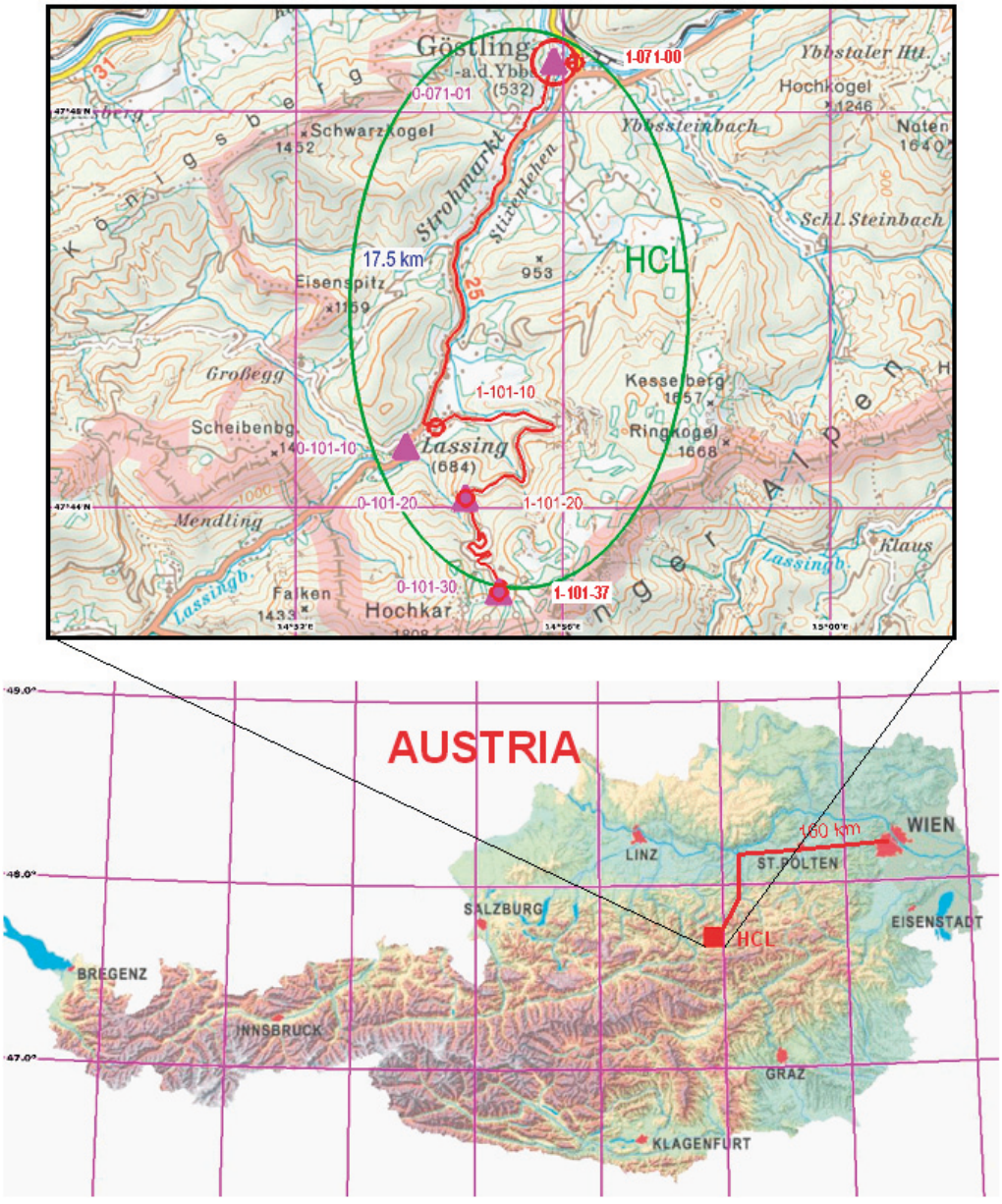

Fig. 1: Situation of HCL in Austria

Fig. 2: Lower station Goestling – Nepomuk S1-071-00

Gravity Base Network that was adjusted by six absolute gravity stations [1].

In 1988 close to the two end points of the HCL absolute gravity stations were founded and observed with the JILAg-6 free fall absolute gravimeter of Austria. In 1995 the absolute gravity measurements were repeated at the end points and supplemented by observations close to the waypoints (intermediate sites) Lassing and Aiblboden [3]. In Goestling the former station in the church-tower was no longer suitable for sensible free fall absolute observations, therefore

Fig. 3: Upper station Hochkar S1-101-37

a new station was founded near by in the cellar of the school building and tied to the former site by relative gravimeters. The comparisons of the results of the two observations epochs do not show significant differences at the repeated sites (Table 2). The given difference of 429 µGal is the result of the network adjustment using about 40 ties.

Additionally during the 1995 campaign vertical gradient measurements were performed at all stations (absolute and relative sites) and a microgravity network was established including all the sites of the HCL (Table 3).

3. Relative gravity observations

Since 1982 a very high number of gravity measurements (132) were taken for calibrating the relative gravimeters. Nevertheless the results in Figure 4 show quite large differences between the instruments. The red line gives the average value respectively the nominal difference value. The nominal difference value corresponds to the directly measured connections from the HCL end points to the absolute stations. The average value is calculated using all relative gravity measurements between the end points of the HCL. Both values fit to 0.8 µGal. The maximum scatter of the measured differences between the main points

Goestling-Nepumuk and Hochkar amounts 97 µGal which is 0.05 % of the total difference. The big scatter of the relative gravimeter results may be caused by not exactly compensated pressure influence of the LCR-meters which also show quite large hysteresis effects at the two waypoints dependent from the direction of driving whether you come down or up [2]. This graph gives also an impression of measurement uncertainties of the relative gravimeters which may occur during normal field observations. Using Scintrex CG5 relative gravimeters since 2007 show an improvement of the results. A very high attention has to be paid to the vertical gradients of gravity at the different stations. This is necessary, if the sensors of the different used relative gravimeters are in different positions above the benchmarks. Particularly the sensors of Scintrex gravimeters are located ~20 cm higher than those of the LCR gravimeters. Table 3 shows the different gradients at the stations. The scatter amounts 175 µGal/m. Negating the effect of gradients

Site	Station	1988	1995	2014
Goestling church-tower absolute station	0-071-00	980 681 839 ± 5	980 681 843 ± 4 (relative deduction)	980 681 844 ± 8 (relative deduction)
Relative tie (school – tower)			429 ± 3	429 ± 3
Goestling school (absolute)	0-071-01	—	980 682 272 ± 3	980 682 273 ± 7
Hochkar absolute station	0-101-00	980 484 648 ± 5	980 484 647 ± 5	980 484 626 ± 5

Tab. 2: Comparison of repeated absolute gravity observations at the HCL (1988/1995) values in µGal (=10 nm/s²)

Site	Station	Order	VG [µGal/m]
Goestling church-tower	0-071-00	Absolute I	235 ± 4
Goestling school	0-071-01	Absolute II	183 ± 5
Goestling Nepomuk	1-071-00	Main HCL point	282 ± 6
Goestling church	1-071-01	Secondary HCL point	250 ± 6
Lassing Maut	1-101-10	Main HCL waypoint	258 ± 7
Aiblboden	1-101-20	Main HCL waypoint	333 ± 7
Hochkar JUFA outside	1-101-37	Main HCL point	357 ± 7
Hochkar JUFA inside	0-101-30	Absolute	356 ± 4

Tab. 3: Different vertical gravity gradients at different stations

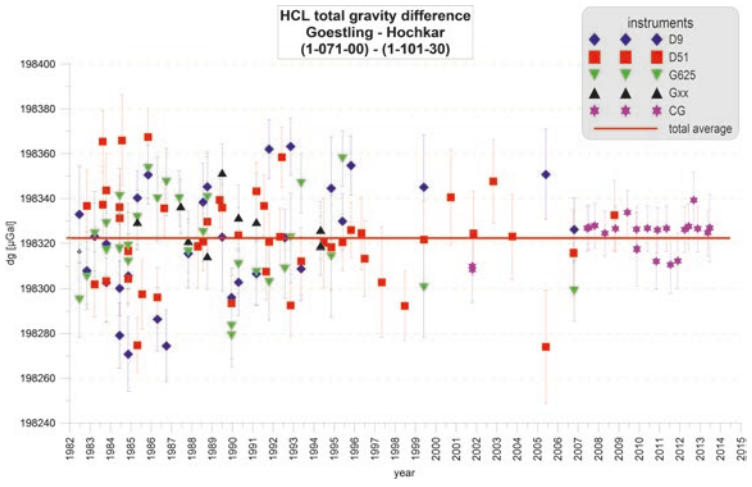

Fig. 4: Relative gravimeter measurement scatter at the HCL before calibration

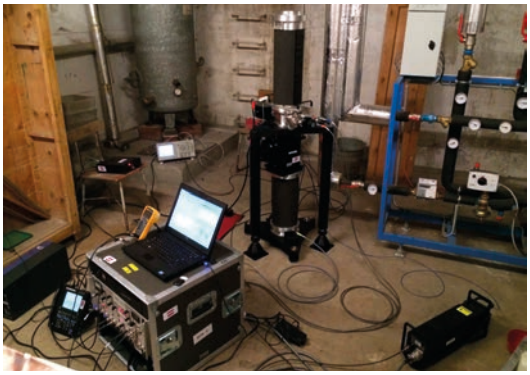

Fig. 5: FG5 absolute gravimeter at the absolute gravity station Goestling

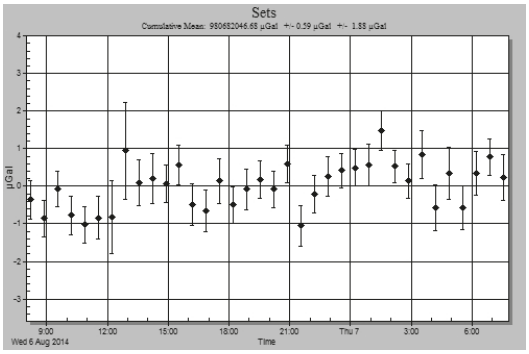

Fig. 6: Set results of FG5-242 at Goestling 2014

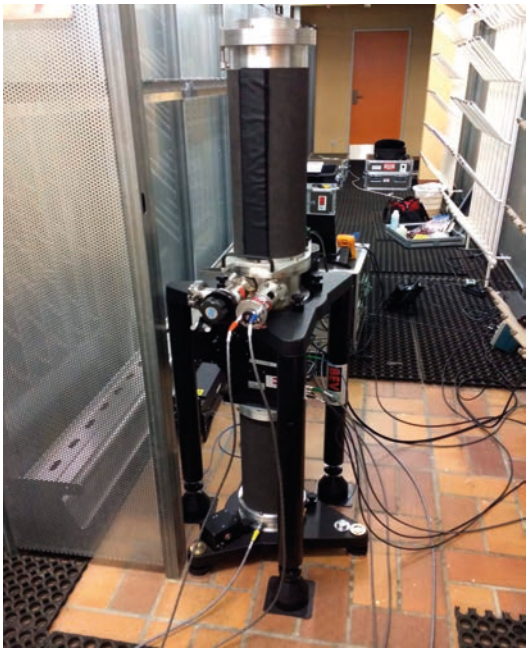

Fig. 7: Absolute station Hochkar 2014

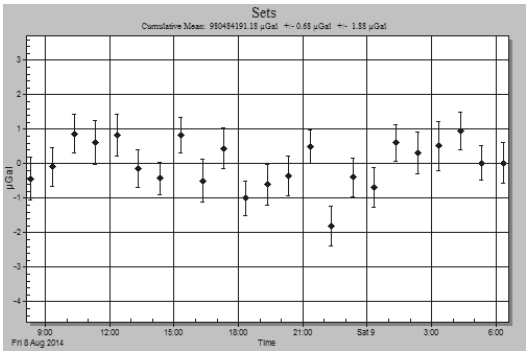

Fig. 8: Set results at Hochkar 2014

may cause errors in the results in order of more than 30 µGal for the gravity differences between certain stations.

4. Absolute gravity measurements 2014

In August 2014 new absolute gravity measurements were performed at the HCL with the absolute gravimeter FG5-242 which is also used as the Austrian national metrological standard for the earth acceleration. The use of the FG5 absolute gravimeter improves the measurement uncertainty greatly compared with the former used JILAg instrument. The measurement uncertainty now varies around 2.5 µGal (1 µGal $= 10^{-8}$ m/s^2). Both used absolute gravimeters were validated regularly by international absolute gravimeter comparisons every 4 years at least [4, 5, 6].

Due to the changes caused by construction at the top station Hochkar it was necessary to repeat the absolute gravity observations there. So it was also opportune to repeat the observation at the bottom station Goestling-school. Because of the unfavorable locations of the absolute stations of the waypoints their re-measurements were waived.

Usually in practice the relative gravimeter observations for calibrations are made at the main HCL stations (Goestling-Nepomuk, Lassing-Maut, Aiblboden, Hochkar-JUFA) and not at the absolute points. The reason is primary the more complicated accessibility of the inside stations which would cause much more time. The relative gravity connections between the absolute stations and the HCL calibration points were repeated several times over the years.

4.1 Absolute station Goestling

The absolute measurements at Goestling were performed in the cellar of the primary school

			differences [µGal]			
Site	*station*	*g [µGal]*	*1-071-01*	*1-101-10*	*1-101-20*	*1-101-37*
Goestling Nepomuk	1-071-00	980683147	1228	41152	126880	198356
Goestling church	1-071-01	980681919	0	39924	125652	197128
Lassing Maut	1-101-10	980641995		0	85728	157204
Aiblboden	1-101-20	980556267			0	71476
Hochkar JUFA	1-101-37	980484791				0

Tab. 4: New gravity values of the HCL at the benchmarks main stations for relative gravimeters

(Figure 5) and lasted 24 hours (Figure 6). Around 3500 free fall drops were used for the final gravity value. The result at the reference benchmark coincides with the former measurements in the level of about 2 µGal (Table 1). The measurement uncertainty of the observation 2014 amounts 2.4 µGal. The set gravity values are shown in Figure 6. Their scatter is clearly below 2 µGal.

4.2 Absolute station Hochkar

The absolute measurements at Hochkar were performed in the JUFA Hotel in the ski storage room (Figure 7). The measurements lasted over two days. About 3500 drops were used for calculating the absolute gravity value. The new result differs about 21 µGal from the former measurement results. That means that the value at the absolute gravity station at Hochkar is 21 µGal less than the old values of 1988 and 1995. The reason of this gravity decrease could be explained by earthmoving through renovation of the buildings respective the near surrounding.

5. HCL results

The new values of the HCL for relative gravimeter positions are calculated using all suitable gravity differences and absolute observations by network adjustment (Table 4). The measurement uncertainty of the results is 3 µGal at one sigma level due to this adjustment. Detailed descriptions of the stations are available at the BEV in Vienna.

6. Conclusion

The Hochkar Gravimeter Calibration Line HCL is a very important facility in Austria for checking and calibrating relative gravimeters. This Line is used since 1982 periodically by domestic gravimeters as well as by foreign gravimeters. The HCL itself is checked by absolute gravity observations on the one hand; on the other hand it can be checked recursively using the results of the relative gravity measurements. The results of the relative measurements show unfortunately a large scatter. Nevertheless the combination of absolute and a high number of relative measurements give quite good gravity values at the main stations. It is also necessary to observe the surrounding of the stations if there may be an influence on the gravity value caused by constructions and mass movements. Therefore absolute observations have to be repeated from time to time.

References

[1] *Meurers B., Ruess, D., 1985*: Errichtung einer neuen Gravimeter - Eichlinie am Hochkar. ÖZV 1985/3, 175-183, Vienna.

[2] *Meurers, B., Ruess, D., 2000*: Gravity Measurements at the Hochkar Calibration Line (HCL). Proceed. 8. intern. meeting on Alpine Gravimetry. Österr. Beitr. Met. Geoph., 26, 209-216, ZAMG, Vienna 2001.

[3] *Ruess, D., 2001*: Absolute Schweremessungen in Österreich seit 1987. Die Zentralanstalt für Meteorologie und Geodynamik 1851 - 2001, 150 Jahre Meteorologie und Geophysik in Österreich, 590 – 607, Leykam, Graz 2001, ISBN 3-7011-7437-7.

[4] *Marson I., et. Al., 1995*: Fourth International Comparison of Absolute Gravimeters. Metrologia, Vol. 32, Nb. 3, BIPM, Nov. 1995.

[5] *Ruess, D., Ullrich, Ch., 2011*: 20 years of International Comparisons of Absolute Gravimeters (ICAG) at the Bureau International des Poids et Mesures (BIPM) in Paris with Participation of BEV. Austrian Contributions to the XXV General Assembly of the IUGG. VGI 2/2011, P. 154 – 161, Vienna

[6] *Z Jiang, et al., 2012*: The 8th International Comparison of Absolute Gravimeters 2009: the first Key Comparison (CCM.G-K1) in the field of absolute gravimetry. Metrologia 49, 666-684.

Contacts

Dr. Diethard Ruess, BEV – Federal Office of Metrology and Surveying, Department Control Survey, Head of V11 – Geophysics and Precise Levelling, Schiffamtsgasse 1-3, 1020 Vienna, Austria.
E-Mail: diethard.ruess@bev.gv.at

Mag. Christian Ullrich, BEV – Federal Office of Metrology and Surveying, Department Control Survey, V11 – Geophysics and Precise Levelling, Schiffamtsgasse 1-3, 1020 Vienna, Austria.
E-Mail: christian.ullrich@bev.gv.at

Vermessung & Geoinformation 2+3/2015, P. 188 – 197, 8 Figs.


Knot estimation on B-Spline curves

Claudius Schmitt and Hans Neuner, Wien

Abstract

Freeform curves with their possibility to approximate shapes from terrestrial laser scanner point clouds are investigated in this study. We focus on B-spline curves which are able to capture the local behavior of the measured profile. Typically, the only parameter set, treated as unknowns are the control points of the B-Spline. Their location is determined by least squares adjustment. The second parameter set are the knots, usually placed at stable locations and they are part of the basis functions. The approach with fixed number of knots placed at stable locations leads to a linear system. However, it intuitively restricts the B-Spline curve in its flexibility. Hence the residuals of the approximation may still contain systematic effects. Estimating the control points and the locations of the knots at the same time succeeds in full flexibility of B-Splines and optimizes the approximation. The system of equations accrued in this second case is highly non-linear. Adequate initial values are necessary to solve this system. Furthermore, introducing constraints can enhance the convergent behavior. This paper introduces a new method that allows the estimation of the number of knots as well as their location. The method uses a bottom up approach starting with the minimum number of knots, denoted as Bézier curves, and adding one knot in each iteration step at a particular curve sections (span) until the convergent criterion is reached. The decision to insert a knot and at a specific location, is based on the analysis of the cumulated sums of squared residuals in each existing span. The location, where the additional knot was inserted, is optimized using a Gauß-Markov model with constraints. The improvements are shown by comparing the results obtained in the linear approach with fixed knots and the non-linear case where control points and the knots are treated as unknowns.

Keywords: B-Spline curve, free knots, shape modelling, freeform curve, TLS profile approximation

Kurzfassung

Freiformkurven können zur Approximation von Punktwolken von terrestrischen Laserscannern genutzt werden. Im Speziellen werden in dieser Untersuchung B-Spline Kurven eingesetzt, die je nach Parameterwahl lokale Gegebenheiten in einer globalen Approximation darstellen können. Typischerweise werden bei einer Approximation von B-Splines die Kontrollpunkte in einem linearen Modell geschätzt. Die Knoten sind ein weiterer Parametersatz mithilfe derer die Basisfunktionen erstellt werden. Die gemeinsame Schätzung der Knoten mit den Kontrollpunkten ergibt ein hochgradig nichtlineares Gleichungssystem. Die volle Flexibilität zur lokalen Anpassung wird erst durch die Schätzung beider Parametergruppen erreicht. Zur Stützung des nichtlinearen Gleichungssystems werden Bedingungsgleichungen und verbesserte Näherungswerte eingeführt. Diese Näherungswerte für die Knoten werden mit einer neuen Methode ermittelt. Diese basiert auf den Residuen der linearen Schätzung der Kontrollpunkte, die in Teilbereichen, sogenannter Spans, analysiert werden. Begonnen wird die Approximation mit der Minimalkonfiguration, den Bézier-Kurven, innerhalb derer die Knoten festgelegt sind. Die im neuen Ansatz erzielte Verbesserung wird durch den Vergleich der Ergebnisse aus der Schätzung der Knoten und der Kontrollpunkte demonstriert.

Schlüsselwörter: B-Spline Kurve, Knotenschätzung, Oberflächenmodellierung, Freiformkurve, TLS Profilapproximation

1. Introduction

Surface-based metrology, like terrestrial laser scanning (TLS), needs new surface-based evaluation methods. Taking the workshop suggestions from [1] into account, these evaluation methods are one of the main challenges making the information of 3D point clouds suitable for further processing steps and taking benefits from the redundancy. Freeform curves and surfaces are promising approximation methods to create parameterized curves and surfaces, like shape information for structural-mechanic analysis of built objects [2]. Whereby, the freeform curves are the basis for the freeform surfaces. Past research has shown that the freeform shapes significantly improve the approximation quality, compared to approximations with geometric primitives, e. g. [2].

In this paper, B-Spline curves are used to approximate TLS profiles. In the past, only the control points of the B-Spline were estimated. Another essential parameter set for B-splines are the knots. The optimization of the knot-locations leads to a nonlinear system of equations. The solution of the non-linear problem as well as the determination of proper initial values for the knot positions is a challenge for which an innovative solution is presented in this paper.

The paper is structured as follows: aspects of B-Spline-curve theory are outlined in the 2nd chapter; the state of the art of curve approximation is presented in chapter 3. Chapter 4 introduces an example that motivates the necessity for knot estimation. The main concepts of the developed method for estimating the number of knots and their locations are described in chapter 5. Performance analysis and the validation of the method is done in chapter 6.1 for simulated data and in chapter 6.2 for real data.

2. B-Spline curves

For the spatial approximation of the TLS 2D profile, B-Spline curves are used. They were proposed by de Boor and de Casteljau [3], [4] and applied especially in CAD designs and construction of cars. The challenge in this paper is to use them in the opposite way, for approximating existing curves and surfaces, based on single points. The advantage of the B-Splines is their flexibility in matching most of the curves with respect to their local behavior.

The local behavior is due to the piecewise linear independent basis function, $N_{i,p}$, with its recursive definition:

$$N_{i,0}\left(obs_{Par.}\right)=\begin{cases}1 & if\ \ u_i < obs_{Par.} > u_{i+1}\\ 0 & otherwise\end{cases}, \quad (2.1)$$

$$N_{i,p}\left(obs_{Par.}\right)=\frac{obs_{Par.}-u_i}{u_{i+p}-u_i}N_{i,p-1}\left(obs_{Par.}\right)+ \\ +\frac{u_{i+p+1}-obs_{Par.}}{u_{i+p+1}-u_{i+1}}N_{i+1,p-1}\left(obs_{Par.}\right), \quad (2.2)$$

$$i = 0, \dots, n, \quad \text{with } U=\{u_0, \dots, u_m\} \text{ and} \quad (2.3)$$

$$m = n + p + 1, \quad (2.4)$$

where n is the number of basis functions and their corresponding control points. For further information on the recursive definition see [5]. The basis function, consists of divided differences of the knots u, with $m+1$ knots inside the knot vector U, and the parameterized observations, $obs_{Par.}$, explained in chapter 3. The variable p, with $p>0$, defines on the one hand the degree of the single basis function and on the other hand the number of linear combined basis functions. The local behavior of the curve is controlled by the distance between the knots. The smaller the spans the more curvature changes / details can be modeled.

Further parameters of the B-Splines are the control points, $CP_{X/Y}$, which can be stated as weights for each basis function $N_{i,p}$

$$C_{X/Y}\left(obs_{Par.}\right)=\sum_{i=0}^{n}N_{i,p}\left(obs_{Par.}\right) * CP_{X/Y,i}\ , \quad (2.5)$$

where $C_{X/Y}$ is the curve point at the 2D Euclidian space (X, Y) with the homologues curve position $obs_{Par.}$ at the parameter space. For clarity reasons we restrict to the 2D case, the extension to the 3D case is a formal analogy. The geometric continuities depends on the span width and can be restricted if necessary.

3. State of the art in B-Spline curve approximation

B-Spline curve approximation from 2D TLS profiles is a new field in engineering geodesy that refers to the deformation analyses, as shown in [6], [7].The characteristic of a TLS point cloud is normally its high point density and its homogeneous distributed points without gaps.

The standard method for the parameterization of the observations from the metrology, $obs_{X/Y}$ (measured 2D coordinates), is denoted as uniform, where the homologous parameters, $obs_{Par.}$, are equal allocated along the curve. However, this is mostly not the case for measured data. A second method based on the chord length between the $obs_{X/Y}$. It roughly approximates the arc length of the curve. A third one is the centripetal method, which contains the centripetal acceleration and curvature. Lee describes in [8] all three methods in detail, compares them to each other and gives recommendations for deploying them, seen in [9].

The control points are estimated by solving the linear system of equations (2.5). The degree of the basis functions is set empirically to a fix value in accordance to the experience about the observations, the further applications and the requirements to the curve continuity.

The last parameters are the knots, which are necessary for the formulation of the basis functions (2.2). There are two estimation issues referring to the knots: their number and their location inside the knot vector. The last is the most complex one. For the number of knots, the Akaike information criterion, AIC, provides promising results, shown in [7], [10] and [11]. Regarding the location of the knots the uniform distribution performs poorly on heavy irregular curved data sets. For this fact other algorithms perform better. They depend on the distribution of the observations, like the basic method described in [5] and its extended version in [12] by considering the Schoenberg-Whitney condition [13]. A further algorithm is the section midpoint strategy, which locates a new knot in the middle of a span, or at the location with the highest residual to an estimated curve. Other techniques uses a initial length and curvature for the knot placement, e. g. [14], [15]. Calculating initial length and curvature on noisy data is a challenge, but produces sufficient knot locations when reliable parameters (curvature and length) can be calculated. Estimating the location of the knots during the approximation leads to a highly nonlinear optimization problem as mentioned before, which is denoted as the "lethargy", extensively explained in [16]. The motivation of optimizing the knot location despite the lethargy is described in the following chapter.

4. Motivation of the knot optimization

Shown in chapter 3, B-Splines consist of two parameter sets which can be estimated during an approximation. Previous research has shown that the estimation of only one parameter set, the control points, in the linear system may lead to systematic effects in the residuals. Increasing the number of knots increases the number of control points with their connectedness of (2.4) and creates significantly better results, e. g. Figure 1 and [7]. Not only the number of knots improve the approximation results but also their location. Its effect is shown exemplary in the following figure.

Figure 1a shows a section of an under determined approximation result created from the sample Dataset of chapter 6.2. Improving the approximation can be done by increasing the number of knots at specific locations, shown in Figure 1b and 1c. Figure 1d, 1e and 1f show the knot locations inside the knot vector for the curves above. Knots with the same value are printed one below the other. The impact of only one additional knot, seen in Figure 1d at location −4.3, results in highly changes of the curvature shape. The reason for the changes is given by the functional relationship between the knots and their basis functions, seen in from (2.2). The additional knot does not only extend the functional system with one basis function it changes the p ascending basis function, counted from the ad-

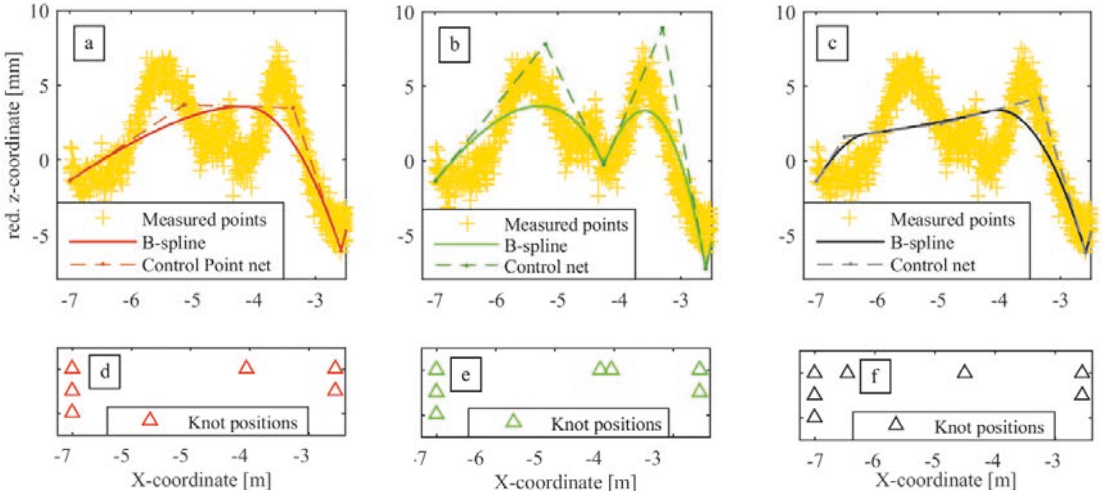

Fig. 1: a) Example of an underdetermined B-Spline approximation; b) Example of an underdetermined B-Spline approximation with one additional knot; c) Example of an underdetermined B-Spline approximation with one additional knot at another location; d) Knot sequence of the curve in a; e) Knot sequence of the curve in b; f) Knot sequence of the curve in c

ditional inserted one. Associated with the knots are the control points, which reinforce or weaken the influence of each basis function, like weights for the observations in a least squares.

The influence of the knot location itself can be seen on the different curves in Figure 1b and 1c. This leads to the fact that the locations of the knots are as important as their number.

5. Implementation

The developed approximation method describes an iterative two-step estimation of the control points and knot locations. For this method, equal observation variances are assumed. The noise assumption ensures that only systematic effects based on the geometry and not on the metrology are optimized and that the numbers of residuals are equally distributed at each span. This is why for now the identity matrix was applied to the stochastic model.

The following flow chart shows the different steps of the method:

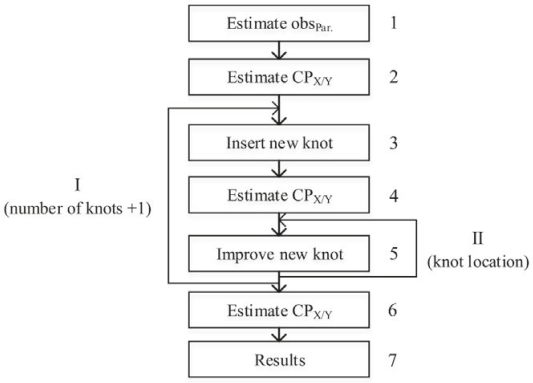

Fig. 2: Algorithm flow chart

In the first step the homologous parameters, $obs_{par.}$, for the measured 2D points, $obs_{X/Y}$, are estimated with one of the methods, uniform or centripetal, appropriated to the datasets as described in chapter 3. In the 2nd step the control points for the minimal configuration of the B-splines, denoted as Bézier curve, with $p+1$ basis functions and a knot vector consisting of

$$U = \{0_0, \ldots .0_p, 1_{p+1}, \ldots ,1_m\}, \qquad (4.1)$$

are estimated using (2.5) in a linear least squares Gauß-Markov model. For the B-Splines used here, the first and last control point fit the first and last observation respectively. These restrictions and the composition of the minimal knot vector implies, that the slope of the line between the first and second control point and between the last and penultimate control point is equal to the slope of the curves at the start and end point. The restrictions are necessary to prevent oscillations of the curve at these points. They are valid for all approximations, which are performed here. If the residuals obtained from the control-point estimation do not fulfil a certain quality criterion, new knots and their locations are estimated iteratively within the loop I (step 3 – 5). In each span cumulative sums (CumSum) of squared residuals are calculated in two versions, first starting from left to right and second starting from right to left. The idea of using the cumulated sums of squared residuals based on equal variances inside each span. Different variance levels indicate systematic effects in the results of the least squares approximation. As shown in chapter 4 the number of knots and their location influences the obtained variance of residuals. Creating a criterion based on the variance, which reduces its value at a specific location inside the approximation, is needed to develop plausible initial values for the knots.

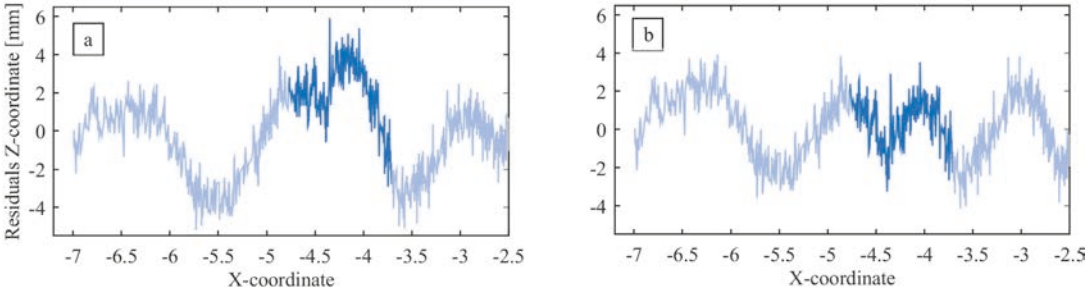

Fig. 3: a) Residuals from approximation shown in Figure 1a; b) Residuals from approximation shown in Figure 1b

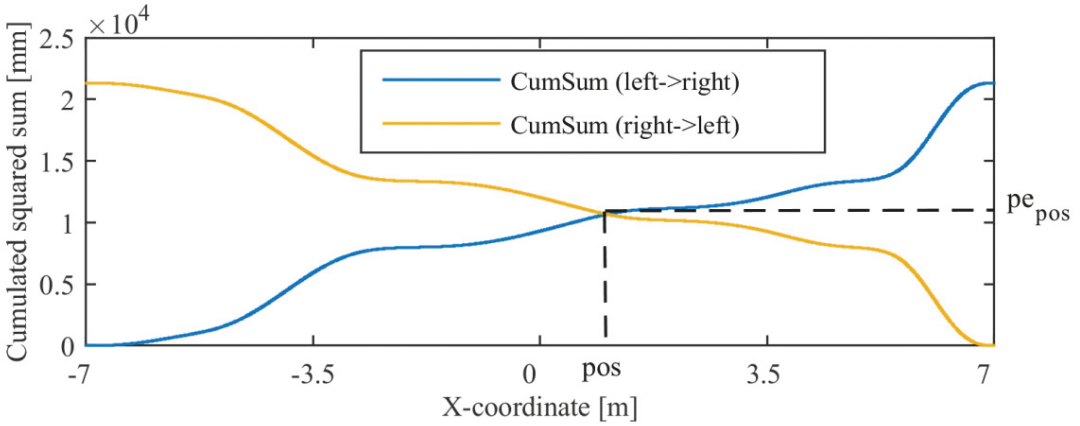

Fig. 4: Cumulated sum of squared residuals (measured data) and their criteria for the new knot locations

These effects can be seen in the residuals, shown in Figure 3, where the additional knot is inserted in the area of –3.7 to –4.7, see Figure 1a and 1b, which corresponds to the section with the highest variance, in this part of the curve. The residuals are reduced by more than the half from ≈5 mm to ≈2 mm at the section mentioned before.

Regarding this concept the squared sum can be understood as the potential energy pe of the residuals inside a span. The position, pos, inside a span where the value of the pe's for both versions of the cumulated squared sum (from left and from right) are equal is defined as the new knot location. Thus, a possible location for a new knot is set equal to the pos in order to reduce the overall pe. At each possible location the value of the cumulative sum at this point is denoted as pe_{pos}, e. g. Figure 4. The new knot will be inserted in the span with the highest pe_{pos} value to reduce the highest pe in the curve.

In each iteration step, only one new knot is inserted. In step 4 the location of the new control points which occurs due to the new knot insertion are estimated with the model (2.5). Afterwards only the location of the new knot is improved by a nonlinear iterative estimation (loop II) using a restricted linearized Gauß-Markov model (step 5). Therefore the location of the new knot is unrestricted while all other knots are fixed by constraints. The Jacobian matrix for this system has the following structure:

$$A = \begin{pmatrix} \frac{\partial C_X\left(obs_{Par.,i}\right)}{\partial u_{p+1}} & \cdots & \frac{\partial C_X\left(obs_{Par.,i}\right)}{\partial u_n} \\ \frac{\partial C_Y\left(obs_{Par.,i}\right)}{\partial u_{p+1}} & \cdots & \frac{\partial C_Y\left(obs_{Par.,i}\right)}{\partial u_n} \\ \vdots & \ddots & \vdots \\ \frac{\partial C_X\left(obs_{Par.,j}\right)}{\partial u_{p+1}} & \cdots & \frac{\partial C_X\left(obs_{Par.,j}\right)}{\partial u_n} \\ \frac{\partial C_Y\left(obs_{Par.,j}\right)}{\partial u_{p+1}} & \cdots & \frac{\partial C_Y\left(obs_{Par.,j}\right)}{\partial u_n} \end{pmatrix}, \quad (4.2)$$

$i = 0, \ldots, j$, $j =$ number of $obs_{par.}$

The derivative for each knot is defined with the recursive algorithms for the basis functions given in (2.2). The parameterization of the observations implies that the $obs_{X/Y}$ provides the full coordinates, here X and Y for the rows, likewise the control points. Due to the orthogonality of the coordinate axes the derivatives of the basis function are the same for each axis.

After the iteration of loop I and II has reached the convergent criterion, based on the results with the simulated data, described later on, the control points are estimated using the optimized new knot location. Then the quality parameters of the results are obtained in step 7. A simultaneous global optimization of the curve parameters, the control points and the knot locations cannot be realized yet due to reasons shown in the next chapter.

Type	Values
Knot vector	{0, 0, 0, 0.10, 0.15, 0.30, 0.55, 0.60, 0.75, 0.90, 1, 1, 1}
Number of knots	13
Number of basis functions / $CP_{X/Y}$	10
Degree	2
Dimension	2 (X,Y)
Noise – Variance	0.005^2
Number of sample points	5000

Tab. 1: B-Spline parameters for simulated data

Method	$\sigma_{apost.}$	T_F	T_F	$F_{9984, 9984, 0.05}$
New method – nonlinear	0.11		1.09	1.03
New method – linear	0.12	1.53		
Basic	0.18			

Tab. 2: Results compared to each other – on simulated data (TF = Test value for the F-test, $F_{f1, f2, 1\text{-}alpha}$ = quantil of the F-distribution)

6. Data Approximation

6.1 Simulated Data

The simulation studies performed in this chapter aim to validate the developed method and to infer its behavior with respect to the knots and control points. Therefore, the test dataset was generated referring to the TLS profile analyzed in chapter 5.2. The noise is processed from the normal distribution with $N(0,\sigma^2 = 0.005^2)$ and used in all simulated data sets. The minimum of 5000 sample points are necessary, because with this number the value σ_{apost}, obtained from the linear approximation in step 2 where the control points are the only unknown, is equal to the value $\sigma_{apriori}$, e. g. Table 1. The sample points are distributed uniformly with a point to point distance of 0.015. The threshold ε to the break criterion of the loop II is set to $\varepsilon = 1e^{-4}$. This value results from the maximum update value for the unknowns of the nonlinear knot estimation in loop II, with the initial values of the control points and knots. The idea is to have the knots and control points as the only unknowns and take the other parameters from the simulated dataset, so that the only influence of changes in the curve geometry relies on them.

Different estimation scenarios were applied on the simulated curve:

- The new method – nonlinear (including loop II, with optimization of knot location in restricted Gauß-Markov model),
- The new method – linear (without loop II, knot location defined according to Figure 4),
- The basic/state of the art method.

also described in Table 2. The degree of the basis function and the number of knots were set equal to the ones of the designed B-Spline. All three above-mentioned methods of parameterization were applied to the $obs_{X/Y}$. A comparison of the obtained results is given in Table 3. For further processing the $obs_{Par.}$ were not improved or recalculated. Instead, they were taken directly from the designed B-Spline.

Results

The Schoenberg-Whitney conditions are fulfilled otherwise the functional matrix of the Gauß-Markov model is singular, which is difficult to solve without further information such as constraints. The linearized normal equation system is badly scaled and needs to be preconditioned to avoid numerical instabilities and to minimize the number of iterations.

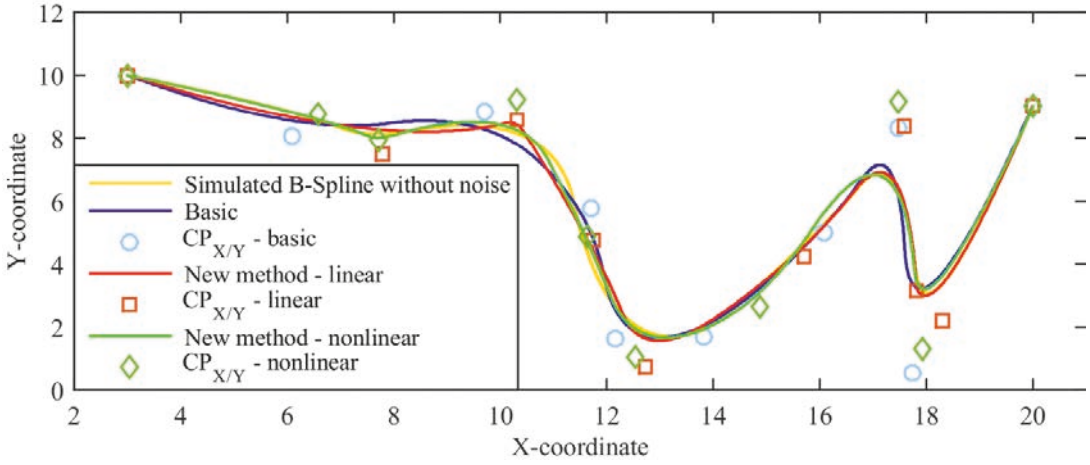

Fig. 5: Result of the B-Spline curve approximations – simulated data

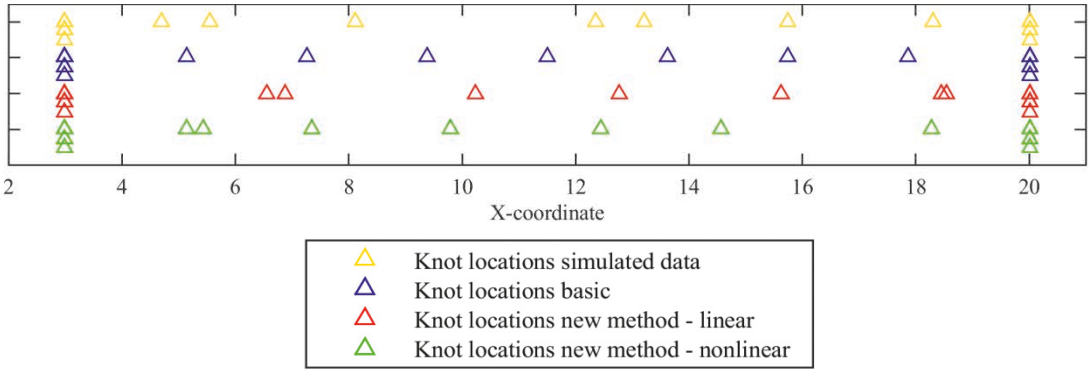

Fig. 6: Knot locations – simulated data

Both new methods show "significantly" better results than the basic one, in case of uncorrelated variances. The connected lines at the columns T_F in Table 2, Table 3 and Table 5 reveal both methods which are compared in the hypothesis test. For example the test value T_F between the basic and the new method linear and between the new method linear and nonlinear respectively is higher than its quantil. The obtained curves are shown in Figure 5.

The highest residuals are at the beginning where the new method produces sharp peaks in the linear case. The reason for that are the short spans at some locations in the knot vector. The new nonlinear method is closer to the $obs_{X/Y}$, but with a high curvature turn and smoother than the linear method. The basic method leads to a shift at the beginning of the curve up to $X \approx 11$ compared to the simulated dataset, which can be interpreted with a shift of the knots at that part. No systematic effects can be observed from the distribution of the control points.

Figure 6 shows the location of the knots for all used B-Splines. The locations of all knots differ from the simulated ones. Instead to the new method – nonlinear, which tend to have a similar knot location pattern as the simulated data. Although there is a significant improvement of the results, most knot locations of the simulated data cannot be reached.

Hypothesis tests cannot be performed correctly on the results, because in our case the

Noise	Parameterization method	$s_{apost.}$	T_F	T_F	$F_{9984, 9984, 0.05}$
Yes	Chordal	0.2932		56	1.034
Yes	Uniform (simulated)	0.0052	40		
Yes	Centripetal	0.2120			

Tab. 3: Results of linear least squares with different obs values (TF = Test value for the F-test, $F_{f1, f2, 1-alpha}$ = quantil of the F-distribution)

Type	Values
Number of knots	22
Number of basis functions / $CP_{X/Y}$	19
Degree	2
Dimension	2 (Z, X)
Sample points	5000 / 12293

Tab. 4: Parameters for the B-Spline approximation of the measured data

Num. Points	Method	$s_{apost.}$ [mm]	T_F	T_F	$F_{9940, 9940, 0.05}$ / $F_{24526, 24526, 0.05}$
5000	New method nonlinear	0.68		1.07	1.03
	New method linear	0.73	1.33		
	Basic	0.97			
12293	New method nonlinear	0.70		1.07	1.02
	New method linear	0.75	1.25		
	Basic	0.94			

Tab. 5: Results compared to each other – on measured data (TF = Test value for the F-test, $F_{f1, f2, 1-alpha}$ = quantil of the F-distribution)

functional model of each method changes. The reason is the different knot vector, which affects the calculated basis functions and the affiliation of the $obs_{Par.}$ to the basis functions. This aspect justifies the sequential knot optimization: the updates of the knot location in loop II are related to the actual functional model and not to the new one that accounts for changes of the basis-function-allocation and the relation of the $obs_{Par.}$ to the basis-functions. Different experiments on the dataset have shown that by estimating all knots at the same time the function changes increase so much, that the nonlinear model fails after the third iteration.

The reason for using the parameters of the simulated B-Spline itself is given by the differences between the three mentioned methods. The parameters differ significantly in the part of the curve with high curvature. As a result of this all known parameterization methods allocate insufficient $obs_{Par.}$ between the spans for the further approximation algorithms. This can be noticed in Table 3, where all linear approximations of the control points differ significantly from the ones obtained for the uniform case.

6.2 Measured Data

The measured data comes from a TLS profile scan, with a total length of 14m. The Z coordinate needs to be sensitive. Therefore it is trend reduced and scaled to [mm]. The X-coordinate is in [m] and represents the step size of points. The point density was reduced from 12293 to 5000

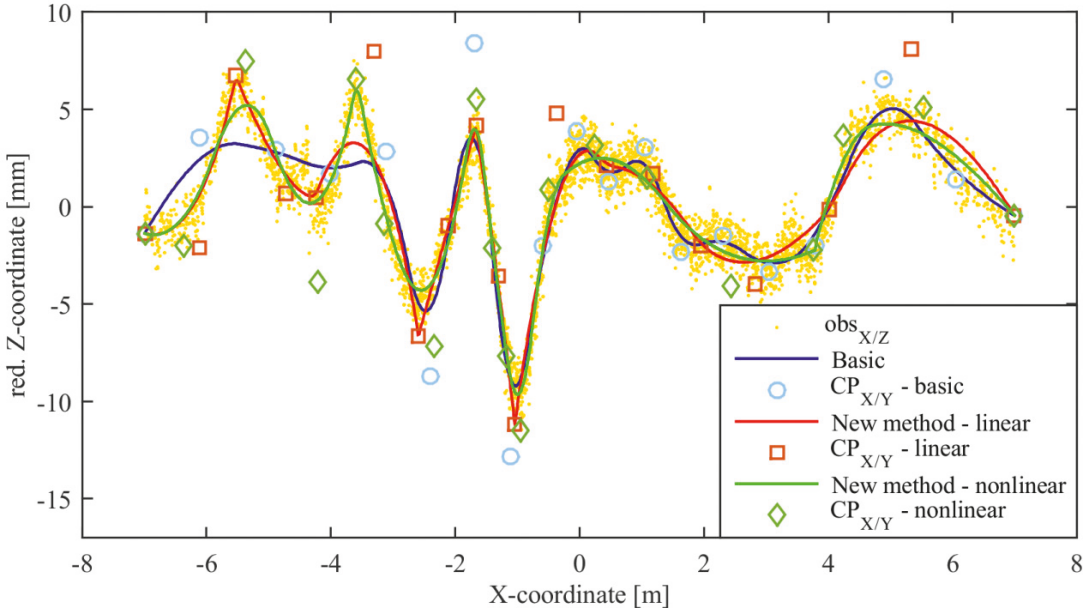

Fig. 7: Result of the B-Spline curve approximation – measured data

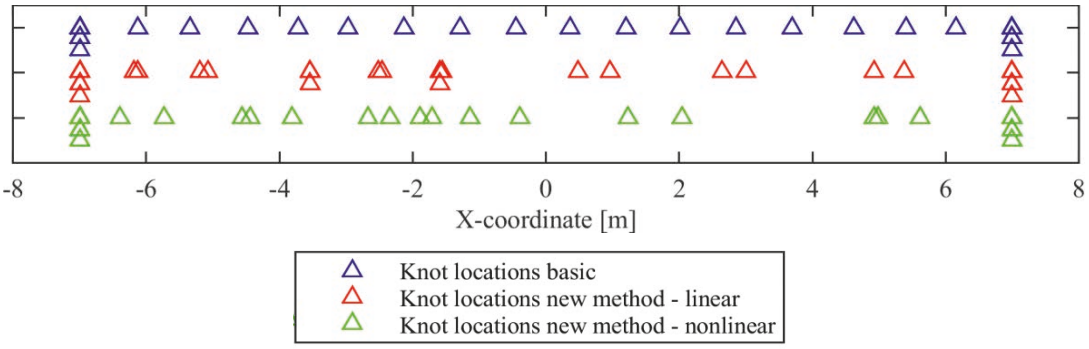

Fig. 8: Knot locations – measured data

points in order to emphasize the impact of the step size. The parameters for the B-Splines are given in Table 4.

The curve parameters allocated to the $obs_{X/Y}$ are calculated with the centripetal method. It has generated the best result compared to the other parameterization methods.

Results

The estimation results are summarized in Table 5. As can be seen the new methods are better than the basic one. However, the decrease of the standard deviation of the control-point estimation is not as strong as in the case of the simulated data set. The variation of the number of knots, degree of the basis function and the number of $obs_{X/Y}$ results in the gradation from the best result by the new method nonlinear to the basic method, as in Table 5. The "significant" changes need to be carefully interpreted with the difficulties of the hypotheses test in mind, mention in chapter 6.1. More explanation of how to read the table can be achieved under Table 2.

Figure 7 shows the different B-Spline curves after the knot estimation with the three methods in the case of 5000 sample points.

Especially at the beginning of the curve, the new methods lead to improved approximations

of $obs_{X/Y}$. In the section between 0 m and 4 m the approximation with the basic method is more detailed. These oscillations appear also in the case of estimation with the developed methods when a higher number of knots are used. The difference between the linear and the nonlinear case of the developed method is the smoothness of the curve. While in the linear case the curve is approximated with sharp peaks the nonlinear model leads to rounded peaks and a smoother curve.

Figure 8 shows the knot distribution in the knot vector. Noticeable are the large differences of the knot locations between the methods, which can also be seen in Figure 6. The reason for that are the large functional changes in the formulas between different parameter sets, which produce large differences in the residuals on which the new parameters rely on.

7. Conclusion

The new methods for the knot estimation improve the approximation of TLS profiles with B-Splines. The algorithms were validated with simulated data and applied on real data. They lead to better results than the basic method.

Despite the functional problems during the nonlinear iteration the algorithm converges when estimating only one knot at a time and allowing only small updates. This leads to good results also in case of higher knot numbers. The method doesn't use any problem specific smoothing or penalty terms. When estimating all knot locations at once the algorithm becomes unstable. Oscillations like in the case of polynomials with higher degree didn't occur when the estimation was performed by a maximum of 23 knots in order to reach the standard deviation of the simulated dataset.

Different parameterizations of the observations were implemented in order to analyze their influence on the approximation results. This influence tends to be higher than the influence of the right number of the knots. Similar approximation results were obtained for different numbers of $obs_{X/Y}$.

Extending the sequential nonlinear model to a global estimation of knots and control points is aimed in future research.

References

[1] Workshop Flächenrepräsentation. Workshop at the DGK Sektion Ingenieurgeodäsie, Rhön-Park, 2013.

[2] C. Schmitt, H. Neuner, I. Neumann, J. Piehler, M. Hansen, and S. Marx, Erstellung von Ist-Geometrien für strukturmechanische Berechnungen. Beiträge zum 17. Internationalen Ingenieurvermessungskurs Zürich, A. Wieser, Ed. Heidelberg, Wichmann Verlag, 2014, 37–48.

[3] C. de Boor, A practical guide to splines. New York; Berlin [u.a.], Springer, 1978.

[4] P. de Casteljau, Courbes et surfaces a pôles. André Citron Automobiles SA - Paris, 1959.

[5] C. Schmitt, H. Neuner, and I. Neumann, Strain detection on bridge constructions with kinematic laser scanning. Proceedings of the 2nd Joint international Symposium on Deformation Monitoring, 2013.

[6] H. Neuner, C. Schmitt, and I. Neumann, Modelling of terrestrial laser-scanning profile measurements with B-Splines. Proceedings of the 2nd Joint international Symposium on Deformation Monitoring, 2013.

[7] E. T. Y. Lee, Choosing nodes in parametric curve interpolation. Comput.-Aided Des., 1989, 21, 6, 363–370.

[8] P. Dierckx, Curve and surface fitting with splines. Oxford, Clarendon Press, 1995.

[9] M. J. Lindstrom, Penalized Estimation of Free-Knot Splines. J. Comput. Graph. Stat., Jun. 1999, 8, 2, 333–352.

[10] C. Harmening and H. Neuner, Raumkontinuierliche Modellierung mit Freiformflächen. Terrestrisches Laserscanning 2014 (TLS 2014) | Beiträge zum 139. DVW-Seminar, 1st ed., 78, Fulda, 2014, 228.

[11] L. A. Piegl and W. Tiller, The Nurbs Book. Springer, 1997.

[12] L. A. Piegl and W. Tiller, Surface approximation to scanned data. Vis. Comput., Nov. 2000, 16, 7, 386–395.

[13] I. J. Schoenberg and A. Whitney, On Polya Frequency Function. III. The Positivity of Translation Determinants With an Application to the Interpolation Problem by Spline Curves. Trans. Am. Math. Soc., 1953, 74, 2, pp. 246–259.

[14] A. Razdan, Knot Placement for B-Spline Curve Approximation. 1999.

[15] H. Park and J.-H. Lee, B-spline curve fitting based on adaptive curve refinement using dominant points. Comput.-Aided Des., Jun. 2007, 39, 6, 439–451.

[16] D. L. B. Jupp, The "Lethargy" theorem—A property of approximation by γ-polynomials. J. Approx. Theory, Jul. 1975, 14, 3, 204–217.

Contacts

Univ.-Ass. MSc. Claudius Schmitt, Vienna University of Technology, Department of Geodesy and Geoinformation, Engineering Geodesy, Gusshausstraße 27-29, E120-5, 1040 Vienna, Austria.

E-Mail: claudius.schmitt@geo.tuwien.ac.at

Prof. Dr.-Ing. Hans Neuner, Vienna University of Technology, Department of Geodesy and Geoinformation, Engineering Geodesy, Gusshausstraße 27-29, E120-5, 1040 Vienna, Austria.

E-Mail: hans.neuner@geo.tuwien.ac.at

Monitoring Tectonic Processes in Eastern Austria based on GNSS-derived site velocities




Elke Umnig, Ewald Brückl, Jadre Maras and Robert Weber, Wien

Abstract

Still ongoing tectonic processes over the Eastern Alps lead to the extrusion of parts of the Eastern Alps towards the Pannonian basin and the Carpathians. The project ALPAACT investigates intra plate movements in the Austrian region. As part of the studies a geodetically derived horizontal velocity field has been derived.

For a selection of about 20 sites of a permanent GNSS network, which covers the area of interest, coordinate time series have been obtained. The processed GNSS network is located in the eastern part of Austria, between the Bohemian Massif in the north and the Styrian basin in the south and spreads out over the most active zones of the area. The data series span a period of 4 years (2010 to 2013) so far. Daily coordinate solutions were calculated by means of the Bernese Software and station velocities with respect to the global reference frame ITRF2000 have been derived by means of a linear regression approach.

The quality of the time series can evidently be deteriorated by data gaps and physical obstructions surrounding the reference site, significant discontinuities are mainly caused by equipment changes at the observation sites. Apart from the linear station motion also nonlinear variations with predominately an annual period show up in the time series. Nevertheless the accuracy of the provided global velocity estimates can be assumed with accuracy at the level of 0.5 mm/y for individual stations. The geodetic data are consistent with a sinistral strike–slip deformation velocity of sub–mm/y along the Mur–Mürz valley–Semmering–Vienna Basin transfer fault system. The magnitude of the deformation velocity is significantly lower than values derived earlier from large scale GNSS networks and essential for the characterization of the plate tectonic regime and a realistic estimate of seismic hazard in this area.

Keywords: Plate tectonics, Geodetic monitoring, ALPAACT

Kurzfassung

Nach wie vor andauernde tektonische Prozesse in den Ostalpen führen zu einer Extrusion von Teilen der Ostalpen in Richtung des Pannonischen Beckens und der Karpaten. Das Projekt ALPAACT (seismological and geodetic monitoring of ALpine–PAnnonian ACtive Tectonics) untersucht innerplattentektonische Bewegungen in Österreich. Im Rahmen der Studien wurde ein geodätisch abgeleitetes horizontales Geschwindigkeitsfeld generiert.

Das prozessierte GNSS Netz befindet sich im östlichen Teil Österreichs, zwischen der Böhmischen Masse im Norden und dem Steirischen Becken im Süden und erstreckt sich somit über die seismisch aktivsten Bereiche des Untersuchungsgebietes. Für eine Auswahl von ca. 20 permanenten GNSS Beobachtungsstationen wurden bisher Koordinatenzeitreihen über eine Periode von 4 Jahren (2010 bis 2013) mittels der Software Bernese berechnet. Die Koordinatenzeitreihen beziehen sich auf den globalen Referenzrahmen ITRF2000. Anhand einer linearen Regression wurden Stationsgeschwindigkeiten abgeleitet.

Die Qualität der Zeitreihen kann durch Datenlücken sowie Abschattungen an den Referenzstationen beeinträchtigt werden, wobei signifikante Diskontinuitäten vor allem durch Hardwarewechsel an den Beobachtungsstationen verursacht werden. Neben den linearen Stationsbewegungen treten in den Zeitserien auch nichtlineare Variationen mit überwiegend jährlichen Perioden auf. Trotzdem kann von einer äußeren Genauigkeit im Bereich von 0.5 mm/Jahr für die geschätzten Geschwindigkeiten der einzelnen Stationen ausgegangen werden. Die Ergebnisse der geodätischen Beobachtungen sind konsistent mit der Geschwindigkeit im sub–mm/Jahr Bereich und entsprechen einer sinistralen Seitenverschiebung entlang des Störungssystems des Mur–Mürztals, des Semmerings und des Wiener Beckens. Die Magnitude der Deformationsgeschwindigkeit ist signifikant kleiner als die Ergebnisse, welche aus frühen großräumigen GNSS Kampagnen stammen und stellt somit einen wichtigen Beitrag zur Beschreibung der plattentektonischen Situation und einer realistischen Abschätzung des Erdbebenrisikos im Untersuchungsgebiet dar.

Schlüsselwörter: Plattentektonik, Geodätisches Monitoring, ALPAACT

1. Introduction

The collision of the European and Adriatic plates, exhumation forming the Penninic windows and extrusion and tectonic escape of crustal blocks to the Pannonian basin influenced the current appearance of the Eastern Alps most strongly. Neotectonic or reactivated geological structures, seismic activity and large scale deformation patterns observed by GNSS indicate that Neogene tectonic processes are still ongoing. The Vienna Basin and the Mur–Mürz valley have been formed by pull–apart and strike–slip faults crossing the Semmering region and extending along the Mur–Mürz valley. The Mur–Mürztal and Vienna Basin fault zones are seismically the most active regions in Austria.

Within the frame of project ALPAACT (seismological and geodetic monitoring of ALpine–PAnnonian ACtive Tectonics) [6], [7], a GNSS network, located in the eastern part of Austria, between the Bohemian Massif in the north and the Styrian basin in the south, has been processed over a period of 4 years. The most northern sites belong to the Bohemian Massif, which represents the European plate and is seen as a stable part within the network. In the centre of the network, observation stations are directly grouped along the main transfer faults, which are the Mur–Mürz valley and the Vienna basin. Stations in the south–east belong to the Styrian basin, respectively the Pannonian platform.

Coordinate time series were calculated using the Bernese Software and station velocities aligned to the global reference frame ITRF2000 have been obtained to support the geophysical investigations in this area.

2. Tracking Network

The processed GNSS network includes 22 permanent GNSS observation sites, in which the stations Graz, Penc and Mattersburg are part of the global IGS network (International GNSS Service; www.igs.org) and are labelled in Figure 1 according to their official four character identification. Site TRF2 (Trafelberg) belongs to the EPN network (Euref Permanent Network; http://www.epncb.oma.be), the other sites are part of the real time positioning services EPOSA (Echtzeit Positionierung Austria) and the EVN–satellite positioning service respectively. Each station in the network is equipped with a dedicated antenna receiver and/or radome combination.

A station information file records the equipment changes at the observation sites. To account for the antenna phase center variations of the satellite and the ground antennas correction terms have been applied in the GNSS data processing. These PCV model values are derived from absolute antenna calibration techniques.

3. Data and Processing Method

Observation data from the IGS tracking stations (on both GPS carriers L1 and L2 from 24 hour sessions with a time resolution of 30 seconds) as well as other IGS products, such as precise satellite orbits, geocentric coordinates of the IGS tracking stations or Earth orientation parameters are available through the IGS data centers and are free of charge. Observation data from the EPN network are also publicly accessible. All computations have been carried out by means of the Bernese Software. In principle the coordinate time series result from two processing campaigns. One GNSS campaign was mainly set up to contribute to the investigations in the framework of the ALPAACT project and covers the period from 2010.0 to 2013.5. The associated observation network was described above and is shown in Figure 1. The second GNSS campaign, designated as PROAUT started to be operational recently and consists of about 100 sites with a distribution over the whole Austrian territory and parts of the neighbouring countries. It has been established to support various multifunctional requests, such as in the context of atmospheric studies, the estimation of station–specific tropospheric zenith path delays. The coordinate time series for the period July–December 2013 are processed within this nationwide network. Due to the update of the Bernese Software from version 5.0 to version 5.2, the usage of a new ITRF realisation or parameter estimates over unequal time intervals both campaigns cannot be assumed to be completely consistent. The processed coordinate time series for the period from 2010.0 to 2013.5 are tied to the global reference frame ITRF2000. In contrast, the coordinate time series of the last 6 months in 2013 are primarily aligned to the global reference frame ITRF2008, but have been realigned in an additional processing step to the global reference frame ITRF2000 to ensure continuity.

The processing strategies for both campaigns follow likewise the guidelines of a modern GNSS network approach [9], [12], where double differences are applied, the tropospheric refraction is handled by implementing the dry and wet Niell Mapping Functions or the dry and wet Global Mapping Functions [4] respectively. The latter

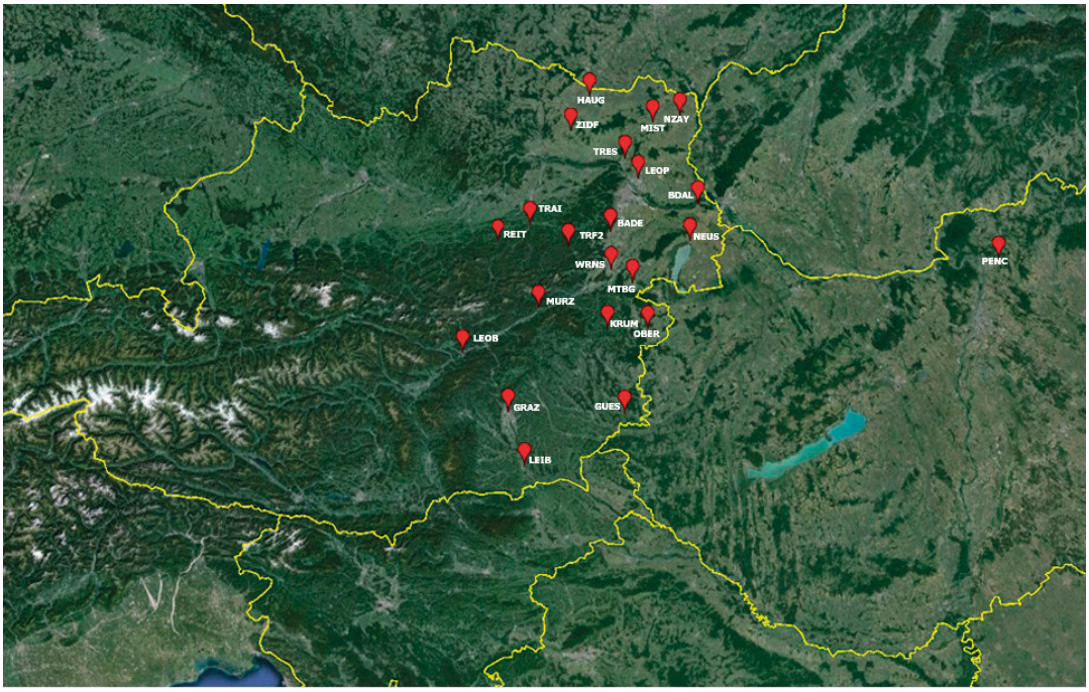

Fig. 1: Tracking GNSS network (ALPAACT)

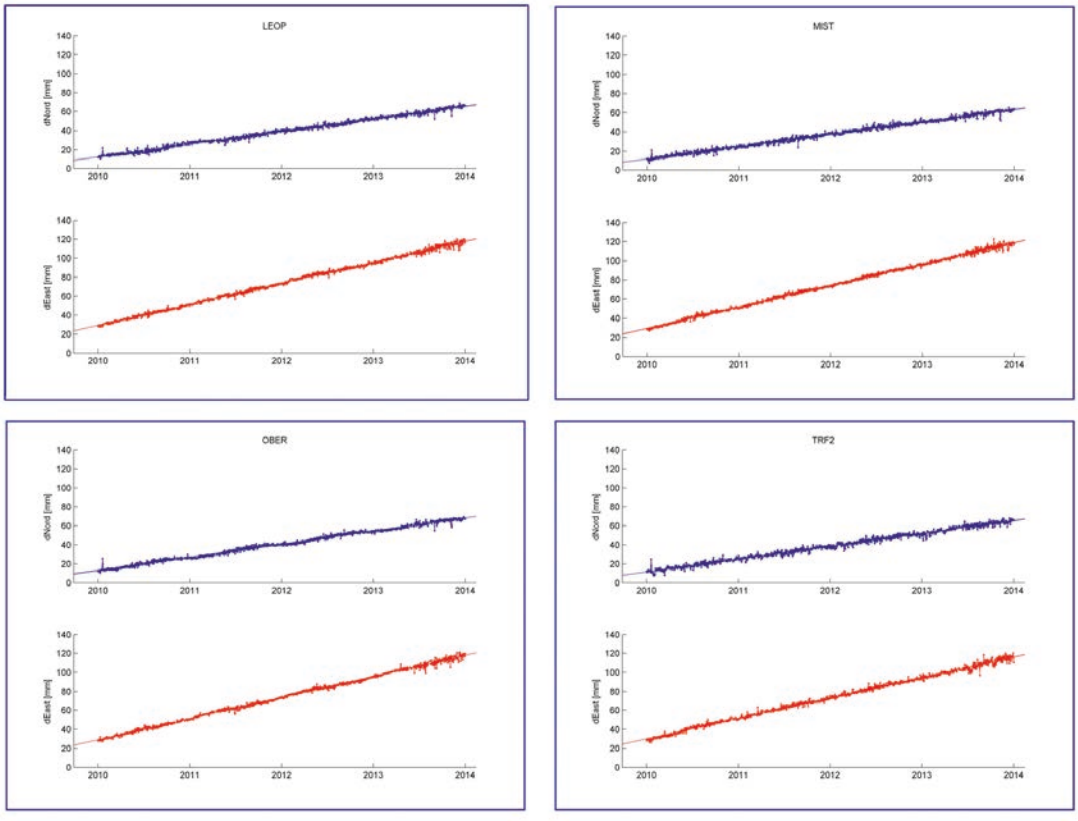

Fig. 2: Coordinate time series (2010 to 2013)

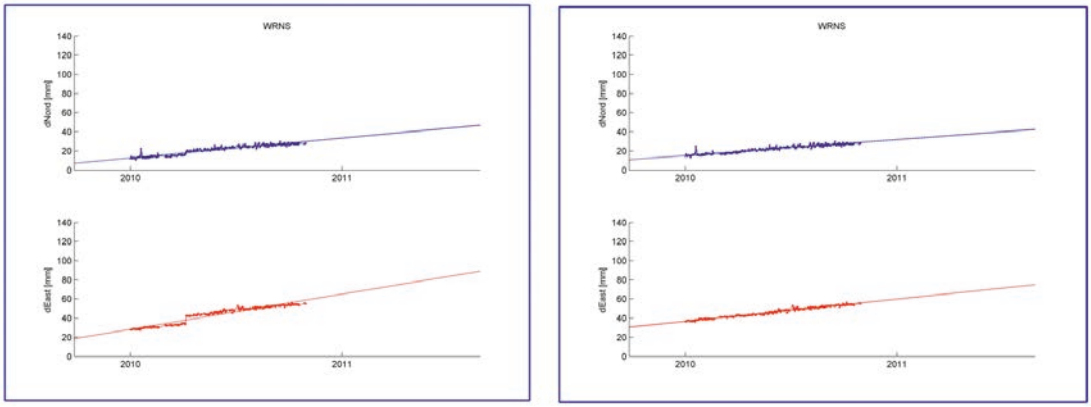

Fig. 3: Coordinate time series WRNS

are used within the nationwide campaign. The impact of the ionosphere is eliminated by computing the ionosphere–free linear combination by means of the narrow–lane strategy and daily coordinate solutions are estimated within a least square adjustment. The underlying datum of the generated network solutions in both campaigns has been defined by implementing IGS site coordinates into the processing. Regarding the ALPAACT campaign the site coordinates of GRAZ (Graz), PENC (Penc) and MTBG (Mattersburg) have been constrained to their ITRF2000 (epoch 1997.0) values. Moderate constraints ±1 mm/coordinate are applied to the coordinates of these 3 frame defining sites to avoid artificial deformations of the network.

4. Coordinate Time Series

The computed coordinate time series start on Jan, 1st, 2010 respectively the date when data for a special reference site are available for the first time. Figure 2 shows a selection of daily coordinate time series (north and east components) of the processed sites with respect at our chosen reference coordinates at epoch 2008.0: LEOP (Leopoldau), MIST (Mistelbach), OBER (Oberpullendorf) and TRF2 (Trafelberg).

Since July 1st, 2013 the temporal resolution of troposphere parameters was raised in the computations to support atmospheric studies. This switch causes due to parameter correlations a slight increase in the noise of the estimated coordinates. Although we have estimated of course 3D site coordinates all further investigations are restricted to the plane coordinates. Apart from the linear station motion, discontinuities, caused by equipment changes at the observation sites and data gaps (if the site has been decommissioned, for instance) show up in the time series. An example is given in Figure 3 (site WRNS–Wiener Neustadt), where no observation data are available since GPS–day 303 in the year 2010 and the hardware change on GPS–day 096 in the year 2010 induces a significant jump in the corresponding time series. Here the coordinate offset has been corrected accordingly before estimating a velocity vector. Figure 3 shows the coordinate time series from WRNS (Wiener Neustadt) before and afterwards the correction.

Another problem is related to natural (mountains) and physical obstructions surrounding the reference site. For example, as shown in Figure 4, poor satellite geometry at site MURZ (Mürzzuschlag) increases the noise of the estimated coordinate time series significantly in comparison to other network sites.

Even in the time series of the horizontal coordinates in north and east direction also nonlinear variations appear with predominately an annual period (seasonal effects). As example the coordinate time series for stations NEUS (Neusiedl) and TRAI (Traisen) are illustrated in Figure 5.

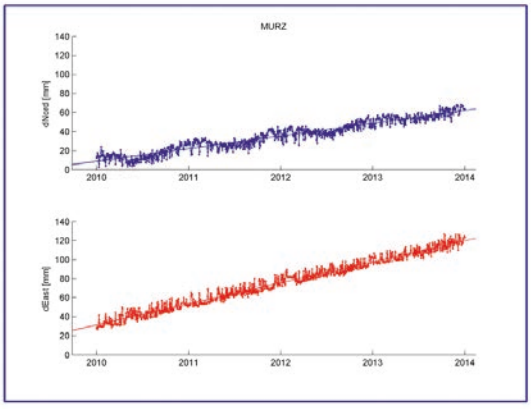

Fig. 4: Coordinate time series MURZ

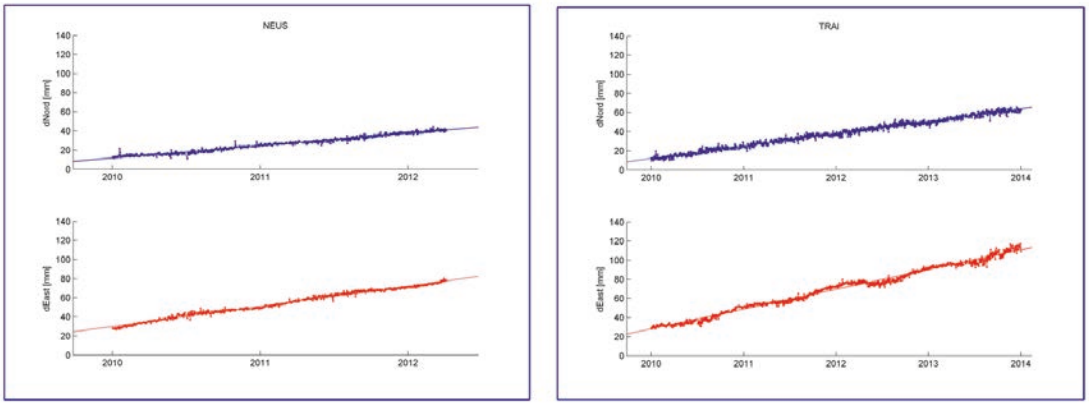

Fig. 5: Coordinate time series NEUS and TRAI

STAT	LAT (approx)	LONG (approx)	ve [mm/yr]	vn [mm/yr]
BADE	48.00	16.25	21.97	13.50
BDAL	48.12	16.92	22.31	13.37
GRAZ	47.07	15.49	21.47	13.92
GUES	47.07	16.32	22.45	13.61
HAUG	48.70	16.07	25.08	13.49**
KRUM	47.50	16.20	22.22	13.53
LEIB	46.78	15.55	21.67	14.85*
LEOB	47.39	15.09	22.67	13.36
LEOP	48.27	16.42	22.15	13.36
MTBG	47.74	16.40	22.05	13.24*
MIST	48.57	16.57	22.36	12.92
MURZ	47.61	15.68	22.07	13.35
NEUS	47.96	16.84	21.15	12.99
NZAY	48.61	16.80	23.02	11.98*
OBER	47.51	16.50	22.22	13.86
PENC	47.78	19.28	22.84	12.84
REIT	47.88	15.31	23.65	14.54*
TRAI	48.06	15.61	20.70	12.91
TRES	48.37	16.36	21.90	12.83
TRF2	47.93	15.86	21.51	13.54
WRNS	47.82	16.27	23.14	16.57**
ZIDF	48.63	15.92	21.74	13.33
* Time series with observation data less than 4 years				
**Time series with observation data less than 2 years				

Tab. 1: ITRF2000 velocities

STAT	ve_eur [mm/y]	vn_eur [mm/y]
BADE	–0.11	–0.99
BDAL	0.23	–1.12
GRAZ	–0.62	–0.57
GUES	0.37	–0.88
HAUG	**	**
KRUM	0.14	–0.96
LEIB	–0.41	0.36
LEOB	0.58	–1.13
LEOP	0.07	–1.13
MTBG	–0.03	–1.25
MIST	0.28	–1.57
MURZ	–0.01	–1.14
NEUS	–0.94	–1.50
NZAY	0.94	–2.51
OBER	0.14	–0.63
PENC	0.76	–1.65
REIT	1.57	0.05
TRAI	–1.39	–1.58
TRES	–0.18	–1.66
TRF2	–0.57	–0.95
WRNS	**	**
ZIDF	–0.34	–1.16
**data gaps		

Tab. 2: Mean Eurasian velocities

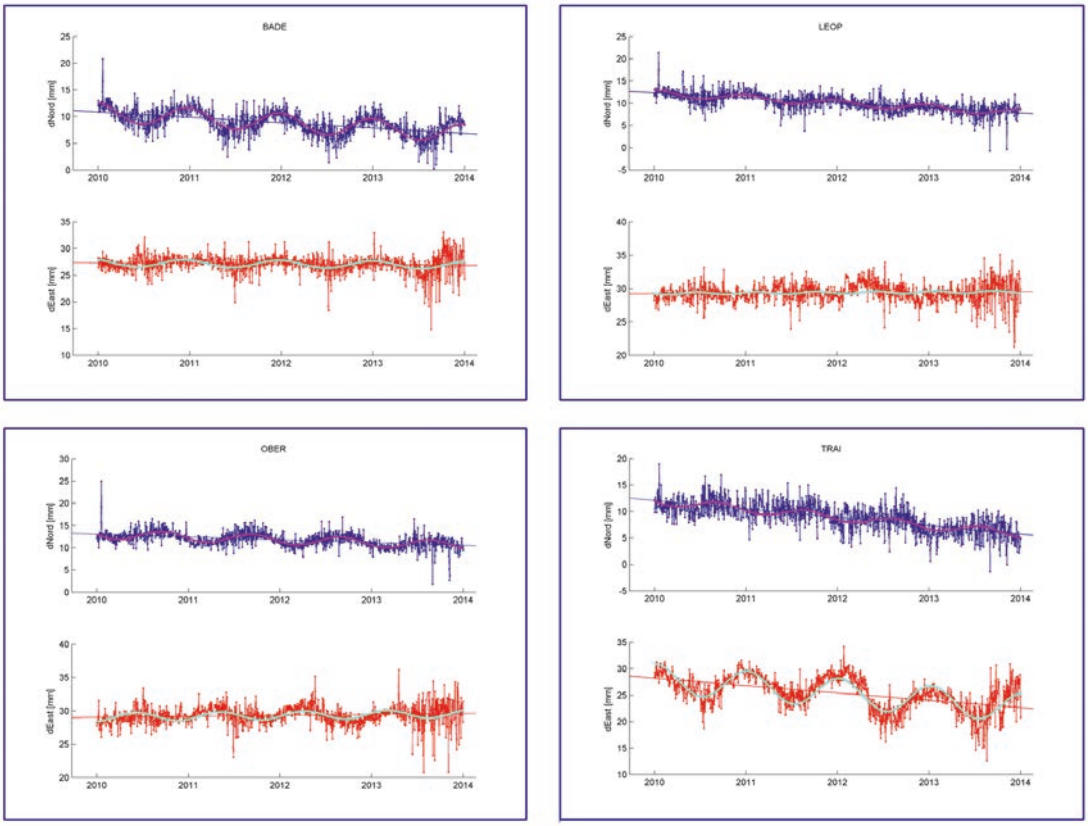

Fig. 6: Local station movement

5. Estimation of ITRF Velocites

Annual station velocities with respect to the global reference frame ITRF2000 have been derived by means of a linear regression approach. A full list of the global site velocities for the components east (ve) and north (vn) is detailed in Table 1.

The formal error of the provided velocity components is at the +/– 0.2mm/year level while a more realistic accurcacy estimate points (depending on the individual site) at the +/–0.5 mm/y level.

As the velocity estimates during the processing period are partly harmed by missing data, we restrict our further interpretations on the site velocity estimates, where at least observation data for more than 2 years are available.

6. Motion with respect to the Eurasian Plate

To obtain a motion field with respect to the Eurasian plate every ITRF site velocity has to be corrected by the common Eurasian plate motion. There are several meaningful methods to apply this correction. Here we have a straight forward approach by subtracting the mean ITRF2000 velocity of the IGS site GRAZ (ve_Graz = 22.07mm/y; vn_Graz =+14.56mm/y). Practically every site coordinate has been referred to the corresponding motion of site GRAZ. In a further step the remaining velocity has been estimated by means of a linear regression. Table 2 summarizes the estimated mean station velocities in north and east direction (ve_eur) and (vn_eur) with respect to the Eurasian plate.

7. The Local Trend– Non LinearVariations

The remaining trend in the signal reflects the local station movement and can be further analyzed: As already mentioned in chapter 4 at most stations periodical (annual) motions superimpose the mainly linear station motions. To insulate this periodic effects from further interpretation and most of all to prevent a systematically wrong estimation of the underlying linear station motion we tried to estimate phases and amplitudes of this periodic behaviour. The values for the parameters amplitude, phase and period are estimated by applying a minimum search algorithm. Corre-

STAT	eAmp [mm]	ePha [days]	nAmp [mm]	nPha [days]
BADE	0.69	7.33	1.78	19.16
LEOP	0.39	20.74	0.72	12.40
OBER	0.62	14.07	1.03	13.77
TRAI	2.74	18.86	0.76	13.33

Tab. 3: Amplitude and phase computed from data for the time span (2010 to 2013)

sponding for a selection of sites the periodicity in east and north direction is illustrated in Figure 6.

As all the resulting periods were close to one year (346 days – 375 days) we fixed the period to exactly one year. The remaining values for the amplitudes (eAmp, nAmp) and phase (ePha, nPha) in the components east and north are shown in Table 3. North and east components are handled separately.

Additionally corrections (due to the correct accounting for periodical effects) for the site velocities have been obtained from the processed period from 2010.0 to 2014.0. Most of this corrections are well below the 0.05 mm/y level, but some are not negligible (such as for instance for site NEUS with correction values of 0.14 mm/y in east and –0.08 mm/y in north direction respectively). These corrections are due to phase angles far different from 0 degree of the periodic effects which map into the linear motion coefficients.

8. Resumé

Coordinate time series for the years 2010, 2011, 2012 and 2013, which are tied to the global reference frame ITRF2000 (epoch 1997.0) have been processed. The velocity estimates of the stations HAUG and WRNS are of less quality due to equipment changes and large data gaps during the considered observation period and have not been considered in the further analysis. Finally the station velocities with respect to the Eurasian plate have been computed from the available data sets. The finally achieved velocity estimates (ve_vel, vn_vel) with respect to a mean motion of the Eurasien plate are summarized in Table 4 below.

Figure 7 shows the velocity vectors plotted on a geological map. The average velocity value of all stations in the target area has beeen subtracted in order to enhance the local tectonic kinematics. At a first view these velocity vectors appear rather randomly distributed with a few outliers (LEIB, NZAY, REIT, TRAI). We consider the velocity components parallel to the Mur–Mürz and Vienna Basin transfer fault system and exclude stations on or near the fault system (BADE, BDAL, LEOB, MTBG, MURZ). A sinistral

STAT	ve_vel [mm/y]	vn_vel [mm/y]
BADE	–0.12	–1.01
BDAL	0.16	–1.10
GRAZ	–0.61	–0.58
GUES	0.27	–0.85
HAUG	**	**
KRUM	0.12	–0.97
LEIB	–0.43	0.41
LEOB	0.56	–1.11
LEOP	0.06	–1.14
MTBG	0.02	–1.30
MIST	0.24	–1.57
MURZ	–0.01	–1.08
NEUS	–0.80	–1.58
NZAY	0.90	–2.52
OBER	0.16	–0.72
PENC	0.73	–1.63
REIT	1.57	0.08
TRAI	–1.34	–1.63
TRES	–0.21	–1.70
TRF2	–0.60	–0.99
WRNS	**	**
ZIDF	–0.34	–1.18
**data gaps		

Tab. 4: Final estimated velocities in the components north and east

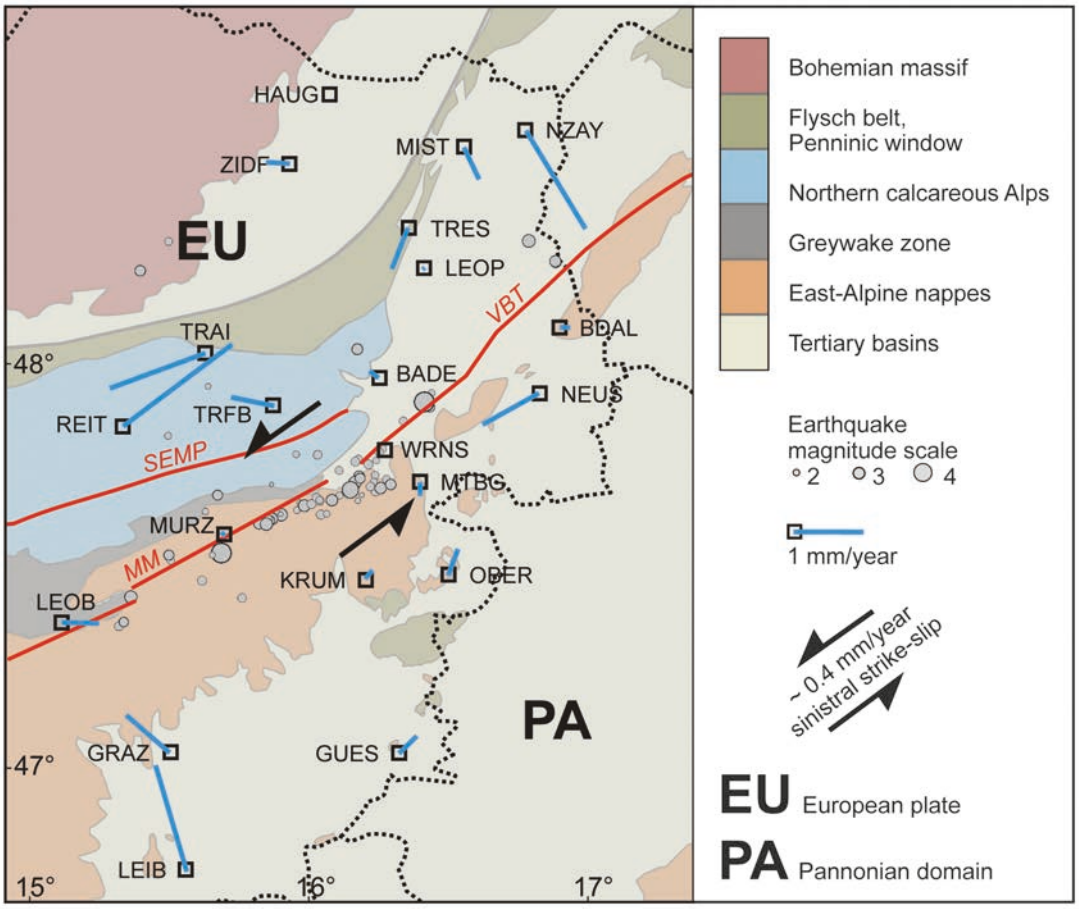

Fig. 7: Generalized geological map of the study area (generalized after [13]) and velocity vectors; SEMP …Salzachtal – Ennstal – Mariazell – Puchberg fault, MM …Murtal – Mürztal fault, VBT …Vienna basin transfer fault system; earthquake epicentres from 2009–05–07 to 2013–09–20 [7].

strike–slip movement of 0.35 mm/y of the Pannonian domain (GRAZ, GUES, KRUM, LEIB, OBER) relative to the European plate (LEOP, MIST, NZAY, REIT, TRAI, TRES, TRFB, ZIDF) along the fault system (average strike 54°, NE–SW) follows from this data. In case we exclude the outliers from the calculation we get 0.43 mm/y. Both values for the magnitude of the strike–slip movement are much lower than the value of about 1.5 mm/y assumed in earlier studies [3], [11]. The average seismic slip rate was estimated to 0.22 – 0.31 mm/y for the Vienna Basin transfer fault by the analysis of earthquake catalogues [11]. Therefore our new geodetically observed slip rate reduces significantly the estimated seismic slip deficit and should be considered in future studies concerning seismic hazard in the Vienna Basin.

The magnitude of sinistral slip along the Mur–Mürz and Vienna Basin transfer faults system imposes a constraint on the plate tectonic system in the Eastern Alps. This system is built by the European plate (EU), the Adriatic micro–plate (AD) and the Pannonian domain (PA), which may be considered as a third tectonic plate [5]. The lithospheric mantles of these tectonic blocks form a triple junction at 13.6°E, 46.7°N. Figure 8a shows a simplified model of this plate tectonic scheme valid for the actual geodynamic situation [8].

It is assumed that the triple junction is actually moving along the AD–PA plate boundary to the southeast, changing the plate boundary from dextral strike–slip to subduction behind it. The velocity triangle at this triple junction (Figure 8b) is determined by the northward orientation of the

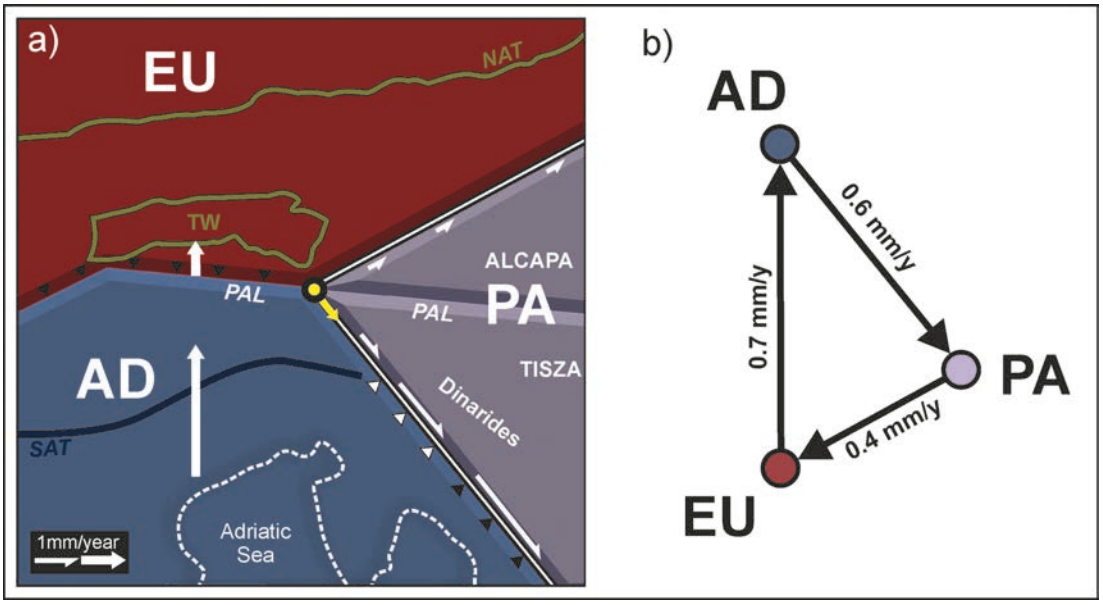

Fig. 8: Plate tectonic model of the lithospheric mantle of the Eastern and Southern Alps; ***a)*** *generalized model of the plate tectonic regime (modified after [8]); AD (Adriatic micro–plate), EU (European plate), PA (Pannonian domain), NAT (Northern Alpine thrust fault), PAL (Periadriatic lineament), SAT (Southern Alpine thrust fault), TW (Tauern Window);* ***b)*** *velocity triangle of the stable triple junction AD – EU – PA marked by a black circle with yellow fill in a).*

velocity of AD versus EU, the stability condition for this type of triple junction and the sinistral strike–slip velocity at the EU–PA boundary as derived from our new GNSS data (Figure 8b). It is assumed that a compressional zone observed by GPS in the Southern Alps [10] comprises also the lithospheric AD mantle [5]. The northward oriented velocity of AD versus EU is reduced from about 2.5 mm/y to a subduction velocity of 0.7 mm/y at the AD–EU boundary by this intra–plate compression.

Future investigations should clarify if the outliers could be caused by geotechnical circumstances (e.g., unstable foundation of the buildings where the antennas are installed) or be local geological processes (e.g., mass movements). Further, the time series shall be enhanced by regularly processing the observation data close to the current day. Currently GNSS observation data from 2010.0 to 2015.0 (even for the whole Austrian territory) can be made available by the contributing organisations. To enhance the time bases of the coordinate series towards half of a decade promises consistent velocity estimates for individual stations at the +/–0.3 mm/y level. Furthermore a more detailed investigation of non–linear station motions is proposed.

Acknowledgements

The authors would like to thank the Austrian Academy of Sciences for funding this project and the EPOSA and EVN Satellite Positioning services to provide the RINEX observation data for post–processing.

References

[1] *Altamimi Z., Sillard P.; Boucher C. (2002)*: ITRF2000: A new release of the International Terrestrial Reference Frame for earth science applications. Journal of Geophys. Res., Vol. 107, B10, 2214.

[2] *Altamimi Z., Collilieux X., Métivier L. (2011)*: ITRF2008: an improved solution of international terrestrial reference frame. Journal of Geod., 85, 457–473.

[3] *Beidinger A., Decker K. (2011). 3D geometry and kinematics of the Lassee flower structure*: implications for segmentation and seismotectonics of the Vienna Basin strike–slip fault, Austria. Tectonophysics 499, pp. 22–40, doi: 10.1016/j.tecto.2010.11.006

[4] *Böhm J., Niell A., Tregoning P., Schuh H. (2006)*: Global Mapping Function (GMF): A new empirical mapping function based on numerical weather model data. Geophys. Res. Lett., 33.

[5] *Brückl E., Behm M., Decker K., Grad M., Guterch A., Keller G. R., Thybo H. (2010)*: Crustal structure and active tectonics in the Eastern Alps, Tectonics, 29, TC2011, doi:10.1029/2009TC002491.

[6] *Brückl E., Weber R. et al. (2013)*: ALPAACT – seismological and geodetic monitoring of ALpine–PAnnonian ACtive Tectonics. Poster for the European Geosciences Union General Assembly 2013 Vienna, Austria, 07–12 April 2013.

[7] *Brückl E., Weber R. et al. (2014)*: ALPAACT – Seismological and Geodetic monitoring of ALpine–PAnnonian ACtive Tectonics. Final Report, Austrian Academy of Sciences, ISBN–Online: 978–3–7001–7738–8, DOI: 10.1553/ALPAACT.

[8] *Brückl E., Hammerl Ch. (2014)*: Eduard Suess´ conception of the Alpine orogeny related to geophysical data and models. Austrian Journal of Earth Sciences, 107, 1; 94–114.

[9] *Dach R., Hugentobler U., Fridez P., Meindl M. (2007)*: Bernese GPS Software, Version 5.0, AIUB Astronomical Institute, University of Berne.

[10] *Grenerczy G., Kenyeres A. (2006)*: Crustal deformation between Adria and the European platform from space geodesy. In: N. Pinter et al (eds.), The Adria Microplate: GPS Geodesy, Tectonics and Hazards. NATO Sci. Ser. IV, vol. 61, 321–334, Springer, Dordrecht, Netherlands, doi:10.1007/1–4020–4235– 3_22.

[11] *Hinsch R., Decker K. (2010)*: Seismic slip rates, potential subsurface rupture areas and seismic potential of the Vienna Basin Transfer Fault. International Journal of Earth Sciences, doi: 10.1007/s00531–010–0613–3.

[12] *Möller G., Brückl E., Weber R. (2011)*: Active tectonic deformation at the transition from the European and Pannonian domain monitored by a local GNSS network, Österreichische Zeitschrift für Vermessung und Geoinformation, 99. Jahrgang, Heft 2/2011, pp. 138–148.

[13] *Schmid S. M., Fügenschuh B., Kissling E., Schuster R. (2004). Tectonic map and overall architecture of the Alpine orogen. Eclogae Geologicae Helvetica, 97, pp.93–117.*

[14] *Umnig E., Möller G., Weber R. (2012)*: Geodetic monitoring of intra–plate velocities. Poster for the European Geosciences Union General Assembly 2012 Vienna, Austria, 22–27 April 2012.

Contacts

Dipl.-Ing. Elke Umnig, Vienna University of Technology, Department of Geodesy and Geoinformation, Advanced Geodesy, Gusshausstraße 27–29, 1040 Vienna, Austria.
E–Mail: elke.umnig@ geo.tuwien.ac.at

Em.O.Univ.Prof. Dipl.-Ing. Dr.phil. Ewald Brückl, Vienna University of Technology, Department of Geodesy and Geoinformation, Geophysics, Gusshausstraße 27–29, 1040 Vienna, Austria.
E–Mail: ewald.brueckl@geo.tuwien.ac.at

Bakk.techn. Jadre Maras, Vienna University of Technology, Department of Geodesy and Geoinformation, Advanced Geodesy, Gusshausstraße 27–29, 1040 Vienna, Austria.
E–Mail: jadre.maras@ geo.tuwien.ac.at

Ao.Univ.Prof. Dipl.-Ing. Dr.techn. Robert Weber, Vienna University of Technology, Department of Geodesy and Geoinformation, Advanced Geodesy, Gusshausstraße 27–29, 1040 Vienna, Austria.
E–Mail: robert.weber@ geo.tuwien.ac.at

Investigation on the influence of the incidence angle on the reflectorless distance measurement of a terrestrial laser scanner




Miriam Zámečníková, Hans Neuner, Stefan Pegritz and Robert Sonnleitner, Wien

Abstract

Although the influence of incidence angle (IA) is one of the known error influences of terrestrial laser scanners (TLS), it is not taken into account in the evaluation of TLS-data. In this paper the fundamental question is discussed, how the IA influences the TLS-distances, if the uncertainty is of stochastic or of systematic nature or of a combination of both. For this purpose, a new methodology has been developed. Its special feature is that the directly measured TLS-distances are compared with reference distances. It can be applied for close range and for longer distances. The methodology was realised with a time of flight laser scanner. At close range of 3.5 to 5.2 m other error effects up to 4.4 mm are more pronounced than the influence of IA. At the distance of about 30 m, a systematic effect of IA was found. The total variation of the distance difference with IA is of ca. 2.0 mm. The stochastic properties of the influence of IA could not be quantified. In future works the methodology will be improved with respect to the obtained knowledge in order to quantify the error influence completely.

Keywords: Incidence angle, reflectorless distance measurement, laser scanner, scanning total station, close range, cyclic distance deviation

Kurzfassung

Obwohl der Einfluss des Auftreffwinkels (AW) zu den bekannten Fehlereinflüssen von terrestrischen Laserscannern (TLS) gehört, wird er bei der Beurteilung von TLS-Daten äußerst selten berücksichtigt. In diesem Paper wird eine grundsätzliche Frage behandelt, ob er stochastischer oder systematischer Natur ist oder eine Kombination von beiden darstellt. Dazu wurde eine neue Methodik entwickelt. Ihre Besonderheit besteht darin, dass die direkt gemessenen TLS-Distanzen mit Referenzdistanzen verglichen werden. Sie ist optional für den Nahbereich und für längere Entfernungen umsetzbar und wird hier mit einem impulslaufzeitbasierten TLS realisiert. Im Nahbereich von 3,5 bis 5,2 m wirken sich andere Fehlereinflüsse mit Beträgen bis 4,4 mm stärker auf die Distanzmessung aus als der AW. In der Entfernung von 30 m wurde ein systematischer Effekt des AW festgestellt. Die Distanzänderung in Abhängigkeit vom AW beträgt ca. 2,0 mm. Die stochastischen Eigenschaften des Einflusses des AW konnten nicht quantifiziert werden. Eine zukünftige Verbesserung der Methodik ausgehend von den gewonnenen Erkenntnissen soll eine vollständige Beschreibung dieses Fehlereinflusses gewährleisten.

Schlüsselwörter: Auftreffwinkel, reflektorlose Distanzmessung, Laser Scanner, scannende Total Station, Nahbereich, zyklische Distanzabweichungen

1. Introduction

In general, the geometry of object surfaces is determined from terrestrial laser scanning (TLS) measurements under varying incidence angles (IA). In consequence, the circular laser spot is deformed to an ellipse so that less signal strength is reflected back in comparison to its perpendicular alignment. The IA of the laser can affect the reflectorless distance measurements (RL) and thus, the TLS-data. In order to consider this influence in the TLS-measurement's planning as well as in the evaluation of TLS-data and in the object modelling, the quantification of its impact is necessary.

Existing publications explain the influence of IA on the distance measurement (i) by the changing geometry in the laser-surface interaction, (ii) in view of the reflected signal strength from the measured surface and (iii) as a combination of both.

(i) The geometrically-based explanation is twofold: Due to the deformation of the laser spot the center of the ellipse does not match the geometric end-point of the distance, which may lead

to deviation of the measured distance [1, 2] or the average of the distances within the laser spot is longer compared to the distance measured in the spatial direction determined by the horizontal direction and the zenith distance [3].

(ii) Due to the dominant signal strength which is concentrated in the nearer part of the elliptical laser spot more signal is reflected back from this area of the laser spot. As a result, the near area is more heavily weighted in the mixed signal and leads to shorter distances [4, 5]. Alternative theory states that the geometrical change of the laser spot reduces the reflected signal strength [6, 7, 8] which in turn influences the distance measurement.

Previous investigations on the influence of IA on the distance measurement of TLS are characterised by three problems. First, the character of the error influence is not clear. In some studies it has been described by a correction term [1, 6, 9] which indicates a systematic nature and in others by a standard deviation which can indicate a stochastic [8] or a systematic character [3, 10]. Secondly, the impact was assessed by indirectly derived parameters. Aspects such as form and geometric quality of the measured objects, heterogeneous errors influencing the collected TLS-data and applied estimation algorithms can also falsify the quantified influence of the error. For the third the impact of the IA was quantified mainly at close range.

In this paper, the influence of IA on the RL measurement is quantified in such a way that the mentioned problematic aspects are minimised. The aim is to answer the fundamental question, whether the influence of the IA on the measured distances is of stochastic or of systematic nature or a combination of both.

A new methodology to investigate the error influence is introduced. Instead of deriving the parameters indirectly, the study is performed on the level of directly TLS-measured distances which are compared with reference distances. To investigate the error influence at greater distances, two variants of the method have been developed for close range and for longer distances. The method is suitable for scanning total stations (TLS + TS).

The proposed methodology is executed with a time of flight TLS. The realised measurement set-ups and measurement procedures are described in detail. After evaluation of the measured data, the results are analysed, evaluated and discussed in the framework of these research issue.

2. Methodology

Our investigations of the influence of IA are based on the direct comparison of the reference with the TLS-distance. The investigated TLS-distance D_{TLS} is defined as the distance between the zero point of TLS + TS and the scanned point P_i (see Figure 1).

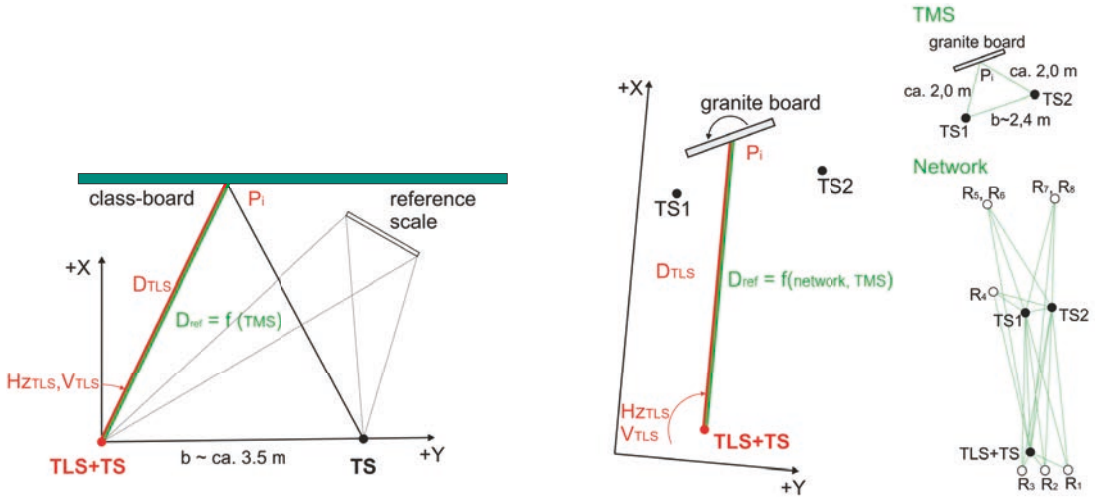

a) b)

Fig. 1: Measurement setup ***a)*** *for close range,* ***b)*** *for longer distance*

The methodology consists of the following steps (Figure 1):

1) A planar object (class-board, granite board) is scanned from a standpoint of TLS + TS. The coordinates Y_{TLS}, X_{TLS}, Z_{TLS} of the point cloud are converted into polar coordinates Hz_{TLS}, V_{TLS}, D_{TLS} (horizontal direction, zenith distance, distance).
2) The point on the object P_i is staked out via Hz_{TLS}, V_{TLS} using the tacheometric part of the instrument TLS + TS and signalised. The fundamental condition must be fulfilled, that TLS and TS work in the same coordinate system.
3) The end points of the studied distance P_i are determined with a theodolite measurement system (TMS). Subsequently, the reference distance D_{ref} is calculated from the determined coordinates. The TMS consists of TLS + TS and another TS instrument (Figure 1 a).
4) For the investigation of the error influence at longer distances e. g. 30 m it is not possible to use only the TMS due to the decrease of the accuracy and the spatial limitations in the laboratory. In this case, the object point P_i is determined with the TMS from a base b (TS1 - TS2) which is located at a short distance to the planar object (approx. 1.6 m) (Figure 1 b). The base points and the reference point of the scanner are determined in a geodetic high-precision network (TS1, TS2, TLS + TS, reflectors R_1 - R_8).
5) The variant for determining the reference distance is selected according to the a priori accuracy analysis. The reference should be at least one order of magnitude more accurate than the investigated distance.
6) Steps 2 and 3 are repeated for distances under different IA.
7) The character of the influence of IA will be investigated on the basis of the differences between the reference D_{ref} and TLS-distances D_{TLS}.

3. Measurements

The study was carried out with a Leica MultiStation MS50. It is characterised by the accuracy of the RL-distance measurement of 2 mm + 2 ppm, a distance measurement noise of 0.4 mm up to 10 m, 0.5 mm up to 25 m at measurement frequency of 62 Hz and the angular accuracy of 0.3 mgon. The spot size is 7 × 10 mm at 30 m.

The MS50 was used at close range (3.5 to 5.2 m) as well as at a distance of ca. 30 m under laboratory conditions. The near field was chosen because instruments have special behaviour in this range. The distance of 30 m belongs to usually measured distances at scanning of structures. Scanning was performed with the measuring rate of 62 Hz. The scanning parameters were set in a way that avoids correlations between adjacent distances.

The measurement process is automated predominantly via GeoCOM control. In the following sub-sections the measurement setup and the measurement procedure of the two cases of investigations are described.

3.1 Experiment at close range

A wooden class-board was used as a test object (Figure 1 a). It has dark green color, dimensions of 5 m × 1.5 m × 0.025 m (width × height × depth) and is almost vertically fixed to the wall. The two station-points of the TMS were placed at 3.5 m from the object. In this measurement setup the MS50 was simultaneously used as a theodolite within the TMS configuration. The base b between the theodolites (TLS + TS, TS) was 3.5 m long. For the basis determination a reference scale of 0.8 m was positioned horizontally.

Different IAs of the laser beam are obtained by the rotation of instrument's collimation axis in horizontal and vertical direction. In this measurement setup the TLS-distances vary from 3.5 m at IA of 0 gon to 5.2 m at IA of 55 gon.

In the measurement procedure first preparation steps were performed for TMS - mutual orientation of the horizontal circle of the theodolite and base determination. The mutual orientation was determined by collimation in two faces. Both instruments are specified with the same angular accuracy of σ_{Hz} = 0.3 mgon. The base was indirectly determined by solving the Hansen problem [11]. The length of the reference scale was measured with the laser interferometer Agilent 5530 with $\sigma_{ref.\ scale}$ 0.4 ppm. The pointing precision to targets of the reference scale with MS50 is 0.3 mgon and with TS 0.3 mgon at the first and 0.7 mgon at the second end point (from 10 repetitions).

Subsequently, the board was scanned in one face with a resolution of 0.3700 gon. The atmospheric corrections were applied to the distance measurement.

The obtained point cloud of the object was approximated by a plane. Hence, for each point the IA was calculated as the angle between the normal vector of the plane and the sighting line under Hz_{TLS} and V_{TLS}. The IA calculated in this way varies from 0 to 55 gon. The point cloud was divided in 5-gon zones of IA and 7 points per zone were selected for further study of the distance.

Each selected point was staked out, the RL distance in the single mode D_{RL} was measured and the point was signalised with a needle. Its position was determined from Hz, V measurements performed in two faces from the two TMS-stations. The points located in two zones were determined twice, in order to empirically determine the precision of the staking out and of the reference measurement. A maximum deviation of two determinations of the reference distance of 0.4 mm was obtained by this procedure.

The stability of the stations was monitored during the measurement process; first by collimation, secondly by repeated measurements to surrounding prisms, and third by repeated base determination. Within a time interval of 2 months the measurements were performed with two different TLS+TS instruments using the same measuring setup and another measuring arrangement with a longer base of about 7 m as well.

3.2 Experiment at 30 m-long distance

The test object used in this case was a granite board with dimensions 0.40 × 0.40 × 0.03 m (width x height x depth), that has a smooth and a rough side (Figure 2). It was placed nearly vertically on a Thorlabs board and fixed laterally. The Thorlabs board with weight of 30 kg and dimensions of 0.60 × 0.60 × 0.06 m is sufficiently stable for the granite board.

The different IAs were obtained by rotating the object around its vertical axis. For this purpose, an angular scale was used. The TLS+TS was installed on a pillar about 30 m away from the test object. The distance between the two theodolites (TS1 and TS2) forming the TMS was 2.4 m. The base was placed at a distance of ca. 1.6 m from the object. The three instrument stations and the surrounding 8 prisms (R_i) mounted on consoles and pillars form the geodetic high-precision network.

The measurement campaign started with the determination of the precise network. During the entire campaign, the three instruments remained mounted in tribrachs to avoid centering errors. Therefore, with each instrument (TLS+TS, TS1, TS2) the elements Hz, V, D were measured to the prisms while only Hz, V were measured to the other instruments by the collimation in 3 sets. TS1 and TS2 have a specified angular accuracy of 0.3 mgon, TS1 the distance accuracy of 2 mm + 2 ppm and TS2 1 mm + 1.5 ppm.

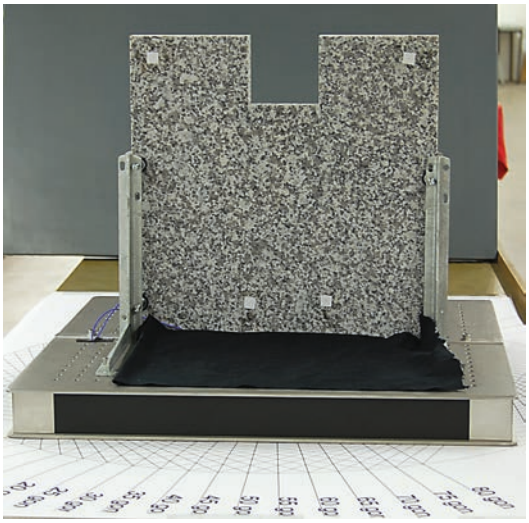

Fig. 2: Test object – granite board with four points for control measurement

For each IA the granite board was scanned with a resolution of 0.0212 gon in one face. Just as in close range it was then approximated by a plane. At each IA among all scanned points 5 per position were selected on the basis of their distance to the adjusted plane. Each selected point was staked out and signalised in the Hz_{TLS}, V_{TLS} direction. The 3D-position of the signalised point was determined in two faces with TMS. The granite board was aligned in steps of 10 (5) gon in order to get IA between 0 and 60 gon. The influence of the IA was studied on both sides of the granite board. At IAs of 0, 45, 55 gon staking out and TMS-measurements were realised twice, in order to quantify the precision.

By means of measuring 4 points on the board before and after staking out it was verified if the position of the board remained unchanged during the staking out and the reference measurement process (Figure 2). The stability of three stations was controlled by polar measurements to prisms and the Hz, V directions measurements between stations.

4. Post processing and results

The reference distances were determined from the highly accurate measurements. They meet the high accuracy requirement that is necessary in order to quantify the influence of the IA. Any systematic deviation affecting these measurements was first analysed. Based on this assessment the accuracy achieved for the reference range could be expressed. Furthermore, reference and TLS-distances were compared, the resulting distance differences were analysed and conclusions were drawn.

4.1 Investigation at close range

The reference distances are determined from the coordinates of the TLS + TS-zero point and of the selected object points. Errors that could possibly affect the obtained reference distance are listed in Table 1. They were methodically eliminated or quantified and their impact was evaluated. Based on this research we conclude that the reference distance could be systematically distorted up to ca. 0.2 mm.

The a priori standard deviation of the reference distance of 0.2 mm was obtained by simulation studies. This value conforms exactly to the empirical standard deviation of the reference distance, obtained from two independent repeated determinations of the reference distance in two zones.

The differences between the reference distances D_{ref} and the corresponding distances in the scanning mode D_{TLS} are shown in Figure 3a. The illustrated differences vary systematically with the IA. The scanned distances are up to 3.0 mm longer than D_{ref} in two intervals: 0–35 and 50–55 gon. In contrast, the distances are up to 4.4 mm shorter within the interval 35–50 gon. The shown systematic effect is physically or geometrically not-explainable. It was therefore assumed, that the obtained effect results from a superposition of the influence of IA with other effects in close range.

The systematic difference between the reference and the scanned distances was repro-

Influence	Impact/Elimination
Stability of the theodolite	1. Repeated measurement of 5 prisms max. coordinate difference of 0.5 mm – within the accuracy of the measurement method 2. Repeated collimation – emp. σ of 0.5 mgon 3. Repeated base determination σ of 0.1 mm, max. deviation of 0.3 mm Stable stations
Axes errors, eccentricity errors	Eliminated by measurements in two faces
Skewness of the trunnion axis	Min. impact at V directions from 95 to 105 gon
Collimation	Emp. σ of 0.5 mgon, max. deviation 1.2 mgon Max. impact on the reference distance 0.2 mm
Base determination	σ of 0.1 mm, max. deviation 0.3 mm
Hz, V – Scanning/Staking out	Max. deviation in Hz und V of 0.8 mgon Max. impact on the reference distance 0.02 mm No influence
Divergence of the line of sight and distance axis	Quantified in Tab. 2 at 30 m, at 5 m ~1/6 from max. deviation of 0.5 mm ~0.08 mm
Intersection angle	45–58 gon Measurement with another configuration with doubled base length No influence
Staking out/TMS	Repeatability of reference distance σ of 0.2 mm

Tab. 1: Error influences on the reference distance determination in close range

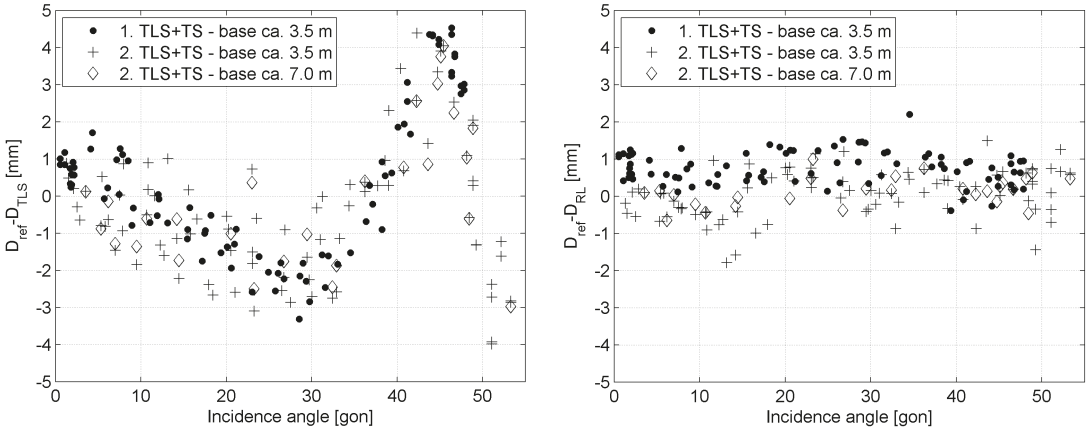

Fig. 3: Distance differences as function of the incidence angle; a) differences between D_{ref} and D_{TLS} (TLS-scanning mode), b) differences between D_{ref} and D_{RL} (RL-single mode)

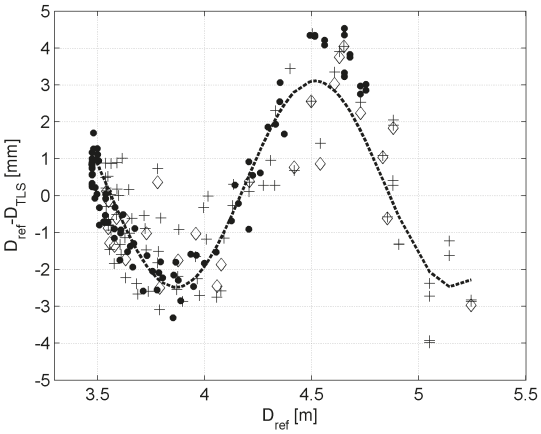

Fig. 4: Differences between D_{ref} and D_{TLS} as function of the distance

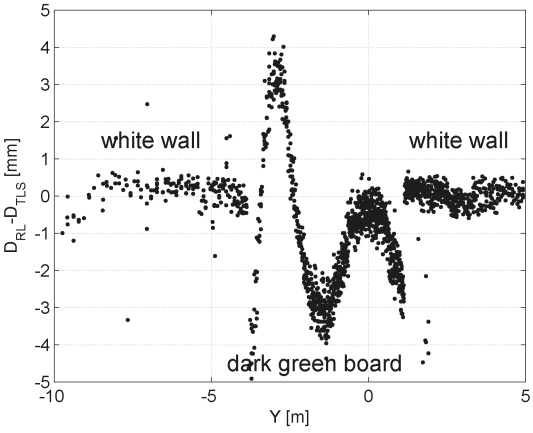

Fig. 5: Differences D_{RL}-D_{TLS} as function of the material (abscissa Y-coordinate, almost parallel to the board)

duced 1.5 months later with another instrument of the same type using the same configuration as well as a slightly modified configuration with a longer base (Figure 3a).

If the systematic part of the distance deviation is split up using an appropriate approximating polynomial function, the stochastic properties in each zone of IA can be quantified. In this case, it is not relevant to express the precision as a function of the IA.

The differences between the reference distance and the reflectorless distance measurement in single mode $D_{ref} - D_{RL}$ show no systematic effects. The distance deviations are mainly in the interval of −1.0 mm to 1.5 mm, which corresponds to the manufacturer specification (2 mm + 2 ppm) (Figure 3b).

4.1.1 Systematic course in close range

To explain the occurred systematic effect in TLS-distance (Figure 3a) further analysis and experiments were performed. The conceptual connection of the investigations is:

a) Determination of the distance dependence.

b) Indication of the surface dependency.

c) Determination of the colour dependence.

A) Distance dependence

In the experimental setup not only the IA varies, but also the distances. Therefore, the differences

$D_{ref} - D_{TLS}$ were plotted as a function of distance in Figure 4. Obvious distance dependence in the form of a cyclic oscillation can be noticed. However, this could not be a cyclic phase error because the instrument uses the time of flight method for distance measurements. To split up the influence of the distance a measuring arrangement with a fixed distance (minimal distance variation) and variable IA needs to be realised in the future.

B) Material dependence

The RL-distances measured in the single mode showed a good agreement with the TMS-distances (Figure 3 b). For this reason in the following, the former are used as a reference basis for comparison. The board and parts of the adjacent white concrete wall have been scanned. The distances to some points were measured reflectorless in single mode (RL). The differences between RL- and scanned distances are shown in Figure 5 and indicate that the systematic effect is occurring only for the dark green board. Thus, the material dependence is evident. It should be noticed that the board has much lower reflectivity (8 %) than the wall (90 %) (empirically determined using Kodak gray card).

C) Dependency on the colour

Another board of the same colour and of another material consisting of a layer of glass and chipboard was examined as in the previous experiment B. In addition, different light colours were applied with chalk. The systematic differences

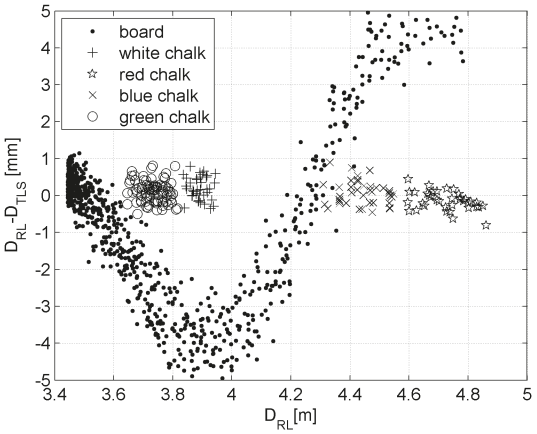

Fig. 6: Differences $D_{RL} - D_{TLS}$ as function of the distance;, distances were measured to a surface of different colours

with the magnitude of ca. 4 mm occur only in case of dark green surfaces (Figure 6).

At the close range the systematic cyclic error effect influences TLS-distances. It occurs by scanning of dark green material.

A systematic material dependent effect at close range was also found in an earlier study [12] when measuring distances in single mode.

4.2 Investigation at a distance of 30 m

The reference distances D_{ref} were determined in two steps. First the coordinates of the intersection point of instrumental axes (zero point) were determined by a free adjustment of the high-precision network. Actual instrumental parameters were considered, which were determined by the method of ISO17123-4 [13]. The precision obtained for the position of zero points is (maximum values) σ_Y = 0.03 mm, σ_X = 0.14 mm, σ_Z = 0.02 mm. These standard deviations seem to be optimistic due to the determination under repeatability conditions. However, they are representative for our case because the instruments remain fixe in the tribraches during the entire measurement campaign. Secondly the coordinates of object points P_i were calculated using spatial forward intersection with the base formed by TS1 and TS2.

The reference distances were obtained from the coordinates of the zero point of TLS + TS and of the determined object points.

Errors of the network measurement, the staking out and the TMS measurement affect the determined reference distance. Their contribution to the uncertainty of the reference distance is analysed and summarised in Table 2. The highest error influence is due to the staking out. In our case, if the granite board rotates around the vertical axis, stakeout precision in the horizontal direction directly affects the TLS-distance (e. g. a lateral deviation of 1.0 mm causes at an IA of 60 gon a distance error dD of 1.4 mm). This uncertainty is mainly caused by the thickness of the cross-hair and the magnification of the telescope. In future, the scale of the precise network e. g. the base should be controlled with high-accurate measurement.

The precision of the reference distance is calculated in the following way:

$$\sigma_{ref} = \sqrt{\sigma_{NET\_TMS}^2 + \sigma_{Stak}^2}, \text{ where} \quad (1)$$

$$\sigma_{Stak} = \sqrt{\sigma_{Stak\_TMS}^2 - \sigma_{TMS}^2}.$$

	Influence		Impact/Elimination
Precision network	Points definition	Stability of stations	1. Repeated measurement of 8 prisms - max. deviation in a coordinate of 0.7 mm 2. Hz, V - measurement between instrument stations – max. V - deviation of 1.3 mgon – max. Hz - deviation from the sum of the interior angles of the triangle (TLS + TS, TS1, TS2) 1.1 mgon – The individual Hz - directions vary within an interval of 2.5 mgon for TS1 and TS2, and of 0.9 mgon for TLS + TS; this results in a probable twisting of the Hz - circle (TS1 - 1.9 mgon, TS2 - 1.6 mgon) The internal geometry is preserved.
		Centering error - instruments	Instruments remain in tribraches, Hz - and V - measurement through the collimation
		Centering error - prisms	Without removing
	Angle	Axes errors, eccentricity errors	Eliminated in two faces
		Skewness of the trunnion axis	Object points are measured under vertical angles of 111 – 116 gon Network points are measured under vertical angles of 83 – 102 gon Close to the horizon, lower impact
	Distance	Zero points errors	Considered
		Scale error	Potential for improvement
		Atmospheric corrections	Considered
	Precision of station coordinates		max. σ_Y = 0.03 mm, σ_X = 0.14 mm, σ_Z = 0.02 mm
Staking out	Hz, V – Scanning/Staking out		max. dev. 0.6 mgon, lateral deviation of 0.3 mm, distance deviation of 0.4 mm under IA of 60 gon
	Repeatability of staked out and with TMS determined distance		One point was staked-out 12 times under an IA of 55 gon, and determined with TMS σ = 0.29 mm
	Repeatability of staked out and with TMS determined distance		Twofold determination of the reference distances of 5 points under IA of 0, 40, 45, 55, 60 gon σ = 0.05 – 0.51 mm
	Divergence of the line of sight and distance axis		Distance measurement in single mode in two faces at IA = 60 gon, D = 30 m – rotation of the board clockwise and counterclockwise Max. distance deviation of 0.5 mm (incl. pointing uncertainty)
TMS	Precision of azimuth R_{TS1_TS2}		σ = 0.1 mgon
	Precision of base		σ = 0.07 mm
	Angle errors		As in the network
	Twisting of the Hz-circle at TS1 and TS2		Max. difference of the reference distance of 0.02 mm
	Board stability – before/after staking out		4 points were measured with TMS before and after staking out Max. coordinate deviation of 0.05 mm
	Repeatability of the distance determination by TMS		1 point signalised with the needle once and measured 12 times by TMS σ = 0.01 mm

Tab. 2: Error influences on the reference distance determination at 30 m

σ_{Net_TMS} – standard deviation of the reference distance (TLS + TS, P_i) derived with variance propagation law by taking into account full covariance matrix of the network adjustment (0.17 mm),

σ_{Stak} – empirical standard deviation of the staked out reference distance,

σ_{Stak_TMS} – empirical standard deviation of the repeatedly staked out and with TMS determined reference distance (0.05 – 0.51 mm),

σ_{TMS} – empirical standard deviation of the once signalised and repeatedly with TMS determined reference distance (0.01 mm);

IA [gon]	0	40	45	55	60
Rough surface	0.18	0.45	—	0.27	—
Smooth surface	0.18	0.24	0.52	0.22	0.54

Tab.3: Standard deviation of the reference distance [mm]

The precision of the reference distance varies between 0.18 and 0.54 mm (Table 3).

The individual distance differences for both sides of the granite board are shown in Figure 7. In order to suppress the measurement noise, the distance differences per IA were averaged. The empirical standard deviations of a distance difference per IA reach values between 0.3 and 1.0 mm. The standard deviations of the mean values are between 0.1 to 0.4 mm. The averaged differences between the reference and TLS-distances at each IA are illustrated in Figure 8. Comparing the mean values with their standard deviations we conclude according to the 3Sigma-rule (P = 99.7 %) that the deviations are significant (Figure 8).

The differences (Figure 8) have a distance offset at IA 0 gon and vary systematically with the IA. At the rough surface of the granite board the TLS distance is 0.8 mm longer at AW 0 gon. This difference increases at larger IA up to 2.5 mm. The total variation of the distance difference with IA is of 1.7 mm. The smooth surface shows a similar behavior. At an IA of 0 gon the TLS distances are longer by 1.1 mm. At 60 gon the difference achieves 3.1 mm. Its total variation is of 2.0 mm.

The significant offset (at the rough surface - not significant at P = 99.7 %) in the case of IA = 0 gon is surprising and needs further investigation. This IA is ideal for the RL measurement. The offset can be caused by other error influences on the RL distance measurement such as the reflectivity of the surface or the penetration of the laser [14].

The obtained systematic variation of the distance differences is caused most probably by the influence of the IA on the TLS distance measurement. Higher IA lead to worse geometrical and physical conditions, resulting in greater distance distortion. As in the case of the close range investigation the variation of the differences is strongly correlated with the received signal strength (Figure 9). Both, the distance differences and the received signal strengths are shifted (Figure 8 and 9). They also point to the influence of the surface roughness. The TLS-distances differences to the smooth surface are in average 0.7 mm longer than the ones for the rough surface.

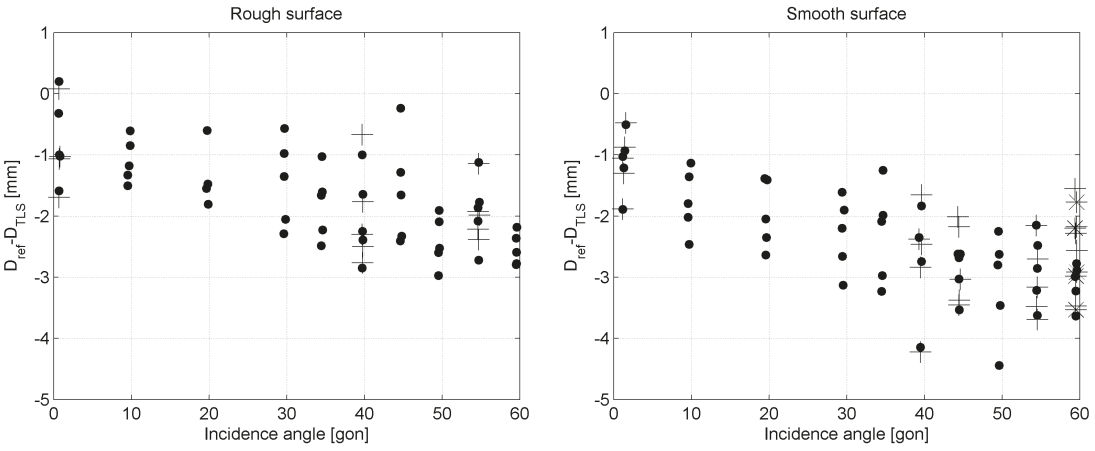

Fig. 7: Differences D_{ref} and D_{TLS} as function of the incidence angle (repeated determination – cross, star)

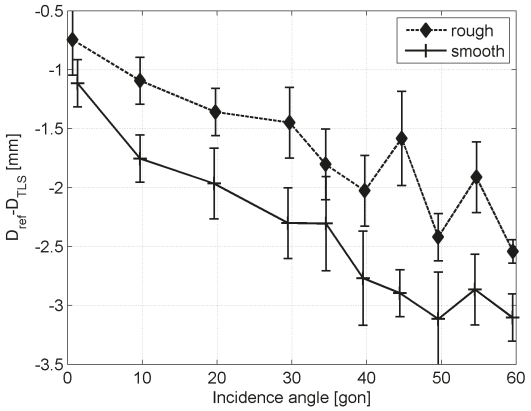

Fig. 8: Mean value of differences D_{ref} and D_{TLS} per one incidence angle and their standard deviations

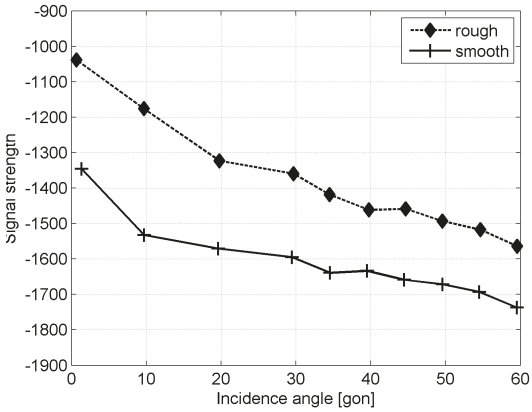

Fig. 9: Mean value of received signal strength by scanning to the rough and smooth surface of the granite board

In order to quantify the stochastic properties of the distances measured under various IA, we have assumed that the reference distances are more precise than D_{TLS}. Under this condition, the systematic component should be separated and the standard deviations calculated with respect to the IA. However, in our experiment this basic assumption was not met. Thus, the stochastics of the distances among IA is not quantified. This lack of the presented methodology needs to be eliminated in future works.

5. Conclusion and outlook

In this paper, a new method for investigating the influence of IA on the reflectorless distance measurement of scanning total stations was presented. It is new and unique by comparing the directly measured scanned distances to the reference in the areal acquisition. It is variable for distances of different lengths and was applied here for two ranges.

At close range of 3.5 to 5.2 m it was found out that other errors are more pronounced than the IA. A systematic cyclic distance-dependent effect up to 4.4 mm was detected at a material of dark green color with low reflectivity. Its physical cause needs to be clarified in the future. It has been shown that in the realised measurement configuration with a fixed object, the variation of the investigated TLS-distances should be minimised or even eliminated. As a result, the object should not be fixed but rotatable.

At the distance of 30 m a systematic effect of IA was detected. In the range of IAs between 0 and 60 gon the distances differences between reference and TLS vary up to 1.7 mm on the rough side and up to 2.0 mm on the smooth side of the granite board. The variation of the distance differences is closely related to the received signal strength. In addition, at IA of 0 gon a distance offset of −0.8 mm for the rough surface and −1.1 mm for the smooth surface could be detected. The stochastic properties of the error influence could not be quantified because the reference distances are too noisy. From the realised investigation it can be concluded that the uncertainty of the reference distance should be increased, especially the precision of the staking-out should be minimised. For the determination of the stochastics the methodology could be added to repeat scanning of the object in the identical Hz and V grid. From the repeated distance measurements stochastic properties of the error influence can be obtained.

The first experiences show that the developed methodology for investigating the influence of the IA has great potential. In future work the methodology will be improved with respect to the above mentioned shortcomings.

References

[1] *Lindstaedt, M., Kersten, T., Mechelke, K., Graeger, T., Sternberg, H. (2009)*: Phasen im Vergleich - Erste Untersuchungsergebnisse der Phasenvergleichsscanner FARO Photon und Trimble GX. In: Photogrammetrie, Laserscanning, Optische 3D-Messtechnik - Beiträge der Oldenburger 3D-Tage 2009, Wichmann Verlag, Heidelberg, pp. 53–64.

[2] *Schulz, T. (2007)*: Calibration of a Terrestrial Laser Scanner for Engineering Geodesy. Dissertation ETH, Zürich. In: http://www.geometh.ethz.ch/people/former_staff/schulzt/TS_PhD_Final.pdf

[3] *Gordon, B. (2008a)*: Zur Bestimmung von Messunsicherheiten terrestrischer Laserscanner. Dissertation, Technische Universität Darmstadt. In: http://tuprints.ulb.tu-darmstadt.de/1206/1/Dissertation_BGordon.pdf

[4] *Joeckel, R., Stober, M., Huep, W. (2008)*: Elektronische Entfernungs- und Richtungsmessung und ihre Integration in aktuelle Positionierungsverfahren. 5. Auflage, Wichmann Verlag, Heidelberg.

[5] *Kern, F. (2003)*: Automatisierte Modellierung von Bauwerksgeometrien aus 3D-Laserscanner-Daten. Dissertation, Geodätische Schriftenreihe der Technischen Universität Braunschweig (19).

[6] *Kersten, T., Mechelke, K., Lindstaedt, M., Sternberg, H. (2008)*: Geometric Accuracy Investigations of the Latest Terrestrial Laser Scanning Systems. In: CD-Proceedings, FIG Working Week, Stockholm, Sweden, June 14-19, 2008.

[7] *Schäfer, T., Schulz, T. (2005)*: Kalibrierung, Einflussgrößen und Genauigkeiten von Terrestrischen Laserscannern. In: Terrestrisches Laserscanning (TLS), Schriftenreihe des DVW (48), Wißner Verlag, Augsburg, pp. 29-48.

[8] *Soudarissanane, S., Lindenbergh, R., Menenti, M., Teunissen, P. (2011)*: Scanning geometry: Influencing factor on the quality of terrestrial laser scanning. ISPRS Journal of Photogrammetry and Remote Sensing 66 (2011), pp. 389-399.

[9] *Mechelke, K., Kersten, T., Lindstaedt, M. (2007)*: Comparative Investigation into the Accuracy Behaviour of the New Generation of Terrestrial Laser Scanning Systems. In: Optical 3-D Measurement Techniques VIII., Zürich, pp. 319-327.

[10] *Gordon, B. (2008b)*: Diskussion von Feldprüfverfahren zur Messunsicherheitsbestimmung für terrestrische Laserscanner. In: Terrestrisches Laserscanning (TLS 2008), Schriftenreihe des DVW (54), Wißner Verlag, Augsburg, pp. 125-142.

[11] *Witte, B., Sparla, P. (2011)*: Vermessungskunde und Grundlagen der Statistik für das Bauwesen. Wichmann Verlag, Berlin, pp. 662-665.

[12] *Juretzko, M. (2006)*: Leistungsfähigkeit des reflektorlosen Distanzmessmoduls R300 der Tachymeterserie TPS1200 von Leica. Flächenmanagement und Bodenordnung (FuB), 2/2006, pp. 90-95.

[13] *ISO17123-4 Optics and optical instruments - Field procedures for testing geodetic and surveying instruments - Part 4*: Electro-optical distance meters (EDM measurements to reflectors).

[14] *Zámečníková, M., Wieser, A., Woschitz, H., Ressl, C. (2014)*: Influence of surface reflectivity on reflectorless electronic distance measurement and terrestrial laser scanning. Journal of Applied Geodesy, 8 (2014), 4, pp. 311-325.

Contacts

Univ.Ass Dipl.-Ing. Miriam Zámečníková, PhD., Vienna University of Technology, Department of Geodesy and Geoinformation, Engineering Geodesy Group, Gußhausstraße 27-29, 1040 Wien, Austria.
E-Mail: Miriam.Zamečnikova@geo.tuwien.ac.at

Univ.-Prof. Dr.-Ing. Hans Neuner, Vienna University of Technology, Department of Geodesy and Geoinformation, Engineering Geodesy Group, Gußhausstraße 27-29, 1040 Wien, Austria.
E-Mail: hans.neuner@geo.tuwien.ac.at

Bakk. techn. Stefan Pegritz, Vienna University of Technology, Department of Geodesy and Geoinformation, Engineering Geodesy Group, Gußhausstraße 27-29, 1040 Wien, Austria.
E-Mail: stefan.pegritz@tuwien.ac.at

Bakk. techn. Robert Sonnleitner, Vienna University of Technology, Department of Geodesy and Geoinformation, Engineering Geodesy Group, Gußhausstraße 27-29, 1040 Wien, Austria.
E-Mail: e0726536@student.tuwien.ac.at

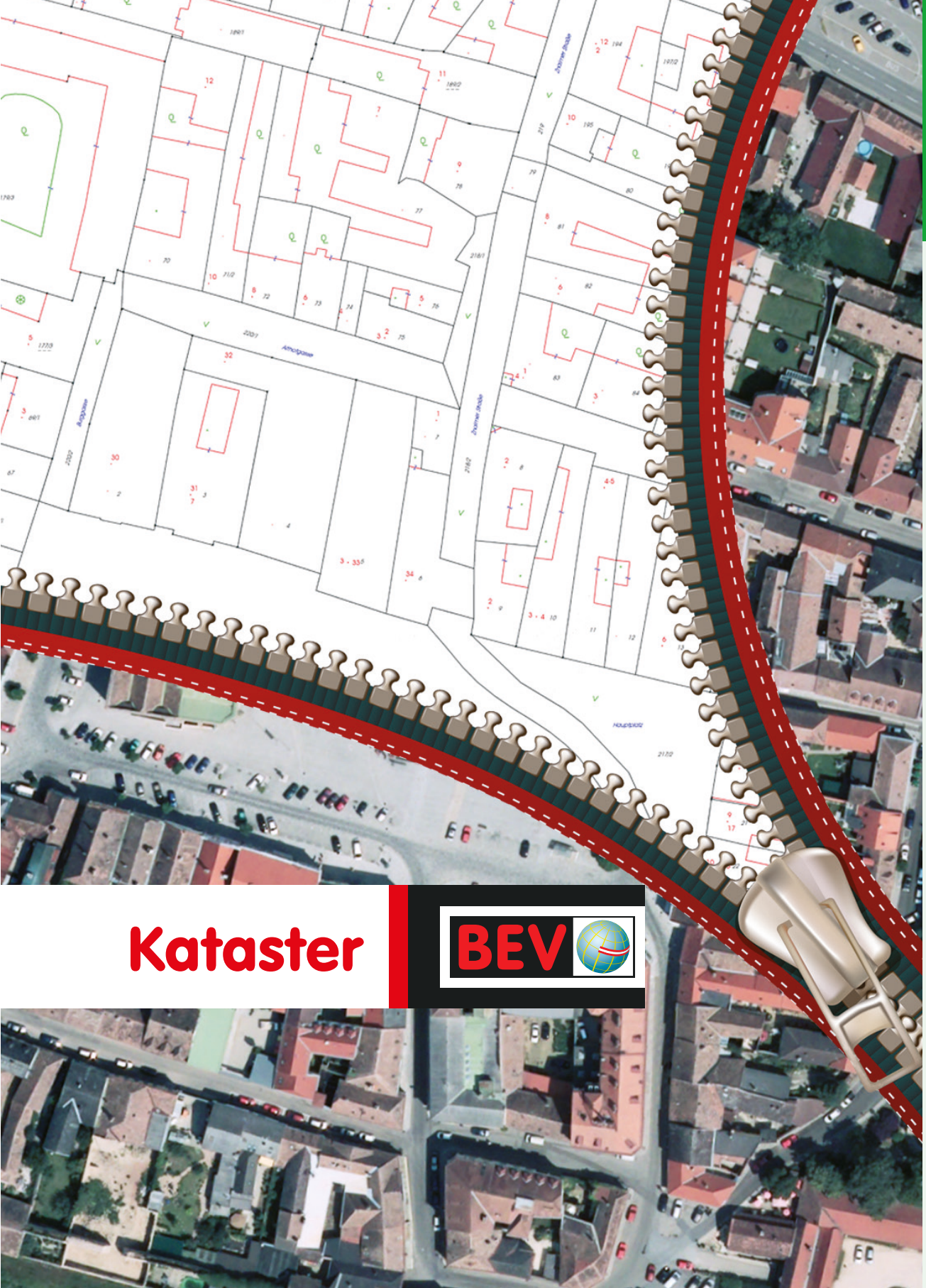

Kataster

BEV